Chem Soc Rev

REVIEW ARTICLE

View Article Online
View Journal | View Issue

Cite this: *Chem. Soc. Rev.*, 2018, **47**, 1822

Raman spectroscopy of graphene-based materials and its applications in related devices

Jiang-Bin Wu,[ab] Miao-Ling Lin,[ab] Xin Cong,[ab] He-Nan Liu[a] and Ping-Heng Tan *[ab]

Graphene-based materials exhibit remarkable electronic, optical, and mechanical properties, which has resulted in both high scientific interest and huge potential for a variety of applications. Furthermore, the family of graphene-based materials is growing because of developments in preparation methods. Raman spectroscopy is a versatile tool to identify and characterize the chemical and physical properties of these materials, both at the laboratory and mass-production scale. This technique is so important that most of the papers published concerning these materials contain at least one Raman spectrum. Thus, here, we systematically review the developments in Raman spectroscopy of graphene-based materials from both fundamental research and practical (*i.e.*, device applications) perspectives. We describe the essential Raman scattering processes of the entire first- and second-order modes in intrinsic graphene. Furthermore, the shear, layer-breathing, G and 2D modes of multilayer graphene with different stacking orders are discussed. Techniques to determine the number of graphene layers, to probe resonance Raman spectra of monolayer and multilayer graphenes and to obtain Raman images of graphene-based materials are also presented. The extensive capabilities of Raman spectroscopy for the investigation of the fundamental properties of graphene under external perturbations are described, which have also been extended to other graphene-based materials, such as graphene quantum dots, carbon dots, graphene oxide, nanoribbons, chemical vapor deposition-grown and SiC epitaxially grown graphene flakes, composites, and graphene-based van der Waals heterostructures. These fundamental properties have been used to probe the states, effects, and mechanisms of graphene materials present in the related heterostructures and devices. We hope that this review will be beneficial in all the aspects of graphene investigations, from basic research to material synthesis and device applications.

Received 31st July 2017

DOI: 10.1039/c6cs00915h

rsc.li/chem-soc-rev

[a] *State Key Laboratory of Superlattices and Microstructures, Institute of Semiconductors, Chinese Academy of Sciences, Beijing 100083, China*
[b] *CAS Center of Excellence in Topological Quantum Computation, and College of Materials Science and Opto-Electronic Technology, University of Chinese Academy of Science, Beijing 100049, China. E-mail: phtan@semi.ac.cn*

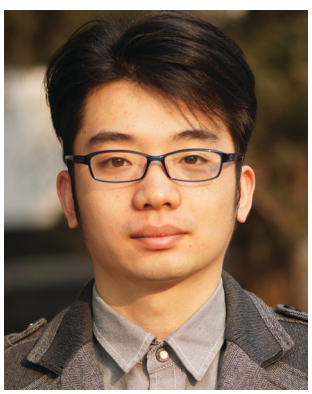

Jiang-Bin Wu

Jiang-Bin Wu is now a postdoc at Ming Hsieh Department of Electrical Engineering, University of Southern California. He obtained his PhD degree from the Institute of Semiconductors at the Chinese Academy of Sciences supervised by Prof. Ping-Heng Tan in 2017. He received his BS degree from Huazhong University of Science and Technology in 2012. His current research focuses on the optical properties of two-dimensional materials and heterostructures.

Miao-Ling Lin

Miao-Ling Lin received her BS (2014) in physics from Nankai University, Tianjin, China. She is now a PhD student supervised by Prof. Ping-Heng Tan in the State Key Laboratory of Superlattices and Microstructures, Institute of Semiconductors, Chinese Academy of Sciences. Her current research interest focuses on optical properties of low-dimensional nanomaterials.

1 Introduction

Graphene is a truly two-dimensional (2d) system, consisting of sp^2 carbon hexagonal networks with strong covalent bonds.[1] Multilayer graphene (MLG) can be stacked layer by layer in a Bernal (AB) or rhombohedral (ABC) way through van der Waals (vdW) coupling.[2–6] High-quality monolayer graphene (1LG) and MLG can be produced by several methods, such as micromechanical exfoliation (ME), chemical vapor deposition (CVD), and epitaxial growth from the SiC surface.[1,7–10] Other artificial fabrication routes for production, such as the reduction of a graphene oxide (GO) solution and organic synthesis, tend to introduce defects into the graphene,[11–13] such as vacancies and dislocations, as well as exposing the graphene to oxidation, hydrogenation, fluorination, and other chemical functionalizations.[14–16] Graphene can also be decomposed into one-dimensional (1d) and zero-dimensional (0d) forms, such as graphene nanoribbons (GNR) and nanographene.[17–21] All these materials with various dimensions are derived from 1LG and can be termed graphene-based materials. The remarkable properties of graphene-based materials, including their high carrier mobility (near-ballistic transport), high thermal conductivity, unique optical and mechanical properties, and high specific surface area, make them promising materials for high-frequency nanoelectronics, micro- and nanomechanical systems, thin-film transistors, transparent and conductive composites and electrodes, batteries and supercapacitors with high charging speeds, highly sensitive chemical sensors, flexible and printable optoelectronics, and photonics.[1,22–27] On the other hand, recent research studies have advanced to investigate vertical van der Waals heterostructures (vdWHs) because they can be formed by vertically stacking various 2d materials (2DMs) by van der Waals forces but without any constraints of lattice matching and fabrication compatibility, offering huge opportunities for the design of new functionalities.[28–30] In particular, hybrid systems consisting of transition metal dichalcogenides (TMD) and graphene (TMD/graphene vdWHs) have been used for various high-performance devices by taking advantage of the high mobility of graphene and the natural band gap of TMDs.[31–35] 1LG and MLG are the essential building blocks for vdWHs[36] as electrodes in various high-performance devices, such as field-effect tunneling transistors, logic transistors, photovoltaics, and memory devices.[37–42] Therefore, a versatile technique to identify and characterize graphene-based materials both at the laboratory and the mass-production scale and to probe the state, effects, and functionalization mechanism of these materials in the heterostructures and devices is essential for material synthesis, basic research, and device applications.

Raman spectroscopy is a fast, nondestructive, and high-resolution tool for the characterization of the lattice structure and the electronic, optical, and phonon properties of carbon materials, including three-dimensional (3d) diamond and graphite, 2d graphene, 1d carbon nanotubes, and 0d fullerenes, as shown in Fig. 1(a).[43–54] Raman spectra of all graphene-based

Xin Cong

Xin Cong is a PhD student in the Institute of Semiconductors at the Chinese Academy of Sciences supervised by Prof. Ping-Heng Tan. He received his BS degree from Huazhong University of Science and Technology in 2016. His current research focuses on the optical properties of two-dimensional semiconductors.

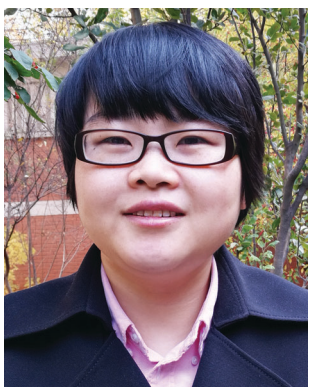

He-Nan Liu

He-Nan Liu is currently an assistant professor at the School of Precision Instrument and Opto-Electronics Engineering, Tianjin University. She received her PhD degree from the University of North Carolina at Charlotte in 2015 and worked as a postdoctoral fellow from 2016 to 2017 in the State Key Laboratory of Superlattices and Microstructures, Institute of Semiconductors, Chinese Academy of Sciences. Her major research interest includes Raman spectroscopy of two-dimensional materials.

Ping-Heng Tan

Ping-Heng Tan is a Professor in the State Key Laboratory of Superlattices and Microstructures at the Institute of Semiconductors, Chinese Academy of Sciences. He obtained BS (1996) in Physics from Peking University and PhD (2001) from the Institute of Semiconductors, Chinese Academy of Sciences. He worked at Walter Schottky Institut, Technische Universitaet Muenchen as a Postdoc Research Associate from 2001–2003. He was a KC-Wong Royal Society Fellow at Cambridge University from 2006–2007. His current research is on two-dimensional layered materials, nanocarbon materials, topological insulators and novel low-dimensional semiconductor optoelectronic materials. He was supported by the National Science Fund for Distinguished Young Scholars in 2012.

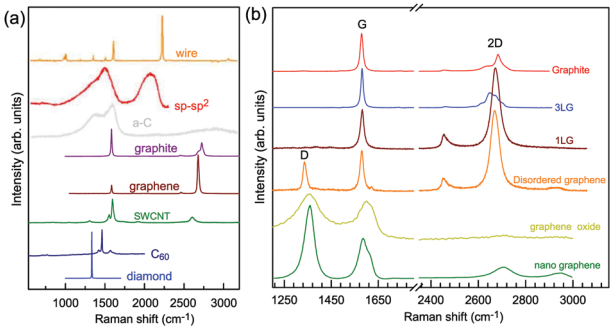

Fig. 1 (a) Raman spectra of carbon solids and nanostructures, including 1d carbon wires, sp–sp^2 carbon, amorphous carbon (a-C), graphite, graphene, single-walled carbon nanotubes (SWNT), C_{60}, and diamond. Raman spectra of carbon wire, sp–sp^2 carbon, a-C are reproduced with permission from ref. 43. Copyright 2015, Beilstein-Institut. (b) Raman spectra of graphene-based materials, including graphite, 1LG, 3LG, disordered graphene, graphene oxide and nanographene.

materials show few prominent features regardless of the final structure.[55] However, the positions, line shapes, and intensities of these peaks give abundant useful information for the investigation of the structures and electronic properties of graphene-based materials.[55–57] For example, for the G mode of graphene excited by an excitation energy (ε_L, E_L or E_{ex}), the peak position (Pos(G)) or frequency (ω(G), or ω_G), line shapes (Lorentzian or Fano), full width at half maximum (FWHM(G) or Γ_G), peak intensities (I(G) or I_G), and peak area (A(G) or A_G), *i.e.*, integrated intensity, are closely related to its doping level.[58–65] In Fig. 1(b), the Raman spectra of various graphene-based materials showing the D, G and 2D spectral regions are shown, demonstrating their similarity. The intrinsic properties of samples from monolayer to few-layer graphene, as well as bulk graphite, can be distinguished from the spectral profile of the 2D modes. In addition, the D peak can be used to characterize graphene-based materials with defects, such as disordered graphene, graphene oxide, and nanographene.[66–68] On the other hand, the Raman features of graphene-based materials depend not only on the phonon properties but also on the corresponding electronic properties, *e.g.*, the unique linear band structure in 1LG and distinct band structures in MLG.[44] In 1LG, the origin of the overtone and combination modes, such as the 2D and D + D″ modes, is the triple resonance (TR) or double resonance (DR) process, which is related to the linear dispersion of its electronic bands.[66,69] For *N*-layer graphenes (*N*LGs), the stacking order has an important influence on the band and interlayer phonon properties, leading to *N*- and stacking-orientation-dependent Raman spectra.[5,6,53,55,57,70,71] In addition, quantum interference effects play a key role in determining the Raman intensity of graphene.[58,72,73] Moreover, in the presence of external perturbations, such as defects,[15,16,74–80] doping,[58–65] strain, stress,[81–87] magnetic fields,[88–98] and temperature,[99–103] the electronic and lattice vibration properties change significantly, which can be determined using Raman spectroscopy. Based on the Raman spectra of intrinsic 1LG and MLG and their responses to external perturbations, Raman spectroscopy has been widely utilized to investigate the properties of graphene materials and their effects on the performance of related devices.

Here, we present a systemic review of the Raman spectroscopy of graphene materials both in terms of the fundamental properties and device applications. First, we give a basic picture of the Raman spectroscopy of intrinsic 1LG, which is directly related to the electronic band structures and phonon dispersion curves. Secondly, the effect of the stacking (AB, ABC, and twist) and number of layers on the phonon modes is discussed. The resonant Raman scattering in 1LG and *N*LG is also presented. Then, the Raman spectra of 1LG under perturbation, including doping, strain, stress, temperature, and magnetic fields, are demonstrated. We discuss, in depth, the defects in graphene and their characterization using Raman spectroscopy, and demonstrate how to use the spectral features of Raman spectra to identify the number of layers of graphene materials. In the last three sections, we present some examples of the applications of Raman spectroscopy to graphene-related materials and devices, including GO, nanographene, epitaxial graphene grown from SiC, CVD-grown graphene, graphene-based heterostructures, field effect transistors (FETs), ion batteries, and solar cells. The application of Raman imaging is also presented in detail. We hope that this review will act as a guide for anyone who has an interest in the use of Raman spectroscopy with graphene-related systems and would like to employ Raman spectroscopy to characterize graphene-related materials and related devices.

2 Raman spectroscopy of monolayer graphene

2.1 Electronic band structure of monolayer and multilayer graphene

1LG is a single layer of carbon atoms with each atom bound to three neighbors in a honeycomb structure. The unit cell of its crystal lattice contains two carbon atoms, A and B, each forming a triangular in-plane network. The displacement of the A and B atoms, *i.e.*, the length of carbon–carbon covalent bond (a_{C-C}), is 0.142 nm, which results in a lattice constant of a = 0.246 nm, as shown in Fig. 2(a). *N*LG is a layered stacking structure prepared from 1LG in the out-of-plane direction (c-axis). The most common and stable stacking type is AB stacking, in which two adjacent graphene layers are stacked, oriented by a 60° rotation. From the top view, the empty centers of the hexagons on one layer are occupied by the carbon atoms at the hexagonal corner sites of the adjacent layers. Fig. 2(b) shows the atomic structure of the AB-stacked 2LG (AB-2LG). The typical value of the interlayer space is 0.35 nm. For AB-3LG, the atoms of the top layer are in the same positions as those of the second nearest layer from the top view, continuing in this manner for MLG with more layers. Thus, AB-3LG can be represented as ABA graphene and AB-4LG is ABAB graphene. Moreover, the unit cell of graphite can also be shown as in Fig. 2(b), having lattice constants of a = 0.246 nm and c = 0.67 nm. In reciprocal space, 1LG also has a honeycomb structure, as shown in Fig. 2(c). There are some high symmetry points within the first Brillouin zone (BZ) of 1LG: the Γ point at the zone center, the M points in the middle of the hexagonal sides,

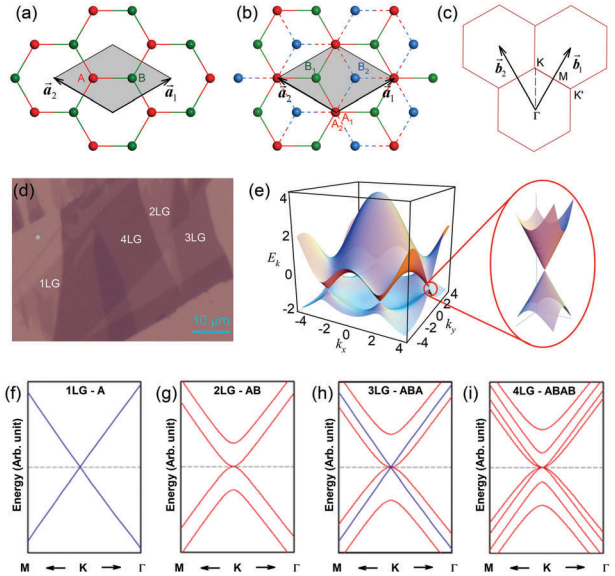

Fig. 2 (a) The top view of the unit cell of 1LG showing the inequivalent atoms A and B and unit vectors $\vec{a}_1$ and $\vec{a}_2$. (b) A top view of AB-stacked 2LG. (c) The unit cell of the reciprocal space of 1LG, showing the first Brillouin zone with its high symmetry points and axes. The primitive vectors $\vec{b}_1$ and $\vec{b}_2$ and high symmetry points are shown. (d) Optical image of *N*LG mechanically exfoliated on a SiO_2/Si substrate. (e) Band structure of 1LG. Reproduced with permission from ref. 104. Copyright 2009, American Physical Society. (f–i) Band structures of 1LG (f), AB-stacked 2LG (g), 3LG (h), and 4LG (i) in the vicinity of the *K* point near the Fermi level (shown by the horizontal gray dashed line).

and the *K* and *K*′ points at the corners of the hexagons, which are all inequivalent.

Mechanical exfoliation is an important method to produce *N*LG and can yield clean and extremely high-quality graphene.[1,105–107] Fig. 2(d) shows an optical image of an *N*LG flake on a SiO_2/Si substrate. Spreading graphene flakes on the SiO_2/Si substrate with a specific thickness (90 or 300 nm) of SiO_2 layer can make the graphene flake visible and enhance its Raman signal, an effect originating from optical interference effects in the air/*N*LG/SiO_2/Si multilayers.[108,109]

Graphene is a zero-gap semi-metal with a linear electronic band dispersion, which leads to its high mobility.[1,110] This band structure also gives rise to its unique optical properties.[23,111] Fig. 2(f–i) show the band structure of 1LG, AB-2LG, -3LG, and -4LG, respectively. The band structure of AB-2LG shows a parabolic line near the Fermi level, whereas that of AB-3LG is a composite of 1LG and AB-2LG band structures. The band structures from 1LG to 4LG (AB-stacked) are different because of the interlayer vdW coupling and changes in symmetry.[112,113] The band structure of *N*LG modifies the 2D mode profile of the corresponding Raman spectra by double resonant Raman scattering.[44,49] Thus, Raman spectroscopy can be used to probe the band structure of 1LG and 2LG,[44,114] as well as to identify the number of layers of *N*LG,[44,115] as will be discussed later.

2.2 Phonon dispersion and Raman spectrum of graphene

The phonon modes (lattice vibrations) of a crystal at the Γ point correspond to the irreducible representation of its symmetry group, which is essential for the interpretation of the Raman spectra. There are two and four atoms in the unit cell of 1LG and graphite, respectively, resulting in six and twelve phonon modes at the Γ point, respectively. The point group symmetries of 1LG and graphite are both D_{6h}. The lattice vibrations of 1LG and graphite at the Γ point can be expressed as: $\Gamma_{1LG} = A_{2u} + B_{2g} + E_{1u} + E_{2g}$ and $\Gamma_{bulk} = 2(A_{2u} + B_{2g} + E_{1u} + E_{2g})$, respectively.[56,118,119] The three acoustic modes in both 1LG and the bulk correspond to one A_{2u} mode and one E_{1u} (doubly degenerate) mode.[49,56] There are three optical phonon modes in 1LG, containing a doubly degenerate in-plane mode, E_{2g}, and one out-of-plane mode, B_{2g}, as shown in Fig. 3(a). In graphite, because the neighboring layers are inequivalent, Davydov splitting of the optical modes occurs.[49,56] The E_{2g} mode in 1LG generates an infrared-active E_{1u} mode and a Raman-active

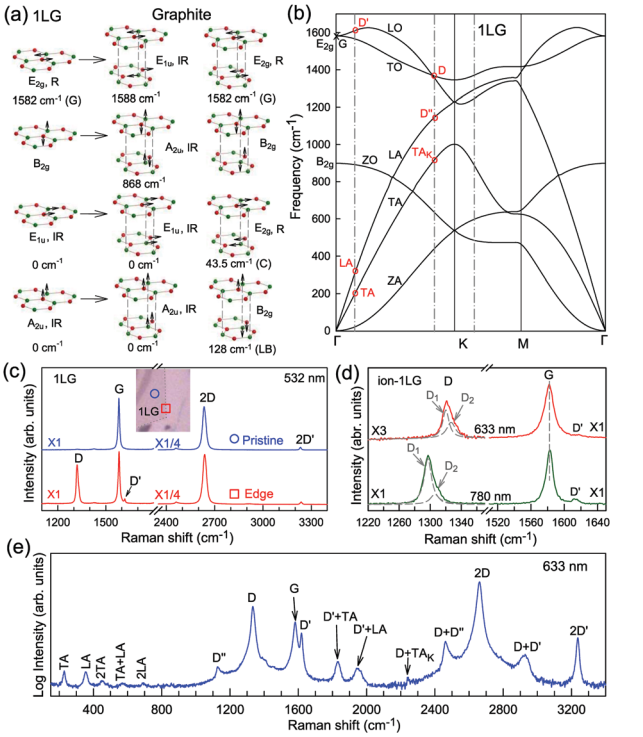

Fig. 3 (a) Normal mode displacements of phonon modes at the Γ points of 1LG and graphite, which show how each phonon mode in 1LG gives rise to two phonon modes of graphite. Red and green dots represent inequivalent carbon atoms. Black arrows show atom displacements for each mode. The Raman-active (R) and infrared-active (IR) modes are identified. (b) Phonon dispersion curves of 1LG calculated by density functional perturbation theory. Reproduced with permission from ref. 116. Copyright 2008, American Physical Society. The assignments of each phonon branch are labeled. (c) First- and second-order Raman spectra of pristine 1LG and at its edge (square), whose measured spots in the flake are labeled by circles and squares in the inset, respectively. (d) Comparison of Raman spectra with D, G, and D′ bands of ion-1LG for 633 and 780 nm excitation. The two components (D_1 and D_2) of the D mode are shown with Lorentzian fitting. The dashed lines are guides to the eye. (e) The expected Raman modes observed in graphite whiskers in the spectral region from 150 to 3400 cm^{-1} excited at 632.8 nm. Reproduced with permission from ref. 117. Copyright 2001, American Physical Society. All the first- and second-order Raman modes are assigned.

E_{2g} mode in graphite, and the B_{2g} mode in 1LG divides into an infrared-active A_{2u} mode and a silent B_{2g} mode. The remnant E_{2g} mode and one B_{2g} mode are the shear and layer-breathing (LB) modes, which correspond to the in-plane and out-of-plane interlayer vibrations of the rigid atomic layers, respectively.[118,120,121] The shear mode is referred to as the C mode in MLG because it provides a direct measurement of the interlayer *Coupling* and was first observed in MLG.[70] For some multilayer 2d materials, other notations of the shear modes, such as S and SM, have been introduced by various research groups.[54] The normal mode displacements and measured frequencies of the phonon modes of 1LG and graphite are shown in Fig. 3(a). The Raman active mode has been observed in 1LG and graphite at $\sim$1582 cm^{-1}, the so-called G mode. The G band is associated with the doubly degenerate (longitudinal optical (LO) and in-plane transverse optical (TO)) phonon mode (E_{2g} symmetry) at the BZ center and is a characteristic peak of graphene-related materials. The peak position of the G mode is sensitive to external perturbations, such as defects, doping, strain, and temperature and, thus, is widely used to probe the responses of graphene-based materials and related devices to external perturbations. However, owing to the weak interlayer vdW couplings, Pos(C) and Pos(LB), are very low (less than 130 cm^{-1}) and exhibit significant layer-number dependence in MLG, as discussed later.

Fig. 3(b) shows the phonon dispersion of 1LG calculated by density functional perturbation theory (DFPT) within the local density approximation,[116] which provides information about the atomic vibrations out of the BZ center. The phonon dispersion of 1LG has three acoustic and three optical branches inherited from the six vibrational modes at the Γ point. The three acoustic branches are the in-plane longitudinal acoustic (LA), transverse acoustic (TA), and out-of-plane acoustic (ZA) modes. The LA and TA branches have linear dispersion and higher frequencies than the ZA branch near the Γ point. The large slopes of the LA (21.36 km s^{-1}) and TA (13.79 km s^{-1}) branches result in the high in-plane sound velocity of graphene,[122,123] which is also responsible for the ultrahigh thermal conductivity of graphene.[124] The three optical branches are the LO, TO, and out-of-plane optical (ZO) branches, with the corresponding optical modes at the Γ point: E_{2g} (LO and TO) and B_{2g} (ZO) modes, as shown in Fig. 3(a and b). The LO and TO branches split when the phonon wave vector $\vec{q}$ is far from the Γ point, and the frequency of the TO branch monotonically decreases along the Γ–K axis. Inelastic X-ray and neutron scattering are the most common techniques used to detect the phonon dispersion of solid materials,[125,126] but they are not suitable for 2DMs because of the size limit. Raman spectroscopy can usually be used to probe the phonon modes at the BZ center. However, for graphene-based materials, the phonon modes far from Γ can also be probed by Raman spectroscopy *via* the double resonant Raman process.[69,127,128]

Fig. 3(c) shows two typical Raman spectra of pristine 1LG (at the sample center) and 1LG at its edge. The Raman spectrum of pristine 1LG consists of a set of distinct peaks in the spectral region from 1500–3400 cm^{-1}. Except for the G mode at around 1580 cm^{-1}, the 2D and 2D′ peaks appear around 2700 and 3240 cm^{-1}, respectively. The 2D peak arises from the overtone of TO phonons around the K point and is activated by triple resonance Raman scattering (TRRS); moreover, it is strongly dispersive with excitation energy because of a Kohn anomaly at the K point.[129] The 2D′ peak arises from the overtone of LO phonons around the Γ point, which is also activated by TRRS. The corresponding fundamental modes of the 2D and 2D′ peaks, *i.e.*, the D and D′ peaks, require a defect for their activation in the double resonance Raman scattering (DRRS), and, thus, they are absent in the Raman spectrum of pristine 1LG. Edges naturally exist in every graphene sample and are a kind of defect because the translational symmetry is broken. Thus, the D and D′ peaks are observed in the Raman spectrum of 1LG at its edge, as shown in Fig. 3(c). Defects can be introduced into 1LG by some techniques, such as ion-implantation, so that the D and D′ peaks can also be observed in ion-implanted 1LG (ion-1LG) and other kinds of disordered 1LG,[15,130,131] as shown in Fig. 3(d).

Besides the distinct D, G, D′, G, 2D, and 2D′ modes, other weak Raman modes can also be observed in 1LG. All of the expected Raman modes in 1LG have been observed in graphite whiskers.[117] The spiral structure and cone tip suggest the existence of a twist angle between adjacent layers in the whisker, leading to weaker interlayer coupling compared to graphite, similar to the case of twisted 2LG with small twist angle.[57] Therefore, the graphite whisker exhibits a typical Raman spectral feature identical to that of graphene, such as a single Lorentzian 2D peak and much stronger intensity of the 2D mode relative to the G mode (I(2D) $\backsimeq$ 13I(G) in Fig. 3(e)). Therefore, graphite whiskers are considered to be a prototype to show the abundant Raman modes that should be observed in 1LG. Indeed, many weak first- and second-order Raman modes have been revealed in its Raman spectrum, as indicated in Fig. 3(e), which can be well understood by DRRS or TRRS based on the phonon dispersion of 1LG, as discussed later.

2.3 The principle of double and triple resonance Raman scattering in graphene

The peculiar band structures of graphene and other materials result in the corresponding Raman modes being involved in the resonant Raman process, *e.g.*, the case of graphene depicted in Fig. 4. In principle, according to the fundamental Raman selection rule of momentum conservation,[132] a one-phonon mode of an intrinsic crystal at the Γ point can be Raman active if it is symmetry allowed. In fact, the G-band is the only band originating from a normal first-order Raman scattering process in graphene systems. When the excitation energy is chosen to match or be near to an optical transition bandgap of the crystal, the Raman intensity can be enhanced by orders of 2 to 6, so-called resonant Raman spectroscopy. Because two linear electronic bands of intrinsic 1LG cross at the Fermi energy, an incoming photon with energy ε_L can always excite a resonant transition from state a in the valence band to state b in the conduction band with $\varepsilon_L = E_b\left(\vec{k}\right) - E_a\left(\vec{k}\right)$, where $E_b\left(\vec{k}\right)$ and $E_a\left(\vec{k}\right)$ are the energies of the electrons in the conduction and valence bands with momentum $\vec{k}$, respectively. The excited

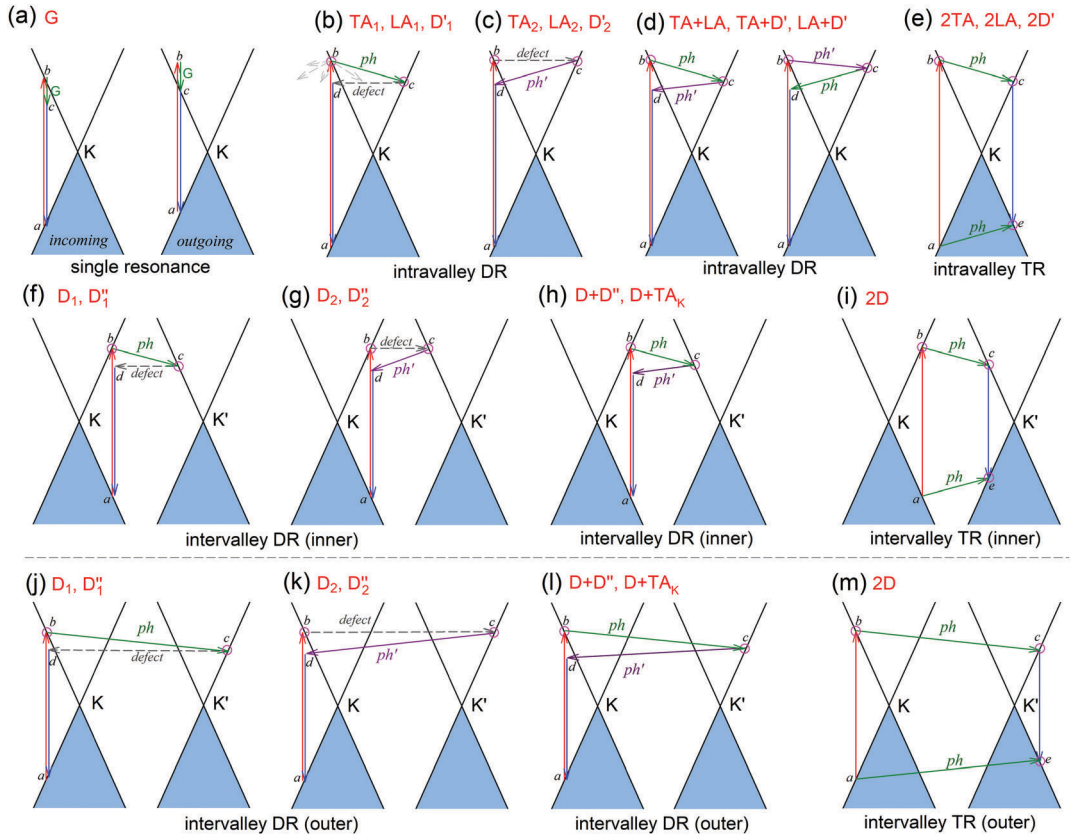

Fig. 4 (a) Incoming and outgoing single resonance processes of the G mode in 1LG. (b–i) Resonant processes of dispersive Raman modes in 1LG, including an electron–hole pair excited by an incident laser photon, inelastic scattering of the electron and hole by phonon emission/absorption, and elastic scattering of the electron mediated by the defect, and recombination of the electron–hole pair. (b–d) The intravalley double resonance processes. (e) An intravalley triple resonance process. (f–h) The inner intervalley double resonance processes. (i) An inner intervalley triple resonance process. (j–l) The outer intervalley double resonance processes. (m) An outer intervalley triple resonance process. The inner DR process activates the phonons along the K–Γ axis, while the outer DR process activates the phonons along the K–M axis. The Raman modes in graphite whiskers activated by each resonance process are labeled accordingly in each panel.

electron can be scattered by the E_{2g} phonons to recombine with a hole, satisfying the incoming single resonance process. The outgoing single resonance process can also be satisfied for the G mode of 1LG. Both resonance processes are shown in Fig. 4(a).

The excited electron $\left(E_b\left(\vec{k}\right)\right)$ can also be scattered by phonons of an arbitrary wave vector, $\vec{q}$, as shown in Fig. 4(b) by the dashed arrows. The scattering probability, however, will be particularly high if the phonon scatters the electron from the real electronic state b into another real state c. If the electronic transition $b \rightarrow c$ is allowed, for a given phonon and electron dispersion, the scattering process is only fulfilled by one pair of phonon energies, $\hbar\omega_{ph}$, and phonon wave vector, $\vec{q}_{ph}$; thus, the electron energy at state c is $E_c\left(\vec{k}+\vec{q}_{ph}\right)$ and $E_b\left(\vec{k}\right) - E_c\left(\vec{k}+\vec{q}_{ph}\right) = \hbar\omega_{ph}$ to maintain energy conservation. Such one-phonon first-order Raman scattering is forbidden by selection rules. However, the electron at state c can be scattered back to the state d with wave vector $\vec{k}$ by crystal defects, which then emits a photon by recombining with a hole at state a, as depicted in Fig. 4(b). The above resonant process is one-phonon second-order Raman scattering, where the two scattering processes consist of one inelastic scattering event by emitting a phonon and one elastic scattering event by crystal defects. This scattering process yields the double resonance condition where $E_b\left(\vec{k}\right)$ is always one of the resonant electronic states and $E_c\left(\vec{k}+\vec{q}_{ph}\right)$ is the second resonant state. The two scattering processes can also start from an elastic scattering event followed by an inelastic scattering event (Fig. 4(c)).

If the elastic scattering of defects, such as the electron from $E_c\left(\vec{k}+\vec{q}_{ph}\right)$ to a virtual state d in Fig. 4(b) or from $E_b\left(\vec{k}\right)$ to $E_c\left(\vec{k}+\vec{q}_{ph}\right)$ in Fig. 4(c), is displaced by another inelastic phonon scattering, the process becomes two-phonon second-order Raman scattering, as illustrated in Fig. 4(d). Further, if the valence and conduction bands are almost mirror bands, a TR Raman process can occur. For example, for the special case of 1LG, as shown in Fig. 4(e), the photo-excited electron can be scattered by a phonon (ω_{ph}) with $\vec{q}_{ph}$; meanwhile, the photo-excited hole can be scattered by a phonon (ω_{ph}) with $-\vec{q}_{ph}$. In this case, the electron–hole generation is a resonant process, and both electron and hole scattering will be resonant.

Finally, the electron–hole recombination will also be resonant. Therefore, for the TR Raman process, all steps in the normal double resonance process become resonant.

The resonance processes in Fig. 4(b–e) are intravalley double resonance processes because two resonant electronic states are connected within the same Dirac cones at the K point (or the K' point) of 1LG. Instead, if the resonance process connects two associated resonant electronic states within the two inequivalent Dirac cones at the K and K' points of 1LG, the corresponding double resonance mechanism is called an intervalley process. By analogy to the intravalley DR and TR processes in Fig. 4(b–e), the intervalley DR and TR processes also occur, as shown in Fig. 4(f–i). The double resonance processes in Fig. 4 only depict the incoming resonance process. The outgoing resonance process can also occur; thus, there are four possible resonant processes of fundamental and combination Raman modes because the order of the two scattered phonons leads to phonons with various wave vectors, $\vec{q}_{\mathrm{ph}}$. However, the selected wave vector of the phonon produced by the outgoing resonance process is equal to that of the corresponding incoming resonance process. Finally, there are two inequivalent double resonant processes for the fundamental and combination Raman modes mediated by the scattering of electrons. Two inequivalent processes for combination Raman modes are degenerate for the overtone, so there is only one double resonant process for the overtone mediated by the scattering of electrons. It should be pointed out that the inelastic scattering of the hole by phonon emission/absorption and elastic scattering of the hole mediated by the defect can also be involved in the DR Raman process.[56]

In principle, many different initial electronic states around the Dirac point and phonons with different symmetries and wave vectors can satisfy the DR conditions. However, considering (1) the existence of singularities in the density of phonon states that satisfy the DR condition, (2) the angular dependence of the electron–phonon scattering matrix elements, and (3) destructive interference effects when the Raman transition probability is calculated, only a few specific DR processes contribute to the observed Raman modes. Because there are two inequivalent DR Raman processes for both intravalley and intervalley DR Raman processes, each ε_{L} can select two phonon wave vectors of $\vec{q}_{\mathrm{ph}}$ and $\vec{q}_{\mathrm{ph}'}$ for the fundamental and combination modes and one phonon wave vector of $\vec{q}_{\mathrm{ph}}$ for the overtones near the Γ and K points, respectively. Because the phonon energy in 1LG is much smaller than ε_{L}, $\vec{q}_{\mathrm{ph}}$ is almost equal to $\vec{q}_{\mathrm{ph}'}$. Thus, in principle, for each ε_{L}, the phonons with almost equal $\vec{q}_{\mathrm{ph}}$ at different branches of the phonon dispersion curves can be probed by the DR Raman process. These are linked by the vertical dotted-dashed lines close to the Γ and K points, respectively, for the intravalley and intervalley DR Raman processes in Fig. 3(b).

2.4 Understanding the Raman spectrum of graphene based on resonance Raman scattering

In 1LG, only the G mode is Raman active at the Γ point. The other observed Raman modes in Fig. 3(c and e) originate from the DR or TR Raman scattering in which one phonon or two phonons are involved. These Raman modes can be assigned based on the electronic band structures and phonon dispersion curves of 1LG, as labeled in Fig. 3(c–e). The Raman modes associated with one-phonon DR Raman process can only be observed in the presence of defects because defects are necessary to activate such Raman processes. However, the combination modes and overtones can be observed in the defect-free 1LG. The possible DR Raman process for each mode is depicted in Fig. 4(b–i). Because $\hbar\omega_{\mathrm{ph}} \ll \varepsilon_{\mathrm{L}}$, once a phonon with $\vec{q}_{\mathrm{ph}}$ in one branch satisfies the requirement of the DR Raman process, the other phonons with $-\vec{q}_{\mathrm{ph}}$ should also satisfy the requirement. Therefore, for each ε_{L}, the phonons in the different branches (linked by three vertical lines in Fig. 3(b)) can satisfy the requirements of the intravalley or intervalley DR Raman processes. However, because of different electron–phonon coupling for different phonon branches, not all the phonons excited by ε_{L} can be observed in the Raman spectra.

The well-known D and 2D bands originate from intervalley one-phonon and two-phonon DR Raman scattering between two nonequivalent Dirac cones (K and K'), respectively, involving one TO phonon near the $K(K')$ point and one defect in the case of the D band and two TO phonons for the 2D band.[69,133] The two inequivalent one-phonon DR processes separately activate one TO phonon near the K point so that the observed D mode actually has an asymmetrical profile that can be fitted by two Lorentzian subpeaks, as shown in Fig. 3(d) for the experimental result and in Fig. 4(f and g) for their resonance processes. The intervalley TR resonance process of the 2D mode is depicted in Fig. 4(i). For the intervalley DR process, Fig. 4(f–i) only depict the inner intervalley DR or TR processes, which activate the phonons along K–Γ. Although the outer DR (or TR) processes (Fig. 4(j–m)) can also satisfy the DR (or TR) conditions and activate the phonons along the K–M axis, the main contribution to both the D and 2D modes is from the phonons along the Γ–K axis according to the numerical calculations.[80]

The phonon at the LA branch near the K point can also be activated by a defect in the intervalley DR process, which has been observed at $\sim$1150 cm^{-1} in graphite whiskers and is assigned to the D″ peak.[117,128,134–136] In 1LG, an asymmetrical Raman peak is observed at $\sim$2450 cm^{-1}, whose intensity is comparable to that of the 2D′ mode. The assignment of this mode has puzzled scientists for a long time because it also appears in graphite.[117,128,135,136] This mode is also observed in graphite whiskers and has been assigned to the D + D″ peak,[117] and was confirmed by later theoretical work, see ref. 80 and 137. A very weak peak at $\sim$2250 cm^{-1} has been observed in graphene whiskers and other carbon materials. It can be assigned to the D + TA$_K$ mode, which is a combination of a D phonon and a phonon belonging to the TA branch near the K point.[80] It should be noted that the fundamental TA$_K$ mode has not been observed in carbon materials. All these modes result from the intervalley DR processes of the fundamental and combination modes, as depicted in Fig. 4(f–h).

The well-known D′ ($\sim$1620 cm^{-1}) and 2D′ ($\sim$3240 cm^{-1}) bands originate from intravalley one-phonon and two-phonon

DR Raman processes, respectively, involving one LO phonon near the Γ point and one defect in the case of the D′ band and two LO phonons for the 2D′ band.[138] The asymmetrical profile of the D mode cannot be revealed for the D′ mode because of its weak intensity and the small dispersion of the corresponding LO phonon near the Γ point. The TA and LA phonons near the Γ point can also be activated by defects in the one-phonon DR intravalley Raman process. There have been few reports on the corresponding Raman modes in 1LG, but they have been observed in graphite whiskers and are assigned as TA and LA modes (Fig. 3(e)), which also exhibit asymmetrical spectral profiles. Their combination modes (TA + LA) and overtones (2TA, 2LA) are also observed in graphite whiskers (Fig. 3(e)). The typical intravalley combination modes are the D′ + TA and D′ + LA modes, which can be clearly observed in 1LG. The two modes are, respectively, a combination of a D′ phonon with the TA and LA phonons, which have opposite $\vec{q}$ with respect to the D′ phonon.[80,122,123] The intravalley DR processes of the fundamental and combination modes are depicted in Fig. 4(b–d), and the intravalley TR process of the overtone is depicted in Fig. 4(e).

Obviously, the frequency of Raman modes is usually independent of ε_L because these Raman modes usually arise from optical phonons at the Γ point and the quasi-momentum of a photon is usually much smaller than the phonon wave vector at the zone edge. However, for DR or TR Raman processes, as depicted in Fig. 5, the wave vector ($\vec{q}_{ph}$) of the involved phonons is determined by ε_L.[122,123,129,133,139] Thus, the peak position of the corresponding Raman mode is dependent on ε_L. For example, as shown in Fig. 5(a and b), Pos(2D) of graphene is dispersive with a slope of $\sim$100 cm^{-1} eV^{-1}, which is twice that of the D mode. Similar behavior has been observed in various graphite materials. It is also well known that the frequencies of the Stokes and anti-Stokes components of a Raman mode should be equal to each other. However, the wave vectors of phonons involved in the Stokes and anti-Stokes DR and TR Raman processes are different from each other. Therefore, there exists a frequency discrepancy between the Stokes and anti-Stokes components of the dispersive Raman modes. Such a frequency discrepancy had been observed in other graphene-based materials, such as bulk graphite,[135] graphite whiskers,[117] and multi-walled carbon nanotubes.[128]

In contrast to the unpolarized G mode, the intensities of the D, D′, 2D, and 2D′ peaks of disordered graphene are dependent on the polarization configuration of Raman scattering, as shown in Fig. 5(c), because of the selective optical absorption and emission mediated by electron–phonon coupling.[80,117,140,141]

Besides graphene, the DR Raman process is also present in other graphene-based materials, such as graphite, carbon nanotubes, and mutlilayer graphenes, although they do not have linear band structures.

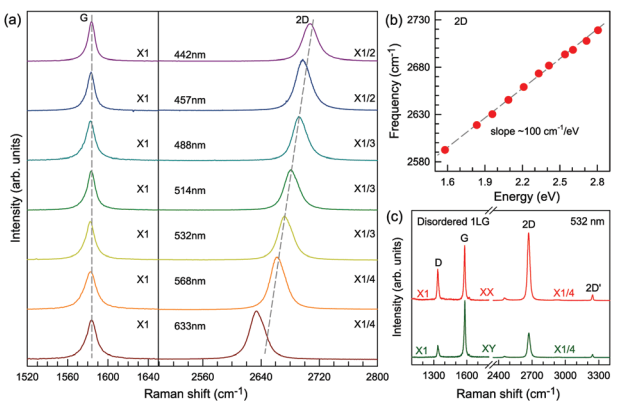

Fig. 5 (a) Raman spectra of 1LG measured at various excitations in the G and 2D mode regions. (b) 2D-peak position as a function of excitation energy, and the slope is 100 cm^{-1} eV^{-1}. (c) Raman spectra of disordered 1LG induced by ion-implantation in both parallel (XX) and cross (XY) polarizations.

3 Raman spectroscopy of multilayer graphene

3.1 Group theory of AB-stacked multilayer graphene

Lattice vibrations can be classified based on the irreducible representation of the symmetry groups of the crystal. Table 1 presents the space groups for 1LG, AB-*N*LG, and graphite and the corresponding point groups at the high symmetry points.[49] Because the phonon along the Γ–K (T) axis mainly contributes to the DR Raman process in graphene,[80] the symmetry information along the Γ–K direction is also shown. Both 1LG and graphite have D_{6h} symmetry, and even *N*LG (ENLG) has D_{3d} symmetry, whereas odd *N*LG (ONLG) ($N \geq 3$) has D_{3h} symmetry.

The first-order Raman process usually occurs at the Γ point because of momentum conservation. The Raman-active modes can be revealed by looking at the quadratic form of the basis function corresponding to the representation. The irreducible representations of 1LG and *N*LG for the lattice vibrations (Γ_{vib}) at the Γ point and along the Γ–K direction in the first BZ are listed in Table 2. The notations of both Bethe and Mulliken are adopted here. A more complete group theory analysis for every high symmetry point inside the first BZ and its dependence on the number of layers can be found in ref. 142. The irreducible representations of the lattice vibrations (Γ_{vib}) at Γ are summarized for 1LG, AB-2LG, and AB-3LG with Mulliken notation as follows:

$$\Gamma_{1LG} = A_{2u} + B_{2g} + E_{1u} + E_{2g},$$

$$\Gamma_{AB\text{-}2LG} = 2(A_{1g} + E_g + A_{2u} + E_u),$$

$$\Gamma_{AB\text{-}3LG} = 2A_1' + 4A_2'' + 4E' + 2E''$$

Table 1 The space groups for 1LG, AB-*N*LG, and graphite and the point groups at the high symmetry points in the Brillouin zone

		Point group			
	Space group	Γ	$K(K')$	M	$T(\Gamma$–$K)$
1LG	$P6/mmm$	D_{6h}	D_{3h}	D_{2h}	C_{2v}
*N*LG even	$P\bar{3}m1$	D_{3d}	D_3	C_{2h}	C_2
*N*LG odd	$P\bar{6}m2$	D_{3h}	C_{3h}	C_{2v}	C_{1h}
Graphite	$P6_3/mmc$	D_{6h}	D_{3h}	D_{2h}	C_{2v}

Table 2 The irreducible representations for the lattice vibrations of 1LG and *N*LG (even and odd) at the Γ point and along the $T(\Gamma$–$K)$ lines. Both notations of Bethe and Mulliken are given

	Notation	1LG	*N*LG even	*N*LG odd
Γ	Bethe	$\Gamma_2^- + \Gamma_5^- + \Gamma_4^+ + \Gamma_6^+$	$N(\Gamma_1^+ + \Gamma_3^+ + \Gamma_2^- + \Gamma_3^-)$	$(N-1)\Gamma_1^+ + (N+1)\Gamma_2^- + (N+1)\Gamma_3^+ + (N-1)\Gamma_3^-$
	Mulliken	$A_{2u} + B_{2g} + E_{1u} + E_{2g}$	$N(A_{1g} + E_g + A_{2u} + E_u)$	$(N-1)A_1' + (N+1)A_2'' + (N+1)E' + (N-1)E''$
$T(\Gamma$–$K)$	Bethe	$2T_1 + T_2 + 2T_3 + T_4$	$3N(T_1 + T_2)$	$(3N+1)T^+ + (3N-1)T^-$
	Mulliken	$2A_1 + A_2 + 2B_1 + B_2$	$3N(A + B)$	$(3N+1)A' + (3N-1)A''$

We take AB-2LG as an example to show the different lattice vibrations in MLG with respect to 1LG. There are nine optical modes at Γ in AB-2LG. The G band in AB-2LG belongs to the E_g irreducible representation, which is doubly degenerate. The E_g mode represents the atomic motion of the nearest neighbor carbon atoms moving against each other within the plane and in phase between the two layers, denoted as the symmetric G mode.[49] The E_u representation is not Raman active in AB-2LG because of the lack of inversion symmetry in the D_{3h} point group. This mode represents the atomic motion of the nearest neighbor carbon atoms moving against each other within the plane but out-of-phase between the two layers, denoted as the antisymmetric G band.[49] This E_u mode can become active if this inversion symmetry operation is broken by the presence of twisted stacking,[57,143,144] doping,[145,146] and strain.[147] There also exists an ultralow-frequency (ULF) E_g mode at $\sim$31 cm^{-1}, which corresponds to the interlayer rigid shear vibration.[70] The other two A_{1g} irreducible representations give rise to phonon modes at $\sim$90 cm^{-1} and $\sim$867 cm^{-1}.[71,148,149] The mode at $\sim$90 cm^{-1} corresponds to the interlayer breathing vibration normal to the basal plane, which is denoted as the LB mode.

With increasing *N*, the atomic displacements of each phonon vibration in AB-*N*LG become more complicated. In AB-3LG, the corresponding G and C modes are assigned to be E′ and E″ representations, and the out-of-plane vibrational modes are assigned to A_1' and A_2'' representations, respectively.

3.2 High-frequency Raman spectra of AB-stacked multilayer graphene

The Raman spectra of MLG consist of two fundamentally different sets of peaks. Those, such as D, G, 2D, *etc.*, also present in 1LG and arise from in-plane vibrations and others, such as the C and LB modes, arise from the relative motions of the planes themselves, either perpendicular or parallel to the normal direction. In *N*LG, all vibrational modes split due to the confinement in the direction perpendicular to the basal plane. In the high-frequency region, because of the weak interlayer coupling in MLG, the peak position of the G mode, Pos(G), in the intrinsic *N*LG is almost $\sim$1582 cm^{-1} and is not sensitive to *N*. However, because *N*LGs with fewer than ten layers show distinctive band structures, the peak parameters of the Raman modes activated by the DR Raman process (*e.g.*, the 2D mode) in *N*LG are significantly dependent on *N*.

Fig. 6(a–c) shows the Raman spectra of 1LG and AB-stacked 2–5LGs excited by a 633 nm laser and AB-stacked 4–5LGs excited by a 532 nm laser. Indeed, all the G peaks are at around

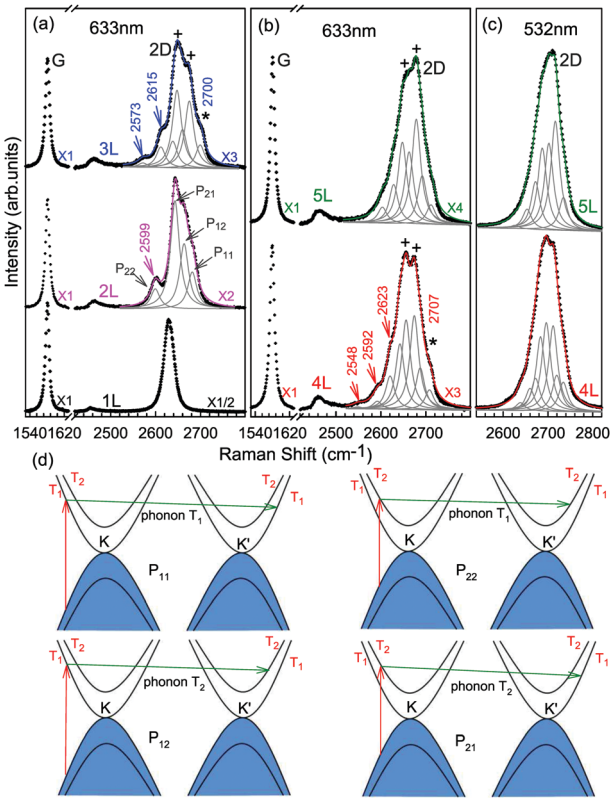

Fig. 6 Raman spectra (dotted curves) of G and 2D peaks for AB-stacked 1–3LGs measured using a 633 nm laser (a) and those of AB-stacked 4–5LGs excited by both 633 (b) and 532 nm lasers (c). The 2D peaks are fitted by Lorentzian line shapes (gray peaks). The solid lines with colors are the sum of fitted Lorentzian curves. The arrows, crosses, and stars indicate the weak shoulders at the low energy side of the 2D peaks for AB-stacked 2–4LGs, the strongest components of the 2D peaks for AB-stacked 3–5LGs, and the high energy side of the 2D peaks for AB-stacked 3–4LGs, respectively. Reproduced with permission from ref. 115. Copyright 2010, American Physical Society. (d) The four allowed DR processes in AB-2LG. According to the scattering order of the phonon, the four DR processes are denoted as P_{11}, P_{22}, P_{12}, and P_{21}, respectively, and the corresponding 2D components are marked in (a).

1582 cm^{-1} and can be fitted with a single Lorentzian line shape.[44] 1LG has a single 2D peak at 2629.7 cm^{-1}. The 2D band of AB-2LG can be well fitted with four Lorentzian peaks.[44,115,142] Under 633 nm excitation, five and six 2D components can be identified in the Raman spectra of AB-stacked 3–4LG, as shown in Fig. 6(a and b) by arrows, crosses, and stars. These spectral features can be used to clearly identify *N* of *N*LG up to four if a Raman system with a high resolution (better than 1.0 cm^{-1}) is

used. Because the different components of the 2D bands may exhibit different resonant behaviors with laser excitation,[114] it is very important to choose an appropriate laser wavelength (longer than 630 nm) to identify the number of layers of graphene flakes by Raman spectroscopy.[115] For example, the 2D band of AB-4LG excited by 633 nm laser light shows more distinct spectral features than that by 532 nm excitation. The D mode of disordered *N*LG also exhibits similar spectral features to the corresponding 2D mode.

Because of the existence of several electronic bands in MLG and several possible DR Raman processes, many 2D components may be expected in MLG. How many 2D components actually exist in *N*LG is determined by the selection rules of the electron–photon and electron–phonon couplings in the DR Raman process. The symmetries of the electrons and phonons can be obtained from space group analysis. Taking AB-2LG as an example, the number of allowed DR processes will be larger than 1LG because both electronic and phonon branches are doubled. Along the T direction in the BZ, the transitions of $T_1 \rightleftharpoons T_2$ are allowed in AB-2LG, as shown in Fig. 6(d).[80,110,142] The TO phonons for AB-2LG have T_1 and T_2 symmetries. For the electron scattering by a T_1 phonon, the allowed process should occur between K and K' electronic bands with the same symmetry $T_1 \rightarrow T_1$ or $T_2 \rightarrow T_2$. This also happens for the electron scattering by a T_2 phonon but it connects conduction bands of different symmetries, *i.e.*, $T_1 \rightleftharpoons T_2$. This gives rise to four possible DR processes, as shown in Fig. 6(a). The 2D components associated with the four DR processes have been clearly observed in the Raman spectra of AB-2LG, as shown in Fig. 6(a). The case for AB stacked 3–5LG is more complex according to point group analysis.[142] However, because of the possible degeneracy and overlapping of these peak components, the number of observed components is much lower than the theoretical one. To obtain good fits, six and eight components are, respectively, required for the 2D bands of AB-3LG and AB-4LG if the peak widths of all components are kept as a fixed constant of 24 cm^{-1} in the fitting process.[115]

Besides the D and 2D modes, other Raman modes in *N*LG activated by DR Raman process also show *N*-dependent spectral features, such as the LA + D′, TA + D′, and D + D″ modes.

3.3 Ultralow-frequency Raman spectra of AB-stacked multilayer graphene

The Raman modes of AB-MLG in the ultralow-frequency region are mainly related to the interlayer C and LB vibrations.[53,54,70] There are $N-1$ degenerate pairs of C modes and $N-1$ LB modes for AB-*N*LG, which are denoted as C_{NN-i} and LB_{NN-i} ($i = 1, 2, \ldots, N-1$), respectively, where C_{N1} (LB_{N1}) (*i.e.*, $i = N-1$) has the highest frequency and C_{NN-1} (LB_{NN-1}) (*i.e.*, $i = 1$) has the lowest frequency. The C and LB modes can be Raman active (R), infrared active (IR) or both, depending on the symmetry of *N*LG and the number of layers (N).[53,54,57,71,150] The symmetry can be divided into D_{3d} for ENLG and D_{3h} for ONLG, as discussed above.[53,142,150] The $N-1$ C modes in ENLG and ONLG can be represented by $\frac{N}{2}E_g(R) + \frac{N-2}{2}E_u(IR)$ and $\frac{N-1}{2}E''(R) + \frac{N-1}{2}E'(R, IR)$, respectively, where E_g and E″ are Raman active, E_u is IR active, and E′ is both Raman and IR active. According to their Raman tensors, only E_g and E′ can be observed in the backscattering configuration. $N-1$ LB modes in ENLG and ONLG are represented by $\frac{N}{2}A_{1g} + \frac{N-2}{2}A_{1u}$ and $\frac{N-1}{2}A_2'' + \frac{N-1}{2}A_1'$, respectively, in which A_{1g} and A_1' are Raman active and A_{1u} and A_2'' are IR active.

Because the C and LB modes are rigid layer lattice vibrations, ω(C) and ω(LB) can be identified by regarding each graphene layer in AB-MLG as a single ball so that AB-*N*LG can be simplified as a linear chain with N balls in which only nearest-neighbor interlayer interaction is considered. This is known as the linear chain model (LCM).[70,151] By assuming that the force constant of the interlayer coupling per unit area is $\alpha_0^{\parallel}$ ($\alpha_0^{\perp}$) for the C (LB) modes, the frequencies ω (in cm^{-1}) of the $N-1$ C and LB modes can be calculated by solving the corresponding $N \times N$ (tridiagonal) dynamical matrix as follows:[70,71]

$$(\omega_i)^2\mathbf{u}_i = \frac{1}{2\pi^2 c^2 \mu}\mathbf{D}\mathbf{u}_i, \quad (1)$$

where the $\mathbf{u}_i$ is the phonon eigenvector with mode i and frequency ω_i, $\mu = 7.6 \times 10^{-27}$ kg Å^{-2} is the monolayer mass per unit area, $c = 3.0 \times 10^{10}$ cm s^{-1} is the speed of light, and $\mathbf{D}$ is the shear or layer-breathing part of the force constant matrix. Thus, the frequency of the C_{NN-i} and LB_{NN-i} modes can be given by[53,54,70,71]

$$\omega(C_{NN-i}) = \frac{1}{\pi c}\sqrt{\alpha_0^{\parallel}/\mu}\sin(i\pi/2N), \quad (2)$$

$$\omega(LB_{NN-i}) = \frac{1}{\pi c}\sqrt{\alpha_0^{\perp}/\mu}\sin(i\pi/2N), \quad (3)$$

respectively, where $i = 1, 2, \ldots, N-1$. Accordingly, the ith displacement eigenvector $v_j^{(i)}$ is

$$v_j^{(i)} = \cos[i(2j-1)\pi/2N] \quad (4)$$

where j labels the layers. In the case of bulk graphite, $N \rightarrow \infty$, $\omega(C_{bulk}) = \frac{1}{\pi c}\sqrt{\alpha_0^{\parallel}/\mu}$, and $\omega(LB_{bulk}) = \frac{1}{\pi c}\sqrt{\alpha_0^{\perp}/\mu}$, which are $\sqrt{2}$ times of $\omega(C_{21})$ and $\omega(LB_{21})$, respectively. $\omega(C_{bulk})$ was measured as 43.5 cm^{-1},[152] while $\omega(LB_{bulk})$ was estimated as $\sim$125.3 cm^{-1} based on the Pos(LB) measurements in *t*MLGs,[57,71] and, thus, $\alpha_0^{\parallel} = 12.8 \times 10^{18}$ N m^{-3} and $\alpha_0^{\perp} = 106.5 \times 10^{18}$ N m^{-3}. Therefore, eqn (2) can be simplified as follows:

$$\omega(C_{NN-i}) = \omega(C_{bulk})\sin(i\pi/2N), \quad (5)$$

$$\omega(LB_{NN-i}) = \omega(LB_{bulk})\sin(i\pi/2N), \quad (6)$$

Once the normal mode displacements corresponding to ω(C) and ω(LB) have been obtained, the symmetry and Raman activity of the C and LB modes can be deduced.[53,54,57,70,71] As examples, Fig. 7(a and b) depict the frequencies and the corresponding normal mode displacements for $N-1$ C and LB modes in AB-stacked 2–4LG, respectively. Fig. 7(c and d) plot all the C and LB modes as a function of N, respectively, in

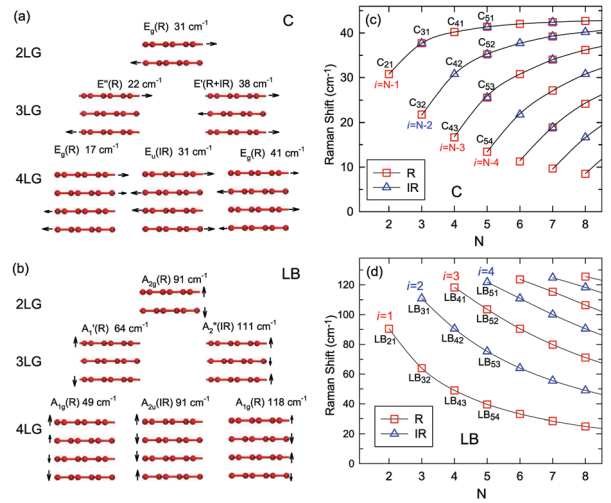

Fig. 7 Symmetry, frequency, Raman activity, and normal mode displacement for each C mode (a) and LB mode (b) of AB-(2–4)LG. The frequencies of C (c) and LB (d) modes as a function of number of layers calculated by LCM and 2LCM, respectively. The rectangles and triangles indicate the Raman and infrared active modes, respectively. Reproduced with permission from ref. 150. Copyright 2016, Elsevier.

which the Raman-active and infrared-active modes are also identified. The C modes in Fig. 7(c) are plotted with the branches of $i = N - 1, N - 2,\ldots$, because only the C_{N1} modes are observed in the intrinsic MLG at room temperature.[70] The LB modes in Fig. 7(d) are plotted with the branches of $i = 1, 2, 3,\ldots$, because all the LB modes in the branches of $i = 2n - 1$ ($n = 1, 2, 3,\ldots$) are Raman active.

Based on the LCM, if $\alpha_0^{\parallel}$ and $\alpha_0^{\perp}$ are independent of N in AB-MLG, ω(C) and ω(LB) in AB-MLG are determined by $\omega(C_{bulk})$ and $\omega(LB_{bulk})$. In the intrinsic AB-MLG, whether the C or LB modes can be experimentally observed relies on their Raman activity, the strength of the electron–phonon coupling (EPC), and the appropriate polarization configuration. Fig. 8(a) plots

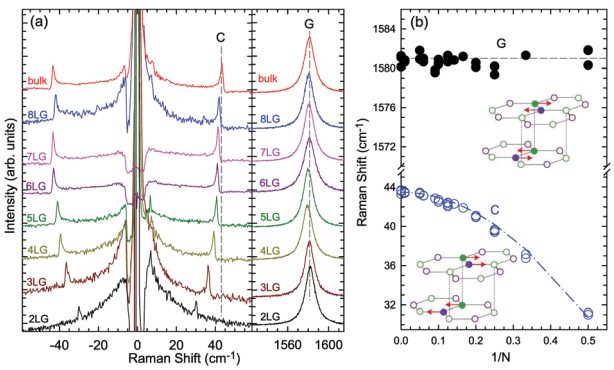

Fig. 8 (a) Stokes Raman spectra of the C peak (left) and G peak (right) for AB-stacked 2–8LG and bulk graphite. (b) The position of the G peak (filled black circles) and C peak (open blue circles) as a function of inverse number of layers. The red dashed-dotted line was calculated by LCM. The insets show the atomic displacements of the C and G modes. The vertical dashed lines in (a) and the horizontal line in (b) are eye guides. Reproduced with permission from ref. 70. Copyright 2012, Nature Publishing Group.

the C mode, as well as the G mode, of AB-stacked 2–8LG and bulk graphite,[70] whereas Fig. 8(b) shows the positions of these two modes as a function of $1/N$. In contrast to the G peak, which remains constant at $\sim$1582 cm^{-1}, $\omega(C)$ decreases monotonically with decreasing N. The N-dependent ω(C) can be well fitted by $\omega(C_{N1}) = \omega(C_{bulk})\cos(\pi/2N)$ based on the LCM,[70] which suggests that $\alpha_0^{\parallel}$ remains constant at 12.8 $\times$ 10^{18} N m^{-3} in AB-NLG. Concerning the line shape, the G peaks maintain Lorentzian line shapes, while the C modes display a unique profile asymmetry and can be well fitted by the Breit–Wigner–Fano (simplified as Fano) line shape. Details about the line shapes of the C modes will be discussed later. Unlike the C modes, the LB modes of AB-NLG cannot be observed directly at room temperature because of the weak EPC.[70] However, these modes have been observed either indirectly (*via* overtones and combination modes)[153] or by increasing the laser power (heating).[154]

Overall, the LCM can predict the N-dependence of ω(C) in NLG and the constant interlayer interaction of $\alpha_0^{\parallel}$ from AB-2LG to bulk graphite. The LCM discussed above could be applied to the C and LB modes of all 2D materials, such as MoS_2, WSe_2, black phosphorus (BP), ReS_2, $ReSe_2$, and even 2D heterostructures.[151,155–167] Because ω(C) and ω(LB) are significantly dependent on the number of layers, N, the C and LB modes can be used to identify the thickness or number of layers of two-dimensional material flakes.[151,155,167,168]

3.4 Raman spectra of ABC-stacked multilayer graphene

Stacking order has a strong impact on the electrical and optical properties of MLG. Apart from the AB stacking, ABC (rhombohedral) stacking is also common in NLG. Lui *et al.*[169] found that $\sim$85% of the area in graphene flakes corresponds to ABA stacking and the remaining $\sim$15% corresponds to ABC stacking, which is in agreement with the X-ray diffraction study on bulk graphite.[170] The spectral profiles of the 2D mode are quite different for AB- and ABC-stacked NLG,[5,6,150,171] which reflects their different electronic structures. Taking 3LG as an example, Fig. 9(a) plots the G and 2D modes of ABC- and AB-stacked 3LG. Similar to the DR Raman process in AB-2LG discussed above, the three degenerate TO phonons in 3LG can couple to all electron bands, in theory generating fifteen sub-peaks for AB-stacked 3LG; however, the profiles can be well-fitted using six sub-peaks, as shown by dashed-dotted lines in Fig. 9(a).[142] In ABC-3LG, the 2D mode is more asymmetrical. Additionally, the G mode of ABC-stacked 3LG ($\sim$1581 cm^{-1}) is 1 cm^{-1} red shifted compared to that of AB-stacked 3LG ($\sim$1582 cm^{-1}). Detailed characterization of the 2D mode profile in ABC-stacked and AB-stacked 4–6LG can be found in ref. 5, 150 and 171. However, the differences in the 2D mode profile between AB- and ABC-stacked NLG are ε_L-dependent and become more complicated with increasing N.

Later, Lui *et al.*[169] and Zhang *et al.*[150] demonstrated that the interlayer vibrations such as the C modes can be used to reveal the stacking order of NLG based on their different symmetries. Lui *et al.* observed a noticeable Raman peak at $\sim$33 cm^{-1}, assigned to C_{31} in AB-3LG, whereas a pronounced peak at $\sim$19 cm^{-1}, attributed to C_{32}, was observed in ABC-3LG at a

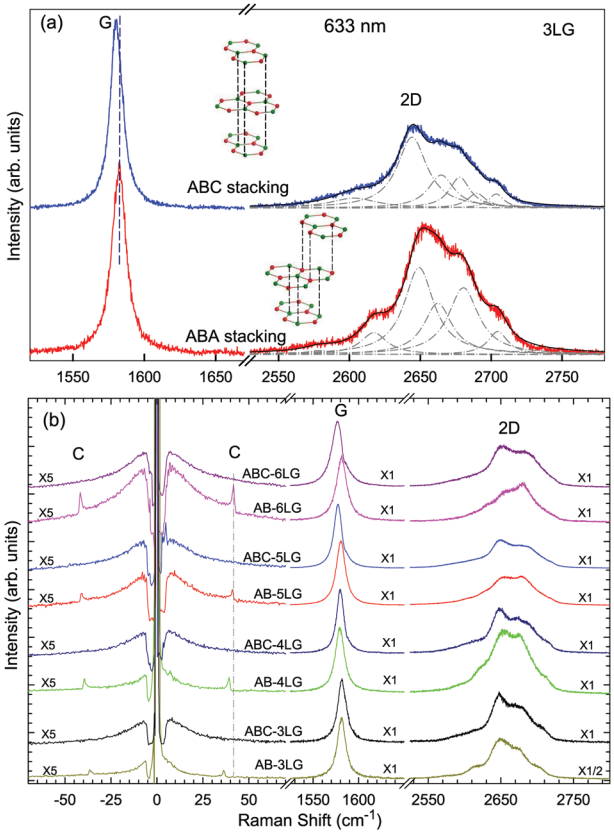

Fig. 9 (a) Raman spectra of 3LG measured in the ABA and ABC zones in the G and 2D mode regions under excitation at 633 nm. A schematic diagram of ABA and ABC structures is shown. The 2D peaks of ABA- and ABC-3LGs are fitted by Lorentzian line shapes (dashed-dotted lines). (b) Raman spectra of 3–6LG with AB and ABC stacking in the C, G, and 2D peak spectral regions. The C modes are observed in AB-*N*LG (*N* = 3, 4, 5, 6) but not in ABC-*N*LG. Reproduced with permission from ref. 150. Copyright 2016, Elsevier.

high temperature (800 K) induced by laser heating when the samples were suspended on a quartz substrate. The vanishing of C_{31} in ABC-3LG is due to its Raman inactivity, whereas the absence of C_{32} in AB-*N*LG is ascribed to the unsuitable polarization configuration.[169] Zhang *et al.* carried out further investigation on the ULF Raman spectra of both AB- and ABC-*N*LG deposited on Si/SiO_2 substrates at room temperature and found that C_{N1} can only be observed in AB-stacked but not ABC-stacked *N*LG, as shown in Fig. 9(b). ABC-*N*LG belongs to the D_{3d} point group where the C modes are represented by $\frac{N-1}{2}E_g + \frac{N-1}{2}E_u$ for ONLG and $\frac{N}{2}E_g + \frac{N-2}{2}E_u$ for ENLG.[150] According to the irreducible representation of C_{N1} in ABC-*N*LG, C_{N1} was assigned to IR-active E_u in ONLG, whereas it was Raman-active E_g in ENLG. Thus, it was concluded that the absence of the C_{N1} mode in ABC-stacked ONLG is due to symmetry limitations, whereas the disappearance in ABC-stacked ENLG is probably due to the small EPC. It is also noted that C_{NN-i} could not be observed on SiO_2 even when the laser power was as high as 10 mW because it merges with the substrate background, unlike the sample on a quartz substrate.[150,169] Thus, this can be utilized as a new method to distinguish AB- and ABC-stacking in *N*LG.

3.5 Raman spectra of twisted multilayer graphene

Besides the AB and ABC stacking configurations, *N*LG can also be formed by assembling *m*LG (AB-*m*LG if $m > 1$) and *n*LG (AB-*n*LG if $n > 1$) flakes together with a twist angle (θ_t) at the twisted interface, which is denoted as *tN*LG or *t*(*m*+*n*)LG. More constituents and twisted interfaces in *tN*LG are also possible. The twist angle in *tN*LG can be determined by the positions of the so-called R and R′ Raman bands.[57,172,173] The R and R′ modes originate from the non-center LO and TO phonons of the constituents, which are folded back to the Γ point by the presence of Moiré superlattices in *t*(*m*+*n*)LG.[57,172,173] In twisted 2LG (*t*2LG or *t*(1+1)LG), novel physical properties arise because of the periodically modulated interactions between the two Dirac electron gases with a large Moiré supercell, as shown in Fig. 10(a).[174–186] *t*2LG has a Dirac-like linear dispersion with a Fermi velocity lower than that of 1LG.[177,181,182,187] In principle, the band structure of *t*(*m*+*n*)LG can be considered as the overlapping of the band structures of the *m*LG and *n*LG constituents after considering the effects of zone folding resulting from the Moiré superlattices. By changing θ_t, it is possible to tune the optical absorption of *tN*LG.[178,183,185,186] Because of the θ_t-dependent energy of van Hove singularities (VHS) in *tN*LG[178,183,185] and different stacking sequences, *tN*LG exhibits rich electronic and optical properties.[57,71,143,144,188]

*tN*LG can be formed by the accidental folding of graphene flakes during the exfoliation process or by the transfer of graphene flakes onto other graphene flakes.[57,144,189] Most MLG flakes grown by CVD also exhibit twisted stacking.[190–192] Fig. 10(b) shows the optical image of the *t*(1+1)LG and *t*(1+3)LG formed by mechanical exfoliation, and their optical contrasts are shown in Fig. 10(c). In comparison to AB-stacked 2LG and 4LG, optical contrasts of both *t*(1+1)LG and *t*(1+3)LG exhibit additional resonant spectral features around 2.0 eV. These features correspond to the energies of VHSs in the joint density of states (JDOSs) of all optically allowed transitions ($JDOS_{OAT}$) in *t*(1+1)LG and *t*(1+3)LG. Once ε_L matches the energies of the VHSs, the C and LB modes are resonantly observed in the Raman spectra.

The twist in *t*(*m*+*n*)LG significantly modifies the symmetry and Raman activity of the C and LB modes with respect to AB-MLG. *t*(*m*+*n*)LG ($m \neq n$) has C_3 symmetry, and the corresponding irreducible representation is $\Gamma_{vib} = A + E$, and both A and E modes are Raman active. In *t*(*m*+*n*)LG with $m \neq n$, all nondegenerate LB modes have A symmetry, and all doubly degenerate C modes have E symmetry. *t*(*n*+*n*)LG ($n \geq 2$) has D_3 symmetry, and the corresponding irreducible representation is $\Gamma_{vib} = A_1 + A_2 + E$. The A_1 and E modes are Raman active, whereas the A_2 mode is Raman inactive. In *t*(2+2)LG, LB_{41}, and LB_{43} have A_1 symmetry, whereas LB_{42} has A_2 symmetry, and all the C modes are E symmetry. The changes of the symmetry and Raman activity and the presence of VHS energies of $JDOS_{OAT}$ in *tN*LGs make the C and LB modes observable when ε_L matches the corresponding VHS energies.

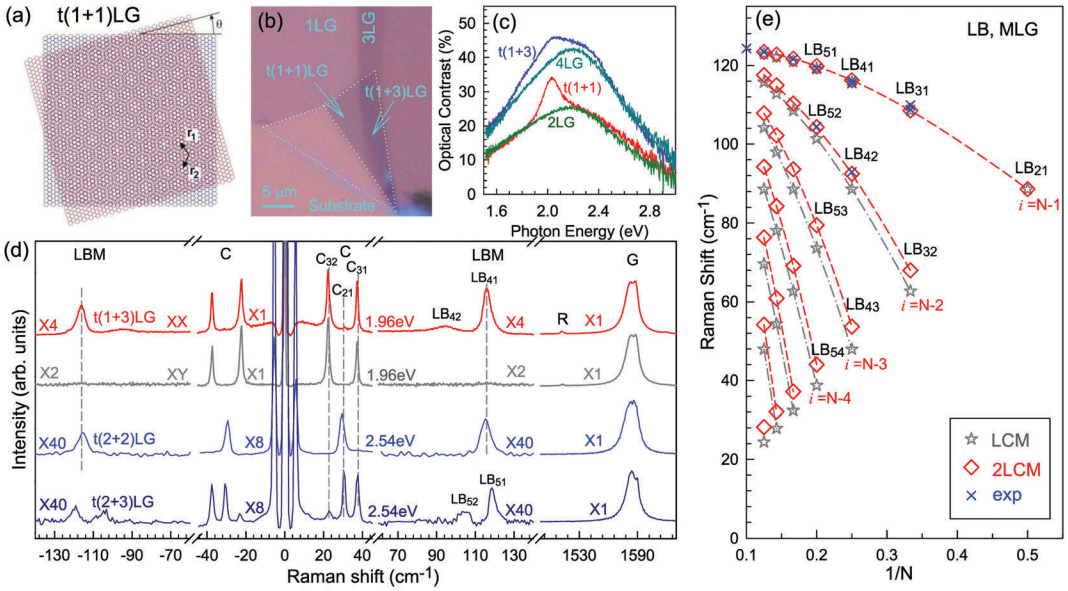

Fig. 10 (a) Moiré pattern of *t*(1+1)LG. (b) Schematic diagram of *t*(1+3)LG. (c) Optical image of a flake comprising a *t*(1+1)LG and a *t*(1+3)LG. Reproduced with permission from ref. 57. Copyright 2014, Nature Publishing Group. (d) Stokes/anti-Stokes Raman spectra in the C and LB spectral range, and Stokes Raman spectra in the G peak region for *t*(1+3)LG, *t*(2+2)LG and *t*(2+3)LG. Polarized Raman spectra of *t*(1+3)LG are also shown. Reproduced with permission from ref. 71. Copyright 2015, American Chemical Society. (e) The theoretical wavenumber of the LB modes as a function of *N* calculated from LCM and 2LCM. The gray dashed-dotted and red dashed lines are eye guides for LCM and 2LCM, respectively. Blue crosses show the experimental (exp) data.

Fig. 10(d) shows the Stokes/anti-Stokes Raman spectra in the C and LB spectral range and the Stokes Raman spectra in the G peak region for *t*(1+3)LG, *t*(2+2)LG and *t*(2+3)LG in the back-scattering configuration. In *t*(1+3)LG, the C modes of 3LG and the LB modes of 4LG are observed. The absence of the LB modes in the cross (XY) polarization configuration confirms the nature of the LB vibrations. This indicates that the twisted interface obstructs the interlayer shear coupling so that only the C modes of the AB-stacked constituents can be measured.[57] The shear coupling at the twisted interface ($\alpha_t^{\parallel}$) is found to be 20% of the bulk case ($\alpha_0^{\parallel}$).[57] However, the twisted interface will not affect the interlayer breathing coupling, so the LB modes of all layers are observed.[71] For the LB modes, based on LCM and experimental $\omega(\mathrm{LB}_{N1})$ in *t*NLGs, the fitted $\alpha_0^{\perp}$ is $\sim 106 \times 10^{18}$ Nm^{-3}, and the silent LB mode (B_{2g}) in graphite is determined to be $\sim$125.3 cm^{-1}, slightly smaller than $\sim$128 cm^{-1} determined by neutron spectrometry. However, the simulated $\omega(\mathrm{LB}_{42})$ and $\omega(\mathrm{LB}_{52})$ based on LCM are 3–4 cm^{-1} lower than those observed in *t*(1+3)LG and *t*(2+3)LG, suggesting that the θ_t-independent second-nearest-neighbor breathing interactions ($\beta_0^{\perp}$) is necessary to fit the experimental values of $\omega(\mathrm{LB}_{42})$ and $\omega(\mathrm{LB}_{52})$. The new model is denoted as 2LCM and $\beta_0^{\perp}$ of $\sim 9.3 \times 10^{18}$ N m^{-3} can be used to fit well the experimental data. Because the relative motions of the second-nearest-neighbor layers are always out-of-phase for the LB_{N2} modes, $\alpha_0^{\perp}$ with additional $\beta_0^{\perp}$ is crucial to reproduce their frequencies, as indicated by Fig. 10(e). However, the second-nearest-neighbor layers are always in-phase for the LB_{N1} modes; thus, $\omega(\mathrm{LB}_{N1})$ is insensitive to $\beta_0^{\perp}$, and it can be well estimated by the LCM.

Because of the softened $\alpha_t^{\parallel}$ and identical $\alpha_0^{\perp}$ to the bulk case at the twist interface in *t*NLGs, $\omega(C)$ is mainly determined by the number of layers of each AB-stacked constituents, whereas ω(LB) is mainly determined by the number of layers (N) of *t*NLGs, as shown in Fig. 10(d) for *t*(1+3)LG, *t*(2+2)LG and *t*(2+3)LG. Therefore, the number of layers of AB-stacked constituents and *t*NLG itself can be identified by the observed ω(C) and ω(LB), respectively, under resonant conditions.

4 Resonance Raman spectroscopy of monolayer and multilayer graphenes

Raman scattering is a process related to photo-excited electron–hole pairs, phonon scattering by electrons or holes, and electron–hole recombination. Thus, the Raman intensities and profiles of Raman modes are determined by the EPC and band structures of the materials. The intensity of the Raman modes of graphene can be calculated by second-order perturbation theory.[80,172] Because of the unique band structure, most of the Raman modes in graphene are involved in resonance processes. As discussed before, the combination modes and first-order Raman modes activated by defects, *e.g.*, 2D, D + D″, and D, originate from the TR or DR process.[56] The intensity of the G mode in 1LG is also dominated by quantum interference effects. In AB-*N*LG, the Fano profile of C modes arises from the quantum interference between the C mode and a continuum of electronic transitions near the *K* point, as shown in Fig. 8(c and d). In *t*NLG, the first-order modes (C, LB and G modes) can be enhanced by the singularities in $\mathrm{JDOS}_{\mathrm{OAT}}$. Because the DR and TR Raman processes in graphene and MLG have been discussed above in detail, we will address the latter three cases of resonance in the following subsections.

4.1 Quantum interference of the G mode in graphene

The peculiar linear band structure of graphene means that the G mode always satisfies the incoming and outgoing resonant conditions, as demonstrated in Fig. 4(a). Besides the two resonant intermediate excited states (pathway I in Fig. 11(a)), there are many nonresonant intermediate excited states (pathway II in Fig. 11(a)), which also contribute to the Raman scattering of the G mode. The Raman intensity of the G mode, I(G), is a result of total quantum interference between different Raman pathways in graphene. For an intrinsic graphene sample with $E_F = 0$, it is not easy to reveal the effects of quantum interference between different Raman pathways because it requires the modification of intermediate excited states with transition energies close to the laser excitation energy E_{ex}. When graphene is doped to E_F, an optical transition can be blocked by hole doping when the initial state has an energy higher than the Fermi level and is not occupied, as shown in Fig. 11(b). In this case, one can modify intermediate excited states with transition energies close to E_{ex}.

Chen *et al.* tuned the hole doping by electrostatic doping[58] in an ion-gel-gated graphene device on a SiO_2 substrate, as illustrated in Fig. 11(c). They found that, when near-infrared laser excitation (E_{ex} = 1.58 eV) is used and some of the pathways are blocked, I(G) does not diminish as expected but increases dramatically,[58] as depicted in Fig. 11(d). The observation cannot be interpreted well by the general assumption that the pathway for G mode Raman scattering is due to resonance alone (I in Fig. 11(a)).

To further understand the phenomenon, the pathways close to resonance (II in Fig. 11(a) and off-resonance are expanded. Under these conditions, all pathways interfering with each other have different quantum mechanical amplitudes, including phase and magnitude. For any specific one-phonon and one-photon state, I(G) can be described by

$$I(\mathrm{G}) = \left|\sum_k C_k R_k\right|^2$$
$$R_k = \frac{1}{(E_{ex} - E_k - i\gamma)(E_{ex} - \hbar\omega(\mathrm{G}) - E_k - i\gamma)}, \quad (7)$$

where C_k and R_k are the matrix element and resonance factor, respectively, for a Raman pathway through a vertical electronic transition at wave vector k. E_k is the transition energy, and γ is the energy broadening of the excited state. Fig. 11(e) plots the phase of quantum pathways, $\Phi = \arg(R_k)$, through different intermediate electronic transitions for ε_L = 1.58 eV. Phase differences between different pathways arise mainly from the resonance factor, R_k. In particular, pathways with transition energies E_k above and below energy E_{ex}–$\hbar\omega$(G)/2 have an average phase difference of π, and they interfere destructively if all quantum pathways are allowed, leading to an overall weak Raman signal. Blocking pathways below E_{ex}–$\hbar\omega$(G)/2, thus, leads to a large enhancement of G-mode Raman scattering. When $2E_F$ is increased further, more in-phase pathways are blocked and the Raman intensity starts to decrease.

The above results show that the simple picture of G-mode graphene Raman scattering, in which only the on-resonance pathways are considered, is invalid. This unexpected phenomenon presents evidence for a new understanding of resonance Raman scattering in graphene.

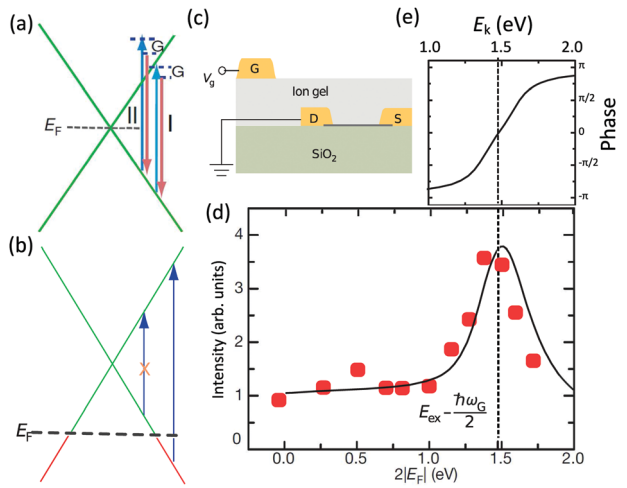

Fig. 11 (a) Illustration of two representative G-mode Raman pathways (I and II) through two different intermediate excited states in graphene with $E_F = 0$. (b) Hole doping results in electronic transitions from zero energy to $2|E_F|$ being blocked because of empty initial states. (c) An ion-gel-gated graphene device on a SiO_2 substrate can make graphene p-doped. (d) I(G) as a function of $2|E_F|$ (symbols). Black line: theoretical prediction. (e) Quantum phase of Raman pathway amplitude illustrated as a function of intermediate excitation energy. Reproduced with permission from ref. 58. Copyright 2011, Nature Publishing Group.

4.2 Fano resonance in multilayer graphenes

A Raman peak usually exhibits a symmetric Lorentzian line shape, such as the G peak in 3LG and graphite, as shown in Fig. 12(a). However, the C modes in AB-*N*LG and graphite show Fano line shapes, as shown in Fig. 12(b) for 3LG and graphite. The Fano resonance effect describes a quantum interference effect between a discrete state (in this case phonon states) and a continuum transition, in which the excited eigenstates are a mixture of the discrete and continuum states.[193] Historically, the Fano line shape was observed in heavily doped silicon systems,[194] metallic carbon nanotubes,[195] nanowires,[196] and topological insulators.[197] The Fano resonance is highly asymmetric, in which the asymmetry of the line shape depends on the coupling coefficient between discrete and continuum states. The Fano lineshape can be expressed by[70,198]

$$I(\omega) = I_0 \frac{[1 + 2(\omega - \omega_0)/(q\Gamma)]^2}{1 + 4(\omega - \omega_0)^2/\Gamma^2} \quad (8)$$

where I_0, ω_0, Γ, and $1/|q|$ are the intensity, uncoupled mode frequency, broadening parameters, and the coupling coefficient, respectively. The peak maximum is at $\omega_{max} = \omega_0 + \Gamma/2q$, whereas the full-width at half-maximum (FWHM) is $\Gamma(q^2 + 1)/|q^2 - 1|$. Both are related to the coupling coefficient, $1/|q|$. The Lorentzian line shape recovers from the Fano shape in the limit of $1/|q| \to 0$. The laser-induced electron–hole plasma and the multiphonon

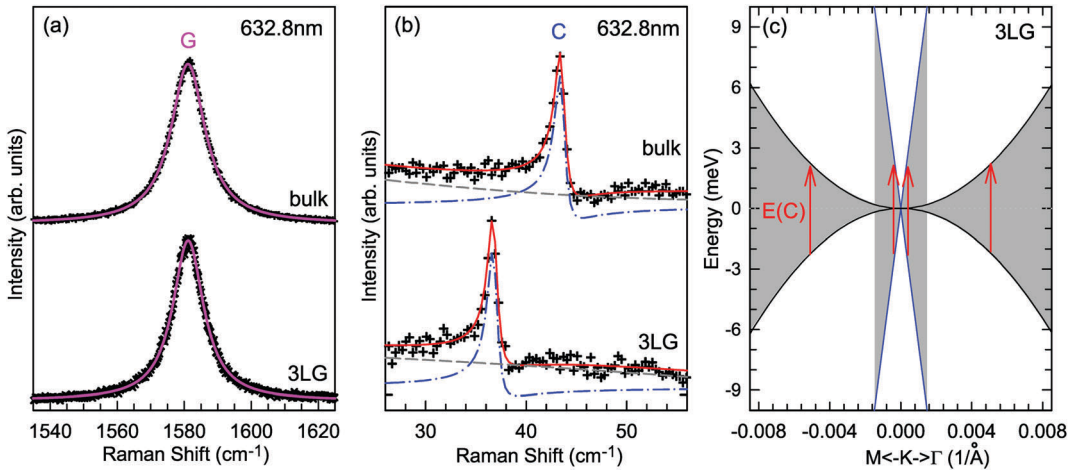

Fig. 12 (a) Lorentzian line shape of the G peak in 3LG and bulk graphite. (b) The C peak of 3LG and bulk graphite fitted by a Breit–Wigner–Fano line shape. The solid red lines, dashed lines, and dashed-dotted lines are the fitted curves, background, and Fano components, respectively. Spectra in (a and b) were excited at 1.96 eV. (c) Schematic band structure of 3LG close to *K*. The gray regions highlight transitions near *K* that could resonate with the C mode. Red arrows indicate transitions with the same energy as the C mode, *E*(C). Reproduced with permission from ref. 70. Copyright 2012, Nature Publishing Group.

resonance can be excluded as reasons for the Fano line shape because $\hbar\omega$(G) remains constant and the C peak at 77 K has the same $1/|q|$ as at room temperature.[70] The Fano line shape for the C mode, thus, is ascribed to the quantum interference between the C mode and a continuum of electronic transitions near the *K* point.[70] Taking AB-3LG as an example (see Fig. 12(c)), in the range of the C peak energy (E(C) $\sim$ 5 meV), the C phonons couple well with the active electronic transitions, resulting in quantum interference. Many factors, such as charge transfer from the substrate or an intercalation agent[58,59,61,115] and the adsorption of air molecules,[59] have significant effects on the increase in the Fermi level (especially for $E > E$(C)/2), thus reducing the coupling coefficient. As the graphene flakes become thinner, this effect becomes more significant. Therefore, the coupling coefficient in *N*LG decreases with decreasing *N*.

In principle, the G mode in graphene and *N*LG should also exhibit the Fano line shape. Indeed, the G band of 1LG exhibits an asymmetric line shape near the charge neutrality point as a manifestation of Fano resonance, whereas the line shape is symmetric when the graphene sample is electron or hole doped.[199] The observed Fano resonance can be interpreted as an interference between the phonon and excitonic many-body spectra in graphene.[199] However, the line shape of the G mode in neutral 1LG shows only a very slight asymmetry because of the small $1/|q|$, $\sim$0.07, which is much smaller than that of the C modes ($\sim$0.3[70]), leading to an almost imperceptibly asymmetric peak. The G band of AB-2LG does not exhibit any Fano resonance, regardless of doping.[199] The Fano resonance can also be observed in the infrared spectra of phonons in *N*LG because of the strong coupling between phonons and interband electronic transitions.[200,201]

4.3 Resonant Raman spectroscopy of twisted multilayer graphene

In comparison to AB-*N*LG, the band structures of *tN*LG are significantly affected by the presence of a twisted interface and Moiré pattern, introducing several θ_t-dependent VHSs to the density of states (DOSs).[57,71,182,185,186] The relationship between the energies of the VHSs of parallel bands near *K* and θ_t can be estimated,[186] $E_{\mathrm{VHs}} \approx 4\pi\theta_t\hbar\nu_{\mathrm{f}}/\sqrt{3}a$, where a is the lattice constant of graphene (2.46 Å), $\hbar$ is the reduced Planck's constant, and ν_{f} is the Fermi velocity of 1LG ($\sim 10^6$ m s^{-1}). For a fixed laser excitation energy ε_{L}, the Raman signal of t(1+1)LG is enhanced around a specific θ_t when ε_{L} matches the VHS energy of the corresponding t(1+1)LG.[185,186] Similar results had been observed in $t(m+n)$LG.[202]

To probe the intrinsic resonant Raman behavior of $t(m+n)$LG, it is necessary to study a $t(m+n)$LG with specific θ_t using tunable excitation energies. Indeed, as shown in Fig. 13(a), I(G) of a t(1+1)LG can be enhanced by a factor of more than 30 at a specific ε_{L}. In the quantum mechanical picture of Raman scattering, incident photons first excite a set of intermediate electronic states, which are then scattered by phonons and radiate energy-shifted photons. However, only the optically allowed electronic transitions are involved in the resonant Raman process. Therefore, the VHS energies of JDOS$_{\mathrm{OAT}}$ should be considered for Raman resonance in $t(m+n)$LG. JDOS$_{\mathrm{OAT}}$ can be calculated using the following equation:[57]

$$\mathrm{JDOS}_{\mathrm{OAT}}(E) \propto \sum_{ij}\sum_{k}\left|M_{ij}(\vec{k})\right|^2\delta\left(E_{ij}(\vec{k}) - E\right) \qquad (9)$$

where $M_{ij}(\vec{k})$ is the optical matrix element between the ith conduction and jth valence bands, and $E_{ij}(\vec{k})$ gives the transition energy of a $i \rightarrow j$ band pair at the wave vector $\vec{k}$. The band structure of t(1+1)LG with 10.6° ($(p,q) = (1,9)$) is calculated and shown in Fig. 13(b), and the optically allowed transitions are marked by dashed arrows. The squared optical matrix elements of the corresponding transitions are shown in Fig. 13(c). Indeed, the transitions with energy $\sim$1.15 eV between parallel bands along *K*–*M* are forbidden, as indicated by solid arrows with crosses. The JDOS$_{\mathrm{OAT}}$ of t(1+1)LG is shown in Fig. 13(d). There is one distinctive VHS in the JDOS$_{\mathrm{OAT}}$ of t(1+1)LG, which is

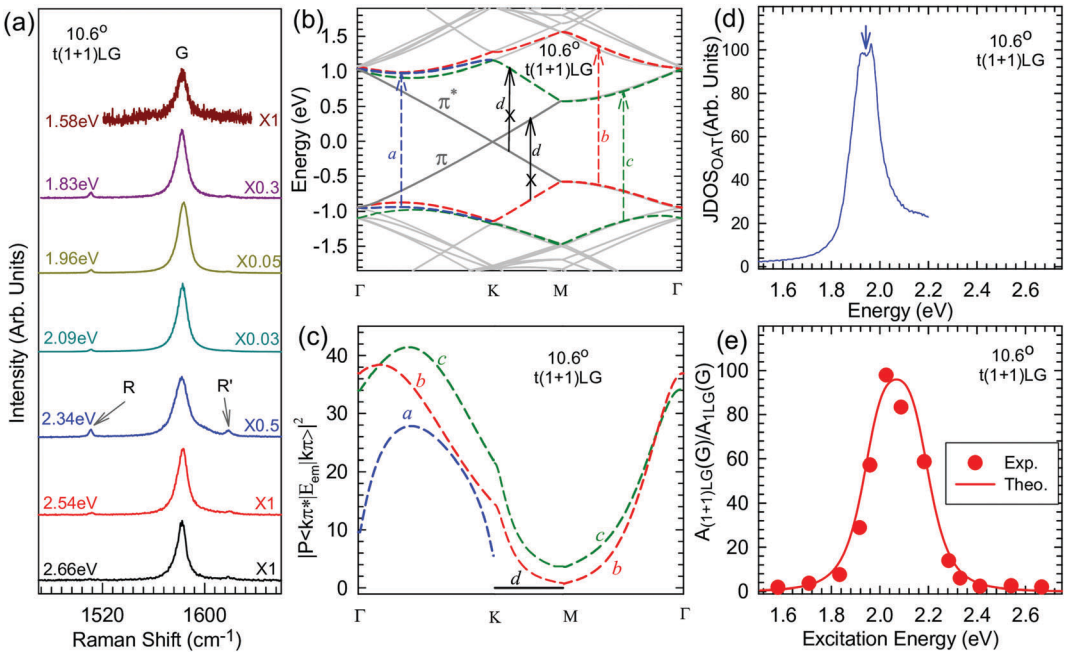

Fig. 13 (a) G mode of t(1+1)LG excited by seven ε_L. The R and R′ modes are indicated by arrows. The spectra are scaled and offset for clarity. (b) The band structure of (1,9) t(1+1)LG. The optically allowed transitions are marked by dashed arrows. The transitions between parallel bands along the K–M direction are forbidden, as indicated by the solid arrows with crosses. (c) Squared optical matrix elements of the corresponding band pairs in (b). (d) $JDOS_{OAT}$ in t(1+1)LG along Γ–K–M–Γ. (e) A(G) of t(1+1)LG as a function of ε_L. Filled circles: experimental data. Solid lines: simulations. Reproduced with permission from ref. 57. Copyright 2014, Nature Publishing Group.

labeled by an arrow. When ε_L matches the VHS energies of $JDOS_{OAT}$ of the t(1+1)LG, the Raman resonance of the G mode occurs. The experimental ε_L-dependent peak area of the G mode (A(G)) in t(1+1)LG can be well fitted using the calculated VHS energy of 1.95 eV.

The DR process in t(1+1)LG is more complicated than that in 1LG because of the zone-folding effect of the band structures. Similar to 1LG, the 2D peak of t(1+1)LG usually shows a single Lorentzian peak; however, the FWHM and frequency of the 2D peak in t(1+1)LG also depend on θ_t.[186,203,204]

The resonance Raman behavior of $t(m+n)$LG ($m > 1, n > 1$) becomes complicated because of its novel band structures and EPC. Because there may exist multiple VHS energies of $JDOS_{OAT}$ in $t(m+n)$LG, the resonant profiles of A(C), A(LB), and A(G) are usually composed of several subpeaks corresponding to each VHS energy.[57] The strong resonance Raman effect makes the C and LB modes observable in $t(m+n)$LG, paving the way to probe interface coupling and stacking orders of tNLG, especially for CVD-grown tNLG.[57,71,144,202,205]

5 Disordered monolayer and multilayer graphenes

One generally refers to defects in graphene as anything that breaks the symmetry of the infinite carbon honeycomb lattice.[206] The amount and nature of the defects strongly depend on the production method and may change from sample to sample. Both the amount and the nature of defects can have a strong influence on the properties of graphene samples.[208] For example, atomic-sized defects can introduce midgap states close to the Dirac point and have been identified as the major limiter of electron mobility for graphene deposited on substrates.[209,210] Extended line defects could be used to guide charge, as well as spin, atoms, and molecules.[211,212] Defects also have a strong influence on chemical reactivity, which makes defective graphene a prospective catalyst.[213] It is crucial to understand how the defects in graphene affect its Raman spectrum and how to use Raman spectroscopy to identify these defects.

5.1 Raman spectra of defect-containing graphene flakes

It is well-known that, with respect to pristine graphite and graphene, additional Raman modes can be observed in disordered graphite and graphene, *e.g.*, the so-called D and D′ modes. These modes cannot be attributed to the vibration mode from defects themselves, but correspond to phonons with momentum $\mathbf{q} \neq 0$ because of the presence of defects in the sample. This defect induced process is not allowed in a purely crystalline sample (without defects) because of momentum conservation. The intensity, peak position, and linewidth of the Raman modes in pristine graphite and graphene can significantly change with the increasing number of defects.

Fig. 14(a) shows an example of the Raman spectra of 1LG samples subjected to different ion implantation conditions.[15] By increasing the ion dose, I(D) increases from the zero value of pristine 1LG. Above 10^{13} Ar^+ per cm^2 the Raman peaks start to broaden significantly. Above 10^{15} Ar^+ per cm^2 the spectra show a decreased intensity, indicating the full amorphization or

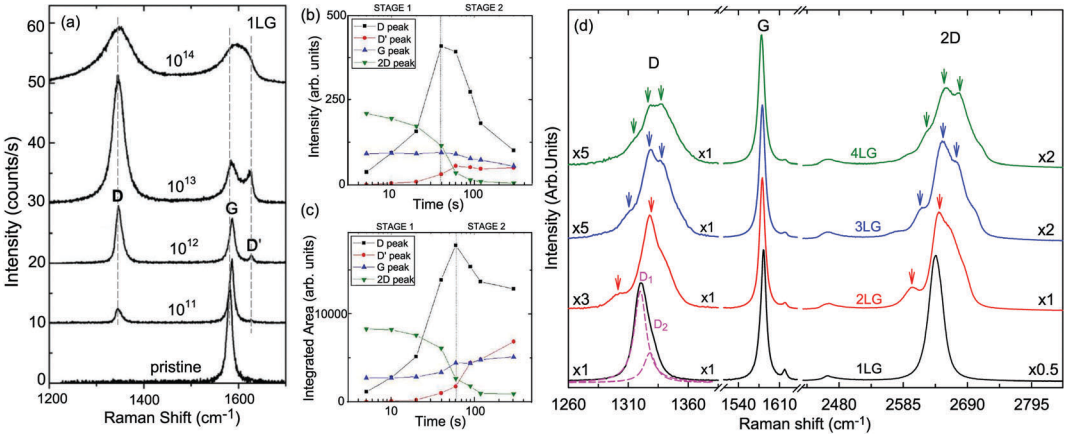

Fig. 14 (a) Evolution of the D, G, and D′ modes of 1LG samples implanted by different ion doses in units of Ar^+ per cm^2. Reproduced with permission from ref. 15. Copyright 2010, Elsevier. Raman intensity as (b) amplitude and (c) integrated area of oxidized graphene under increasing plasma exposure. Reproduced with permission from ref. 206. Copyright 2012, American Chemical Society. (d) Raman spectra of *n*LG (*n* = 1, 2, 3 and 4) implanted with 90 keV carbon (^{12}C) ions at a fluence of 5 × 10^{13} C^+ per cm^2 by an LC-4 type system. Reproduced with permission from ref. 207. Copyright 2015, Elsevier.

partial sputtering of the graphene layer.[15] Fig. 14(b and c) show the peak intensity and peak area (integrated intensity) of the D, G, D′, and 2D modes in oxidized graphenes with increasing plasma exposure.[206] Note that the units are arbitrary, that is, we can compare the trend of the different peaks with exposure time, but we cannot compare the absolute numbers for a fixed time. The number of defects increases with increasing plasma exposure time. I(D) and I(D′) show similar trends to that of Ar^+-implanted 1LG, as shown in Fig. 14(a). The evolution of I(D) with respect to the number of defects can be divided into two stages. In stage 1, the low defect stage, I(D) increases with respect to the number of defects. In stage 2, as the number of defects further increases, I(D) decreases, as shown in Fig. 14(b and c). Interestingly, I(2D) decreases sharply in stage 2. Because the 2D mode can be easily observed only when the crystallinity of graphene is high (pristine or with a few defects), it can be employed as an indicator of relatively high-quality graphene. I(G) in Fig. 14(b) slightly decreases with increasing plasma exposure time, and A(G) shows the opposite behavior because of the width broadening. I(G) and A(G) at low defect concentrations are insensitive to the number of defects because they arise from the in-plane C–C bond stretching of all pairs of sp^2 atoms in both rings and chains.[214] This makes I(G) or A(G) an intensity reference for the defect-induced Raman modes in defect-containing graphene flakes, as discussed later.

The Raman intensity of the defect-induced modes (*e.g.*, D and D′) is proportional to the average number of defects in the unit cell, n_d, at a low defect concentration. Based on the double resonance theory,[215] the intensity of a Raman mode in graphene is closely related to the finite lifetime (τ) of the electronic states involved in the Raman process, which corresponds to a line broadening energy $\gamma = \hbar/\tau$ because the electronic states interact, *e.g.*, with phonons and defects. The total broadening energies (γ^{tot}) should consider the sum of the broadening of the corresponding electronic states. γ^{tot} can be considered as the sum of two contributions, γ^{ep} and γ^{D}, where γ^{ep} is the intrinsic broadening (present in perfectly crystalline samples) arising from electron–phonon scattering and γ^{D} is extrinsic (induced by the presence of defects and dependent on the sample quality), arising from electron-defect elastic scattering. For a simplified case, γ^{tot} depends only on the excitation energy, ε_L, of the type of defect and its concentration, n_d, through $\gamma^{tot} = \gamma^{ep}(\varepsilon_L) + \gamma^{D}(\varepsilon_L, n_d)$. The D mode depends on n_d through two distinct mechanisms. First, it is proportional to n_d ($I(D) \propto n_d$). Secondly, it depends on n_d through electron/hole broadening energies ($\gamma^{tot} = \gamma^{ep} + \gamma^{D}$). With increasing n_d, γ^{D} increases, thus leading to a decrease in the intensity of the resonant phonon modes. At low defect concentrations ($\gamma^{tot} \gg \gamma^{D}$), the first mechanism is dominant and, thus, I(D) increases as n_d increases. With further increasing n_d, the second mechanism becomes dominant, leading to a decrease in I(D). However, I(2D) is sensitive to γ^{tot} and the electronic structure of the defect-containing graphene. Therefore, I(2D) decreases with γ^{tot} broadening when the band structure changes slightly.[215] The process can also be divided into two steps: (1) $\gamma^{ep} \gg \gamma^{D}$ and $\gamma^{tot} \sim \gamma^{ep}$, where I(2D) remains constant, and (2) $\gamma^{D} \gg \gamma^{ep}$ and $\gamma^{tot} \sim \gamma^{D}$, where I(2D) reduces continuously. Thus, the decreasing slope of I(2D) depends on how heavily the various types of defects influence the graphene, in particular, the band structure. Some special laser lines should be chosen to enhance the 2D band when the bandgap is open to the visible and even ultraviolet range, similar to that in carbon nanotubes.[216,217] Furthermore, for defect-containing graphene in stage 2, I(2D) gradually becomes weaker. I(2D) can even become invisible for heavily disordered graphene. In this case, the graphene sheet starts to be dominated by the fully-disordered areas. The above analysis can be extended to different types of defects, allowing the characterization of the defects in graphene.

Raman spectra of ion-implanted MLGs show similar spectral features to that of 1LG, as discussed above.[207,218] As depicted in Fig. 14(d), the D band of ion-implanted 1LG exhibits an asymmetrical lineshape and can be fitted by two Lorentzian subpeaks, *i.e.*, the D_1 and D_2 peaks, which result from two DR Raman processes, as demonstrated in Fig. 4(f and g), respectively. $I(D_1) = 3I(D_2)$.

If we assume that one of the two D subpeaks corresponding to each 2D component in the MLGs is dominant, as in 1LG, the D band profiles should be very similar to the corresponding 2D band. Indeed, similar profiles of the D and 2D bands have been observed for ion-implanted *N*LG, as indicated by the arrows in Fig. 14(b). When *N*LGs are implanted by the same ion dose, I(D) becomes weaker with increasing N because the average number of defects in ion-implanted *N*LG decreases with increasing N.

5.2 A general model for point defects and line defects

Point and line defects are two typical sets of defects in graphene, whose schematic diagrams are shown in Fig. 15(a and b), respectively. Point defects are characterized by the average distance between nearest defects (L_D) or by the defect density ($\sigma = 1/L_D^2$). The typical point defects in graphene and MLG can be introduced by ion implantation or ion-bombardment.[15,16,66,207] These techniques have been used for other two-dimensional materials to create point defects.[220–222] Line defects are characterized by their average crystallite size (L_a) or by the crystallite area (L_a^2). A highly crystalline turbostratic graphitic structure from amorphous carbon under a high heat treatment temperature is formed by graphene layers with line defects.[223,224] Most graphene samples are likely to exhibit both types of defects, as illustrated in Fig. 15(c). Raman spectroscopy is an ideal tool to identify the number of defects.[15,77,219] Thus, we will address a phenomenological theory to identify the concentrations of point and line defects using I(D)/I(G) or A(D)/A(G) in the following paragraphs.

Because of the quantum confinement effect, the FWHM of the G peak (Γ_G) increases with increasing defect density. Fig. 15(d) shows Γ_G as a function of L_a or L_D. Γ_G increases exponentially as the phonon localization length ξ decreases with respect to the phonon coherence length l_{ph}, as proposed by Ribeiro-Soares *et al.*:[224]

$$\Gamma_G(L_a,L_D) = 15 + 87 \exp(-\xi/l_{ph}). \quad (10)$$

For samples containing only line defects, $\xi = L_a$ (because phonons are confined within a crystallite size of L_a). For samples with pure point defects, $\xi = \alpha L_D$, where $\alpha = 10$. Point defects are less effective in localizing phonons compared to line defects; therefore, $\alpha > 1$. The experimental data are in good agreement with theory (solid and dashed lines, respectively), as shown in Fig. 15(d).

The other protocol is based on the intensity ratio between the disorder-induced D band and the G band, *i.e.*, I(D)/I(G). To avoid the influence of peak broadening and the wavelength dependence of the peak intensity, the integrated intensity (peak area) ratio, $(A_D/A_G)E_L^4$, is considered here. $(A_D/A_G)E_L^4$ as a function of L_a and L_D is shown in Fig. 15(e). There are two stages for the evolution of $(A_D/A_G)E_L^4$ with increasing defect density.

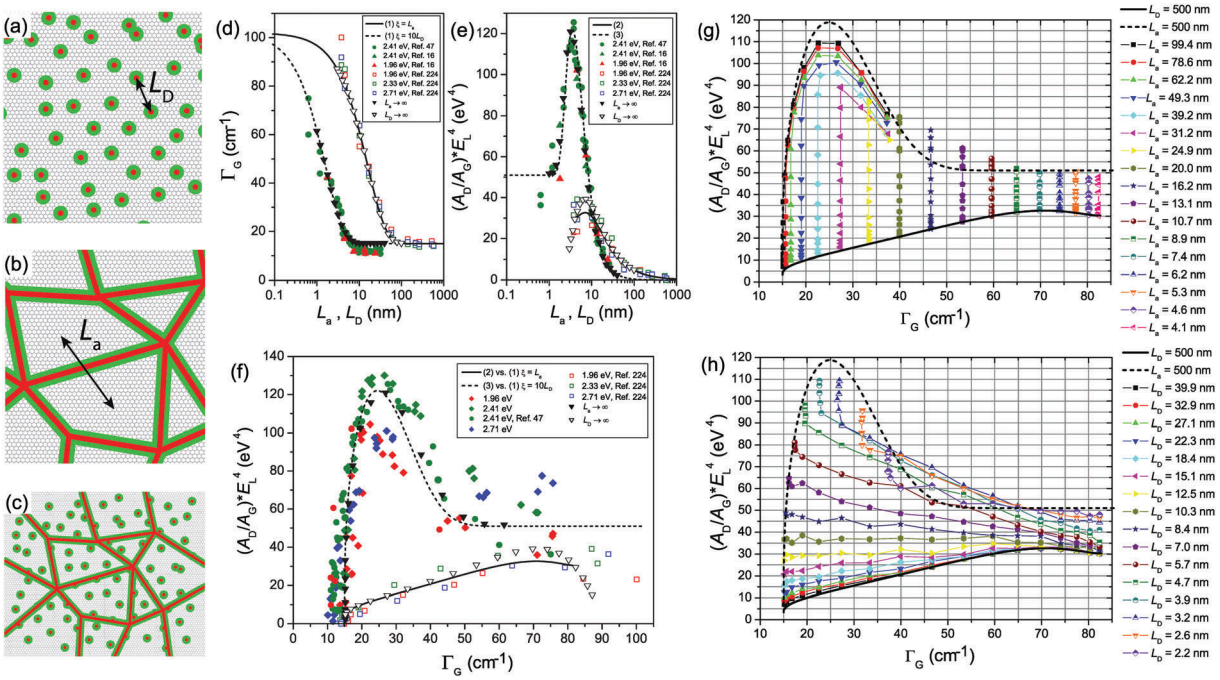

Fig. 15 Illustrations of graphene samples with point defects (a) and line defects (b). (c) Illustrations of a graphene sample containing both point and line defects. The red regions in (a–c) define the structurally damaged area (S-region), and the green circles and lines in (a–c) are the activated area (A-regions) where the D band is active. (d) Γ_G as a function of L_a or L_D. The solid and dashed lines are the plots of eqn (10) as a function of L_a ($\xi = L_a$) and L_D ($\xi = 10L_D$), respectively. (e) $(A_D/A_G)E_L^4$ as a function of L_a or L_D. The solid and dashed lines are the plots of eqn (11) and (12) as a function of L_a and L_D, respectively. (f) $(A_D/A_G)E_L^4$ as a function of Γ_G. The solid and dashed lines are obtained by simultaneously solving eqn (10) *vs.* eqn (11) and eqn (10) *vs.* eqn (12), respectively. (g and h) Theoretical calculation for $(A_D/A_G)E_L^4$ as a function of the G band spectral linewidth Γ_G. The symbols were obtained from numerical simulations. In (g), equal symbols connected by lines represent samples with a given L_a value (indicated in the legend), with decreasing L_D distances from smaller to larger Γ_G values. (h) The opposite: equal symbols connected by lines represent samples with a given L_D value (indicated in the legend) with decreasing L_a distances from smaller to larger Γ_G values. Reproduced with permission from ref. 219. Copyright 2017, IOP Publishing.

In the low defect density stage, $(A_D/A_G)E_L^4$ increases, because the intensity of the D peak increases with increasing number of defects. At a high defect density stage, $(A_D/A_G)E_L^4$ decreases because the disordered lattice structure reduces A_D. The evolution of A_D/A_G can be understood quantitatively using a phenomenological model.[15] For point defects, a single point defect on the graphene sheet causes modifications on two length scales, here denoted as r_A and r_S (with $r_A > r_S$), which are the radii of two circular areas measured from the impact point. Within the shorter radius r_S, structural disorder from the impact occurs, labeled as the structurally damaged region (S-region) and marked in green in Fig. 15(a and c). For distances larger than r_S but shorter than r_A, the lattice structure is preserved, but the proximity to a defect causes a breaking of selection rules, and leads to an enhancement of the D band, labeled as the activated region (A-region) and marked by red in Fig. 15(a and c). Similarly, the S-region and A-region of line defects are shown in Fig. 15(b and c). Thus, the emergence of the D mode requires both A- and S-regions. $(A_D/A_G)E_L^4$ is dominated by the competition between the S- and A-regions. At a low defect density, there is no competition between the S-region and A-region, leading to an increase in $(A_D/A_G)E_L^4$. At a high defect density, the A-region is occupied by the S-region, leading to a decrease in $(A_D/A_G)E_L^4$. Based on this phenomenological model, $(A_D/A_G)E_L^4$ as a function of L_a or L_D can be given by solving the approximate rate equations for the evolution of S- and A-regions:

$$\frac{A(\mathrm{D})}{A(\mathrm{G})}E_L^4(L_a) = \frac{1}{L_a^2}\left[467.36L_a - 1384.6 - 224.96(L_a - 4)\exp\left(\frac{4 - L_a}{4.1}\right)\right], \quad (11)$$

and

$$\frac{A(\mathrm{D})}{A(\mathrm{G})}E_L^4(L_D) = 51 - \frac{51}{\exp(15.2/L_D^2)} + \frac{4298.6}{L_D^2\exp(15.2/L_D^2)}. \quad (12)$$

As shown in Fig. 15(d and e), the defect-density-dependent behavior of Γ_G is different between the point and line defects. This is also true for $(A_D/A_G)E_L^4$. Thus, by combining the experimental Γ_G and $(A_D/A_G)E_L^4$, the defect types can be identified, as shown in Fig. 15(f).

For the situation where the line and point defects coexist, $(A_D/A_G)E_L^4$ as a function of L_a and L_D can also be given by solving the approximate rate equations for the evolution of the S- and A-regions:

$$\frac{A(\mathrm{D})}{A(\mathrm{G})}E_L^4(L_a, L_D) = 51 - \frac{51}{\exp(15.2/L_D^2)} + \frac{4300.8(L_a - 4)^2}{L_a^2L_D^2\exp(15.2/L_D^2)} + \frac{491.68L_a - 249.28(L_a - 4)\exp\left(\frac{4 - L_a}{4.1}\right) - 1481.92}{L_a^2\exp(15.2/L_D^2)}. \quad (13)$$

Fig. 15(g and h) show the theoretical calculation of $(A_D/A_G)E_L^4$ as a function of the G band spectral linewidth, Γ_G, for the coexistence of point and line defects. Because both crystallite size and point defects contribute to phonon localization, the localization length ξ is chosen as the minimum value between L_a and αL_D for the calculation of Γ_G. The plots in Fig. 15(g and h) provide a user-friendly diagram for the quantification of defects by varying L_a and L_D, respectively. The dashed lines in Fig. 15(g and h) are the same plot of Γ_G-dependent $(A_D/A_G)E_L^4$ obtained from eqn (13) and (10) by varying L_D and considering a fixed value of L_a = 500 nm ($L_a \rightarrow \infty$, which reproduces pure point defects). Similarly, the solid lines in Fig. 15(g and h) correlate the Γ_G-dependent $(A_D/A_G)E_L^4$ obtained from eqn (13) and (10) for different L_a with L_D fixed at 500 nm ($L_D \rightarrow \infty$, which reproduces pure line defects). These two curves delimit a phase space that embraces samples with point and line defects. One can obtain the density of line and point defects by locating the positions in Fig. 15(g and h) according to the experimental $(A_D/A_G)E_L^4$ and Γ_G.

Fig. 15(g and h) and the related equations contain clear specifications for the quantification of defects, establishing a protocol for disentangling the contributions of point-like and line-like defects in the Raman spectra of graphene-based materials. L_a and L_D are important structural parameters to identify the transition between perfect graphene and amorphous carbon. The evaluation of the values from Fig. 15(g and h) is useful for understanding and optimizing the synthetic, purification, and functionalization processes of graphene-based materials, such as graphitic nanocarbon made for inks[225] and conductive coatings.[226]

5.3 Edges

Edges naturally exist in graphene samples and also appear when graphene layers are etched into nanoribbons and quantum dots.[227,228] The properties of graphene strongly depend on the edge orientation in different crystallographic directions.[229–231] Edge is a special kind of defect because the translational symmetry is broken here. An immediate consequence of symmetry breaking is the Raman activation of the defect-related modes, such as the D and D′ modes. The edges of 1LG have two basic orientation configurations, *i.e.*, armchair edge and zigzag edge, whose wave vectors involved in the elastic scattering event of the DR Raman process are $\mathbf{n}_A$ and $\mathbf{n}_Z$, respectively, as demonstrated in Fig. 16(a). Electrons or holes in the DR Raman process cannot be scattered between the K and K' valleys by $\mathbf{n}_Z$. Therefore, a perfect zigzag edge cannot produce a D peak.[56,77,232] This does not apply to an intervalley scattering mode (*i.e.*, D′), which can be activated both by armchair and zigzag edges.[56] Because the atomic structures of perfect zigzag and armchair edges in a graphene layer are only constructed from the two outermost atoms at the edge, the edge of the graphene layer is quite different from line defects, as discussed in Section 5.2.

To understand the Raman spectrum at graphene edges, the Raman process in real space should be considered. In real space, phonons, defects, electrons, and holes can be viewed as quasi-particles. A complete Raman process is limited by the

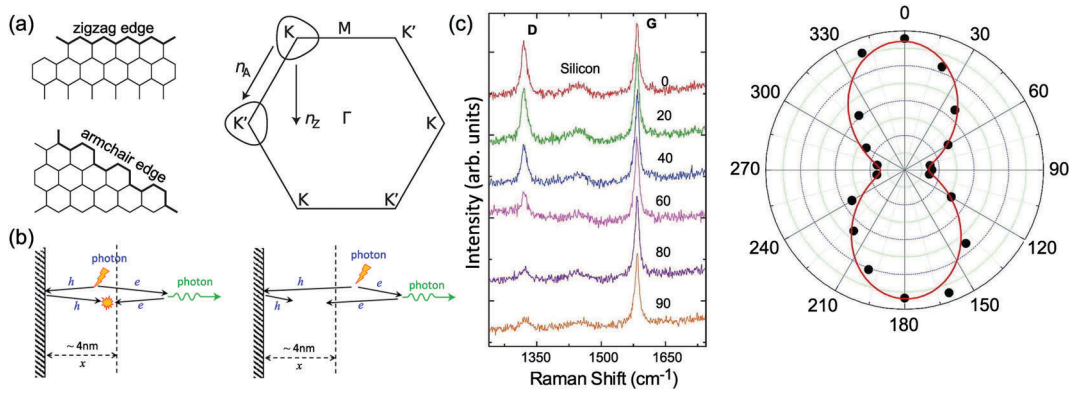

Fig. 16 (a) Left panel: Ideal zigzag and armchair edges. Right panel: Equi-energy contours for electronic states involved in the D peak. n_Z and n_A indicate directions normal to the zigzag and armchair edges, respectively. (b) Real-space Raman processes take place at a given point in space. Photon-excited electrons (*e*) and holes (*h*) move along classical trajectories. After emitting phonons or scattering at edges, the D mode is activated (left panel) when *e* and *h* must meet with opposite momenta at the same point in space to recombine radiatively and produce the scattered photon. Otherwise, the D mode cannot be activated (right panel). The length scale (*x*) in the vicinity of an edge contributing to the D mode is determined by the traveling distance (~4 nm) of *e* and *h* over the lifetime of the virtual electron–hole pair. Reproduced with permission from ref. 56. Copyright 2013, Nature Publishing Group. (c) Raman spectra at a graphene edge measured for different incident polarization measured at 633 nm (left panel), and *I*(D)/*I*(G) as a function of laser polarization direction (right panel). Reproduced with permission from ref. 77. Copyright 2009, American Chemical Society.

momenta (spatial extent and direction) of electrons and holes. Therefore, first, a perfect armchair edge requires that the electronic momentum is perpendicular to the edge so that electron and hole can meet and recombine radiatively to activate the D mode. Moreover, the spatial extent of electron and hole involved in the DR Raman process to meet and recombine radiatively is estimated to be ~4 nm,[77] which means that only the zone ~4 nm from the edge contributes to the D mode, as shown in Fig. 16(b).[56] The D mode at perfect armchair edges shows polarization dependence because of the requirements of the DR Raman process. When the polarization of the incident laser is along the *K*–*M* direction, the D mode presents the strongest intensity. For a linearly polarized light oriented at an angle θ with respect to the perfect armchair edge, the θ-dependent *I*(D) is: $I(\mathrm{D}) \propto \cos^2(\theta)$,[77] as shown in Fig. 16(c). For the D′ peak, its real-space Raman process is analogous to that of the D peak. For both zigzag and armchair edges, this leads to the same $I(\mathrm{D}') \propto \cos^2(\theta)$ dependence.[56,75–77,232] For ideal edges, the D peak is zero for zigzag orientations and large for armchair orientations. However, for real samples, *I*(D)/*I*(G) does not always show a significant dependence on the edge orientation. For exfoliated samples, even though edges can appear macroscopically smooth and oriented at well-defined angles, they are not necessarily microscopically ordered.[77] In this case, the polarization dependence for a disordered edge is determined by contributions from armchair and zigzag segments with different orientations.

In the case of MLG edges, each graphene layer in MLG will contribute its own edge to the overall edges. Ideal MLG edges should exhibit good alignment of all the edges of the graphene layers, as shown in Fig. 17(a and b) for 2LG and 3LG cases, respectively. In reality, each graphene layer in MLG is misaligned with adjacent layers to a significant extent, from micrometers (see Fig. 17(c)) to nearly zero. This is also true of CVD-grown *N*LG samples.[202] The well-aligned *n*LG edge can be denoted as $n\mathrm{LG}_{n\mathrm{E}}$, where the subscript E refers to 'edge'. In the general case, a specific alignment configuration at the *n*LG edge is the well-aligned edge of *m*LG (including *m* = 1) lying on (*n*–*m*)LG, denoted as $n\mathrm{LG}_{m\mathrm{E}}$ ($n > m$). The edge of a graphene layer lying on (*n*−1)LG, denoted as $n\mathrm{LG}_{1\mathrm{E}}$, is a building block for MLG edges, and, thus, the edges of each graphene layer in Fig. 17(d) can be denoted as $1\mathrm{LG}_{1\mathrm{E}}$, $2\mathrm{LG}_{1\mathrm{E}}$, $3\mathrm{LG}_{1\mathrm{E}}$, and $4\mathrm{LG}_{1\mathrm{E}}$.

Raman spectroscopy is a rapid and nondestructive technique to identify MLG edges.[207,218] Fig. 17(e) depicts the Raman spectra of a graphene flake at $n\mathrm{LG}_{1\mathrm{E}}$ edges (*n* = 1, 2, 3, 4), which can be clearly identified in the optical image. The D-band profile at $n\mathrm{LG}_{1\mathrm{E}}$ resembles that of ion-implanted *n*LG. Because only one graphene layer contributes to the D band at $n\mathrm{LG}_{1\mathrm{E}}$ ($n > 1$), its intensity is weaker than that at the corresponding $n\mathrm{LG}_{n\mathrm{E}}$.

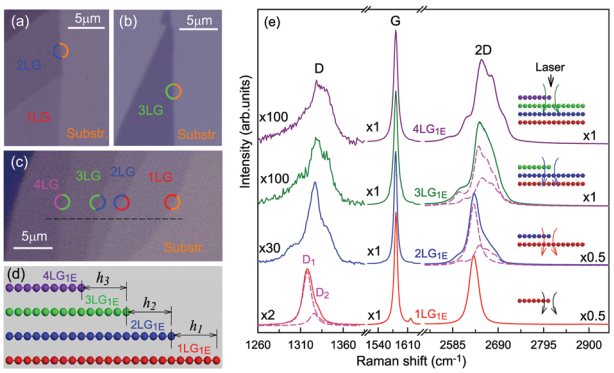

Fig. 17 Optical microscope images of (a) 2LG and (b) 3LG with well-aligned edges, and (c) a graphene flake containing 1LG, 2LG, 3LG, and 4LG. (d) Schematic diagram of side-view alignment configuration at the edges of the graphene flake in (c). h_i (i = 1, 2, 3) refer to the misalignment distances between the edges of two adjacent misaligned graphene layers. (e) Raman spectra at the edges of $n\mathrm{LG}_{1\mathrm{E}}$ (*n* = 1, 2, 3, 4) as indicated by the circles in (c). The dashed lines show the 2D bands of 1LG and 2LG (2LG and 3LG) used to fit that at $2\mathrm{LG}_{1\mathrm{E}}$ ($3\mathrm{LG}_{1\mathrm{E}}$). Reproduced with permission from ref. 207. Copyright 2015, Elsevier.

The 2D bands at nLG$_{1E}$ ($n > 1$) are composed of the 2D bands from nLG and (n−1)LG, as shown by the dashed lines in Fig. 17(e). Moreover, based on the spectral features of the D and 2D bands, the alignment configurations of the edges in NLG can be identified.[207] It is possible to identify the misalignment distance between 2LG$_{1E}$ and 1LG$_{1E}$ of 2LG down to the nanometer scale.[218]

5.4 Probing the nature of defects in graphene by Raman spectroscopy

According to their nature and origin, defects in graphene can be defined such as edges, implanted atoms, vacancies, grain boundaries, and defects associated with a change in carbon hybridization, for example, from sp^2 to sp^3.[206] One, two, or more kinds of defects can exist in a graphene sample. The general models for point defects introduced by implanted atoms, line defects, and edges have been discussed above. Vacancies (see Fig. 18(a)) can be viewed as point defects[15,16,237] that are slightly different from common point defects[66,219] induced by the ion-implantation technique. The grain boundaries are the interfaces between two graphene domains with different crystallographic orientations and can be defined by the misorientation angle between two crystalline domains,[238] *e.g.*, the misorientation angle for grain boundary in Fig. 18(b) is 27°. This type of defect can behave as a line defect.[208] However, it is difficult to define a similar parameter for the vacancy and grain boundary defects in the same way as the L_D and L_a parameters in common point or line defects.

The sp^3-type defects are usually induced by chemical decoration, such as mild oxidation, hydrogenation, or fluorination.[130,239–242] Thus, they are also known as chemical defects. By attaching exotic atoms to each site of graphene, as illustrated in Fig. 18(c), the optical, electronic, and magnetic properties can be modified. For example, the change of the hybridization of carbon atoms from sp^2 to sp^3 can remove the conducting π band and open the energy gap[240,242,243] or form local magnetic moments.[244,245] Therefore, the quantitative characterization of such defects in graphene-based systems *via* Raman spectroscopy is of intense research interest.

Here, we take fluorinated graphene as an example to elucidate the Raman fingerprint of sp^3-type defects (chemical derivatives),[130,246] which can be prepared by the mechanical cleavage of graphite fluoride or by exposing the graphene to atomic fluorine compounds such as XeF_2 and CF_4 plasma. Fig. 18(d) shows the Raman spectra of fluorinated graphene after repeated exposure to XeF_2 plasma. As shown in the figure, prominent defect-induced D and D′ peaks have emerged. Fig. 18(e) summarizes I(D)/I(G) and I(2D)/I(G). The I(D)/I(G) ratio suddenly increases after the initial fluorination and then gradually decreases to saturation upon increasing the fluorination time. However, the I(2D)/I(G) ratio monotonically decreases. Both the G and 2D modes broaden and the D′ peak overlaps with the G modes after continuous fluorination. I(G) changes only slightly for fluorination times of less than 9 h. Although it is difficult to characterize the sp^3-type defect concentration quantitatively in this case, I(D)/I(G) and I(2D)/I(G) follow a two-stage evolution, as depicted in Fig. 14(b and c).

Compared with the other types of defects, one characteristic feature of sp^3-type defects is that such defects can be partially recovered under specific conditions.[235,240,246] In the case of

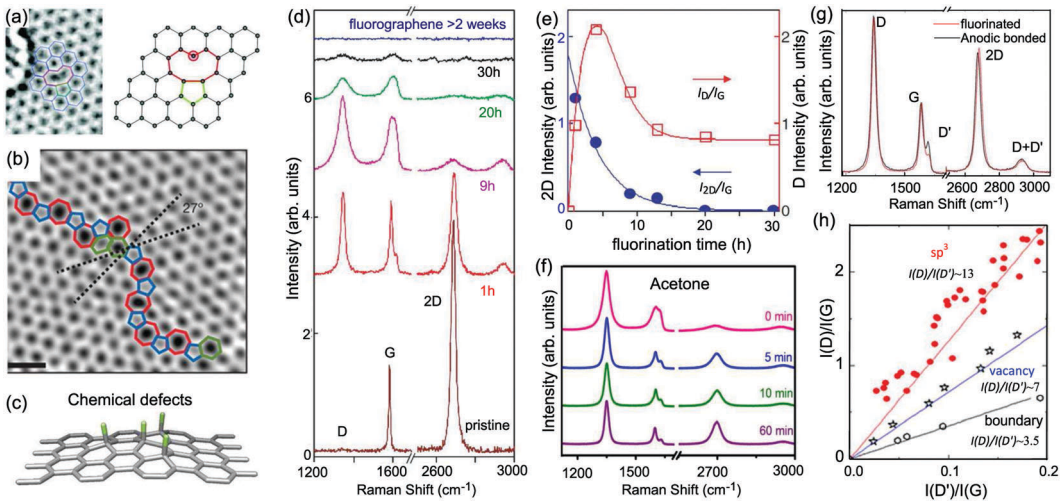

Fig. 18 Representative schematics of (a) vacancies, (b) grain boundaries, and (c) chemical defects (sp^3-type defects). Reproduced with permission from ref. 208, copyright 2011, American Chemical Society, ref. 233, copyright 2011, Nature Publishing Group, and ref. 234, copyright 2017, American Chemical Society. (d) Raman spectra of as-prepared fluorinated graphene exposed to XeF_2 for different fluorination times. The Raman spectra are offset for clarity. (e) I(D)/I(G) and I(2D)/I(G) as a function of fluorination time. Reproduced with permission from ref. 130. Copyright 2010, Wiley Online Library. (f) Raman spectra of as-prepared fluorinated graphene (SF_6, 25 W, 2 min) and fluorinated graphene after different treatment times in different solvents, such as acetone. Reproduced with permission from ref. 235. Copyright 2017, Wiley Online Library. (g) Raman spectrum of fluorinated (red) and defective graphene produced by anodic bonding (black), showing the same D, G, and 2D intensities but different D intensities. (h) I(D)/I(G) *vs.* ratio I(D′)/I(G), showing the linear dependence between the two parameters at low defect concentration, giving different I(D)/I(D′) for different types of defects. Data are from ion-bombarded graphene,[16,66] oxidized graphene,[131] and graphite with different grain sizes.[236] The solid lines are eye guides. Reproduced with permission from ref. 206. Copyright 2012, American Chemical Society.

fluorinated graphene, it is reported that the initial fluorine desorption occurs at around 300 °C, leading to the recovery of the graphene lattice.[246–249] The solvent used in the transfer process can also be used for defluorination.[235] Fig. 18(f) plots the Raman spectra of as-prepared fluorinated graphene after fluorination (25 W, 1 min) using SF_6 as the source gas and those after different treatment times in acetone. The recovery of the 2D peak and weakening of $I(D')$, as well as the reduction in the FWHM of all peaks, can be clearly observed, implying that the sample undergoes defluorination. After defluorination, although the $I(2D)/I(G)$ ratio increases, $I(D)/I(G)$ is still so large that the full recovery of defects cannot occur. The sharp D peak after the defluorination process is attributed to the presence of vacancies in the fluorinated graphene, which cannot be recovered again after treatment in acetone.[235] The defluorination is more likely to occur in a more polar solvent, such as acetone, isopropanol, and deionized water, because a polar solvent is more likely to interact with the F atoms attached to the graphene.

Until now, significant work has been performed to investigate the nature of defects in graphene-based systems, usually using the D and D′ modes.[206] Generally, both the D and D′ modes show similar trends in peak intensities and widths at low defect concentrations. In this case, $I(D)$ and $I(D')$ increase with increasing ion dose and fluorination time, as shown in Fig. 14(a) and 18(d), respectively. When investigating the intensities, different types of defects can induce different features in the D and D′ modes. Two representative Raman spectra (with low defect concentrations) of fluorinated graphene and defective graphene obtained by anodic bonding in graphene are shown in Fig. 18(g), where the D, G, and 2D modes exhibit similar intensities but those of $I(D')$ are quite different. Fluorinated graphene has a higher $I(D)/I(D')$ than defective graphene formed by anodic bonding. Considering both D and D′ modes are defect-induced modes, $I(D)$ and $I(D')$ are linearly proportional to the defect concentration. Consequently, $I(D)/I(D')$ only depends on the physical origin of the defect but is independent of the defect concentration. This suggests that $I(D)/I(D')$ can be used to identify the nature of the defects.[206] Using a systematic analysis of their relationship of all types of defects, such as sp^3-type defects, vacancies, and boundaries, the $I(D)/I(D')$ values are revealed to reach maximum ($\sim$13) for sp^3-type defects and decrease to $\sim$7 for vacancies and $\sim$3.5 for boundaries. Interestingly, $I(D)/I(D')$ of the pristine defects introduced by anodic bonding is the same as that of ion-implanted graphene, which is an indicator of vacancy-like defects. Therefore, $I(D)/I(D')$ can be used experimentally to obtain information on the nature of defects in graphene. This makes Raman spectroscopy a powerful tool to fully characterize the disorder in graphene.

6 Identifying number of layers of graphene flakes by Raman spectroscopy for standardization

There are several hundred companies worldwide producing or using graphene-based materials. Many issues concern the large-scale production, processing, and application of graphene-based materials outside of the laboratory. For industry to have confidence in the graphene materials that are produced commercially, the properties of these materials must be accurately, reliably, and reproducibly measured. For example, the properties of graphene flakes are strongly related to their thickness, *i.e.*, number of layers (N), and, thus, the determination of N of graphene flakes is critical for quality appraisal in graphene industrial products. According to the N-dependent band lattice vibrations and band structures, the value of N of graphene flakes can be identified by several parameters (position, profile, and intensity) of the corresponding Raman bands. Thus, Raman spectroscopy can be expected to serve as a robust, fast, accurate, nondestructive, and even substrate-free approach for the N counting or thickness identification of graphene flakes[168] produced by micromechanical exfoliation, CVD growth, or transfer processes on various substrates, bridging the gap between the characterization and international standardization of the thickness determination of graphene flakes and the gap between academia and industry.

6.1 Identification of monolayer graphene

The $I(G)$ of NLG deposited on a SiO_2/Si substrate increases monotonically until reaching ten or more layers and decreases for thicker graphene flakes.[168,250] To identify N of NLG by $I(G)$, the crucial step is to distinguish 1LG in the graphene flake. For exfoliated flakes on a SiO_2/Si substrate, the 2D band exhibits a single Lorentzian peak, while AB-nLG ($n > 1$) and ABC-nLG ($n > 2$) exhibit broad bands, which can be fitted by several Lorentzian peaks.[115,168] Therefore, the profile of the 2D band can be used to identify 1LG in the exfoliated flakes, as shown in Fig. 19(a). This method is a substrate-free approach to identify the exfoliated 1LG on any substrate.

It is challenging to identify 1LG produced by CVD and other methods. For example, CVD-2LG tends to be t(1+1)LG, in which the 2D-band profile is mostly likely to be a single Lorentzian peak with a blueshift in peak position because of its small Fermi velocity.[187] Therefore, a single Lorentzian peak of the 2D band is no longer a reliable index to identify 1LG in CVD-grown flakes. The $I(G)$ of 1LG on a multilayer dielectric substrate is mainly modified by the multiple reflections at the interfaces and optical interference within the medium. If the CVD-grown flake contains 1LG, its $I(G)$ should be approximately equal to that of ME-1LG when they are deposited on the same substrate. Thus, ME-1LG can be considered as a standard sample when it is transferred onto the same substrate as the CVD-grown flake to be characterized. By comparing the $I(G)$ of the CVD-grown flake with that of the standard ME-1LG, CVD-1LG can be easily identified. Indeed, as shown in Fig. 19(b), the $I(G)$ values of CVD-1LG and ME-1LG on SiO_2/Si are identical, although $\omega(G)$ of CVD-1LG is blueshifted to 1590 cm^{-1} because it is slightly doped. Meanwhile, ME-1LG and CVD-1LG deposited on the same substrate should have similar optical contrast, almost identical amplitudes, and similar profiles, as demonstrated in the inset to Fig. 19(b), which is helpful to further confirm the identity of CVD-1LG.

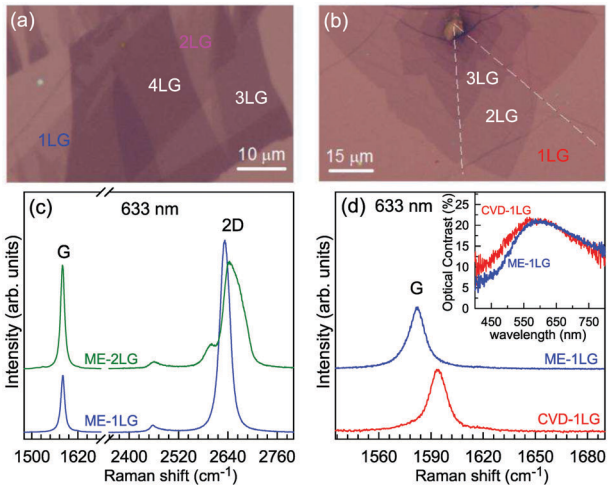

Fig. 19 Optical images of (a) ME-*N*LG and (b) CVD-*N*LG flakes. The scale bars are shown. (c) Raman spectra of ME-1LG and ME-2LG. (d) Raman spectra of CVD-1LG and ME-1LG both deposited onto 90 nm-SiO_2-thick SiO_2/Si substrates. Inset: optical contrast spectra of ME-1LG and CVD-1LG. The excitation wavelength for Raman spectra is 633 nm. Reproduced with permission from ref. 205. Copyright 2017, Wiley Online Library.

This approach can be extended to identify 1LG produced by other methods, such as epitaxial growth on SiC. The 2D band of *N*LG epitaxially-grown on SiC also exhibits a single Lorentzian peak.[251] Thus, it is necessary to transfer ME-1LG onto SiC for use as a standard sample to identify 1LG epitaxially grown on SiC.

6.2 Intensity of the G and Si peaks

Once 1LG has been determined, the experimental I(G) of *N*LG, *i.e.*, I_{NLG}(G), normalized by I_{1LG}(G) must be compared with the theoretical one to precisely identify N of the graphene flakes. If *N*LG is exfoliated on the SiO_2/Si substrate, I_{NLG}(G) is modified by multiple reflections at the interfaces and optical interference within the four-layer structure, which contains air($\tilde{n}_0$), *N*LG($\tilde{n}_1$, d_1), SiO_2($\tilde{n}_2$, d_2), and Si($\tilde{n}_3$, d_3), where $\tilde{n}_i$ and d_i (i = 0, 1, 2, 3) are the complex refractive index and the thickness of each medium, respectively, as shown in Fig. 20(a). The thickness of the SiO_2 layer is denoted as h_{SiO_2}. The transfer-matrix method can quantify the Raman intensities of *N*LG on multilayer structures,[73,252] in which excitation wavelength, objective NA, and Raman tensor must be considered, and the s- and p-polarization components should be treated separately.[73,252]

Fig. 20(b) shows the experimental and theoretical I_{NLG}(G)/I_{1LG}(G) for *N*LG transferred onto a Si(110) substrate covered with 89 nm SiO_2. I_{NLG}(G)/I_{1LG}(G) is not monotonically dependent on N. However, the case of the Si Raman signal from the SiO_2/Si substrate beneath the *N*LG (denoted as I_G(Si)) is different. I_G(Si) decreases monotonically with increasing N because both the laser excitation and the Raman signal from the Si substrate are absorbed by the *N*LG flake. If I(Si) from the bare SiO_2/Si substrate is denoted as I_0(Si), I_G(Si)/I_0(Si) can be used to identify graphene flakes with N up to 100 because of the strong Si Raman signal and high signal-to-noise ratio of I_G(Si)/I_0(Si), as shown in Fig. 20(c). In general, this technique can be utilized to identify N of mechanically exfoliated *N*LG or epitaxially-grown *N*LG on SiC, whose complex refractive index is not sensitive to the N of *N*LG. This technique is not suitable for CVD-grown *t*NLG because its I(G) exhibits N-dependent resonant behavior.

It should be noted that both I_{NLG}(G)/I_{1LG}(G) and I_G(Si)/I_0(Si) are very sensitive to h_{SiO_2}, objective NA, and laser wavelength (λ_{las}). To get reliable theoretical values of I_{NLG}(G)/I_{1LG}(G) and I_G(Si)/I_0(Si) to precisely identify the N of graphene flakes, h_{SiO_2} must be confirmed by initial measurement by a spectroscopic ellipsometer or another technique, and it is better to use an objective with an NA smaller than 0.55. Considering that I_G(Si)/I_0(Si) < 0.45 when $N > 10$, one can identify N ($N < 10$) of *N*LG by I_{NLG}(G)/I_{1LG}(G) with a constraint condition of I_G(Si)/I_0(Si) > 0.45. In principle, it is sufficient to determine N up to 10 because the electronic structure of *N*LG rapidly evolves with N, approaching the three-dimensional limit of graphite at 10 layers.[22]

6.3 Peak profile of the 2D mode

As discussed above, the peak profile of *N*LG also shows N-dependent spectral features. Because the 2D band originates from a two-phonon DR Raman process, it is closely related to

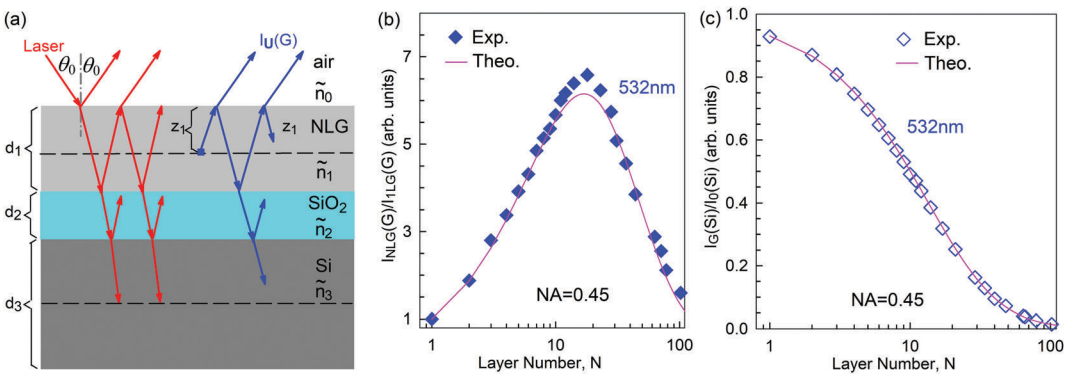

Fig. 20 (a) Schematic diagrams of multiple reflections and optical interference in the multilayer structures containing air, *N*LG, SiO_2, and Si for the incident laser and outgoing Raman signals (the G peak from *N*LG). The experimental (Exp.) and theoretical (Theo.) (b) I_{NLG}(G)/I_{1LG}(G) and (c) I_G(Si)/I_0(Si) (d) as a function of N of *N*LG flakes. The objective numerical aperture (NA) is 0.45. The excitation wavelength is 532 nm. Reproduced with permission from ref. 252. Copyright 2015, Royal Society of Chemistry.

the band structure of the graphene layers. 1LG has a single and sharp 2D band, but the 2D band of *N*LG can be fitted by multiple Lorentzian peaks because of the multiple resonance Raman processes related to its electronic band structures. Ferrari *et al.*[44] clearly explained the changes of the 2D bands of monolayer and bilayer graphenes based on their line shape and peak positions. Zhao *et al.*[115] have demonstrated that the 2D-band profiles of 1LG and AB-stacked *N*LG ($N < 5$) excited at 633 nm clearly exhibit distinct subpeaks, which can be used to identify 1LG and AB-stacked 2–4LG with AB stacking, as shown in Fig. 5, while the 2D bands excited by blue or green lasers do not exhibit these distinct features even for 3LG. However, for more than five graphene layers, the difference between their Raman spectra is insufficient to distinguish them accurately. Because the different components of the 2D band may exhibit different resonant behaviors with different laser excitations, it is very important to choose an appropriate laser wavelength to identify *N* of *N*LG.[115]

The peak profile of the 2D band can also be used to determine whether mechanically-exfoliated *N*LG is ABC-stacked.[5,6,150]

6.4 Peak positions of the C and LB modes

According to the LCM, ω(C) and ω(LB) of AB- and ABC-*N*LG are directly determined by *N*. However, at room temperature, only the C_{N1} modes can be observed in AB-*N*LG,[70] and both the C and LB modes are absent in ABC-*N*LG.[150] Based on $\omega(C_{N1}) = \omega(C_{bulk})\cos(\pi/2N)$, one can determine *N* of AB-*N*LGs up to an *N* of 5.[70] However, the weak $I(C_{N1})$ limits its application in the determination of *N* for AB-*N*LG.

For the *tN*LG, because of the formation of a Moiré superlattice, the band structure of *tN*LG is quite different from its constituents. A series of VHSs appear in the $JDOS_{OAT}$ of *tN*LG, as revealed from its optical contrast.[57] *I*(C) and *I*(LB) are significantly enhanced in *tN*LG once the excitation energy is in resonance with the energies of the VHSs in the $JDOS_{OAT}$, as shown in Fig. 10. Because the interface shear coupling in *tN*LG is only ~20% of the corresponding value in graphite, whereas the interface layer-breathing coupling in *tN*LG is almost identical to the bulk case, the observed C modes in *tN*LG are related to the shear vibrations of its constituents and the LB modes are revealed to be dependent on the total *N* of *tN*LG but not on its constituents. Therefore, The LB modes can be used to identify the number of layers of *tN*LG, while the C modes provide a convenient method to determine the number of layers of its constituents. For example, in *t*(2+3)LG, under the resonant condition, one can observe the C_{21} mode of the AB-2LG constituent, the C_{31} and C_{32} modes of the AB-3LG constituent, and the LB_{51} and (or) LB_{52} modes corresponding to AB-5LG. Because twisted stacking commonly occurs in CVD-MLG, this technique has been developed to distinguish the stacking orders of CVD-grown *tN*LG.[202,205]

In short, this approach, based on the interlayer vibrational modes, is a robust, nondestructive, and substrate-free way to identify *N* of AB-*N*LG and CVD-grown *tN*LG and the number of layers of the constituents in *tN*LG. The method can be extended to the determination of *N* of ultrathin flakes of other two-dimensional materials, such as semimetals ($NiTe_2$ and VSe_2),[253] semiconductors (WS_2, WSe_2, MoS_2, $MoSe_2$, $MoTe_2$, TaS_2, $RhTe_2$, and $PdTe_2$),[151,155,156,254–259] insulators (HfS_2),[260] superconductors (NbS_2, $NbSe_2$, $NbTe_2$, and $TaSe_2$),[261–263] and topological insulators (Bi_2Se_3 and Bi_2Te_3).[160,264,265]

7 Raman spectra of monolayer and multilayer graphenes under external perturbation

Graphene and MLG under external perturbation have attracted considerable attention because external perturbations can modify the electric, phonon, thermal, and mechanical properties of *N*LG. This facilitates various applications such as in tunable photonic devices, flexible electronics, FETs, and catalysts for hydrogen evolution.[110,266] For example, the band gap of AB-2LG can be widened under an asymmetric electric field.[267,268] Under the magnetic field, the quantum Hall effect and Berry phase in 1LG can be observed.[98,269,270] Negative thermal expansion coefficients have also been observed.[271,272] In addition, high-performance elastic properties and intrinsic strengths have been observed under stress.[273,274]

Raman spectroscopy is an ideal technique to probe the influence of external environmental conditions on material systems by spectral-feature analysis with high spectral resolution.[56] This makes Raman spectroscopy useful in fundamental research and device characterization. Indeed, the phonon spectra of graphene are significantly affected by external perturbations, and their responses to external perturbations can be precisely probed by Raman spectroscopy.[56,98,275] In the following sections, we will discuss how external perturbations, such as doping induced by an electric field[58–60,62–65] and charge transfer,[61] strain,[81–87] and temperature,[99–103,276] modify the Raman spectra of graphene and MLG and how to use Raman spectroscopy to probe those external perturbations.

7.1 Doping

The Fermi level of graphene can be tuned by doping, which makes it a candidate for use in electronic and photoelectric devices.[266,277–279] The carrier density in graphene layers can reach a high level *via* electronic doping and chemical doping. By means of electronic doping, a gate voltage is used to tune the Fermi level, in which the doping level of graphene can reach up to 5×10^{13} cm^{-2}. Furthermore, A strong perpendicular electric field can open up a band gap of ~0.3 eV in 2LG.

Doped graphene at various top-gated voltages has been characterized by Raman spectroscopy, as shown in Fig. 21(a).[60,63] The G peak stiffens and sharpens for both electron and hole doping (see Fig. 21(a and b)), implying the breakdown of the adiabatic Born–Oppenheimer (ABO) approximation.[63] The 2D peak will blueshift monotonically when it is p-doped, but redshift when it is n-doped (see Fig. 21(c)).[60,63] The doping level can be determined by *I*(2D)/*I*(G), as shown in Fig. 21(d), and will be discussed in detail later. Moreover, two splitting G modes (a symmetric, in-phase Raman-active mode and an

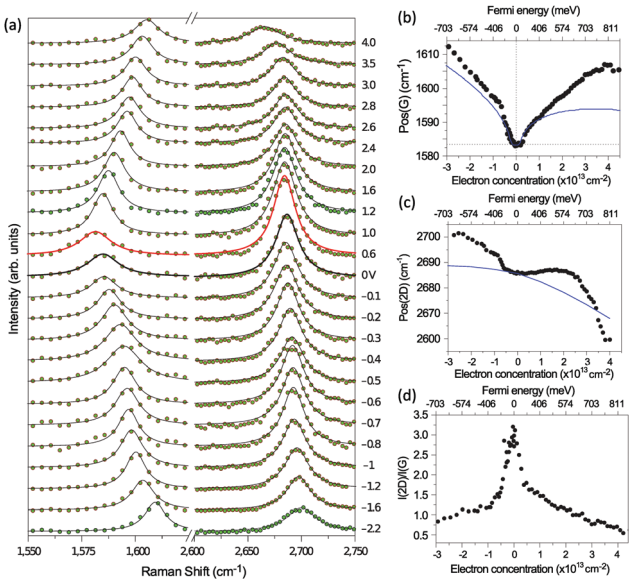

Fig. 21 (a) Raman spectra at gate voltages between −2.2 and 4.0 V. The dots are the experimental data, the black lines are fitted Lorentzian peaks, and the red line corresponds to the Dirac point. Pos(G) (b), FWHM(G) (c), and I(2D)/I(G) (d) as a function of electron and hole doping. Reproduced with permission from ref. 60. Copyright 2008, Nature Publishing Group.

antisymmetric, out-of-phase Raman inactive mode) in 2LG, arising from the interlayer coupling, can be observed upon applying a perpendicular electric field, which can be created, for example, by top and bottom gates of opposite bias in field-effect devices. This is because the electrical field reduces the symmetry of graphene bilayer by removing the inversion center, resulting in new eigenstates, G^+ and G^-, that are linear combinations of the in-phase and out-of-phase modes.[62,145] In addition, the ubiquitous substrate-mediated mechanical strain in 2DMs can also lead to the Raman shifts. This effect should be carefully distinguished from the charge doping effects based on the Raman spectroscopic analysis.[280]

Besides electrostatic doping, *N*LG can also be doped chemically by depositing or adsorbing atoms/molecules on one or both sides, and a charge carrier density is introduced by charge transfer between the chemical impurity and graphene layers.[281–285] When 1–4LG flakes were dipped into sulfuric acid, H_2SO_4 molecules were found to be only physically adsorbed on the surface layers of the graphene flakes as an electron–acceptor dopant without intercalation.[115] For example, 18 M H_2SO_4 can be used to fully dope *N*LG, whose Raman spectra are almost identical to those of stage-*N* graphite intercalation compounds (GIC), as shown in Fig. 22(a). Here, the stage-*N* GIC means a *N*LG sandwiched by two intercalant layers.[121] The G peak of H_2SO_4-doped 1LG blue-shifts to 1624 cm^{-1} from that (1582 cm^{-1}) of pristine flakes. The doped 2LG has a single G peak at 1613 cm^{-1}, which indicates symmetric doping on both sides, and there is no net electric field between the layers.[115] Two G peaks (G^+ and G^-) have been observed in H_2SO_4-doped 3LG and 4LG. The G peak splitting shows that doping is primarily in the surface graphene layers, creating perpendicular electric fields that point inward. The interior layers have lower hole densities. This situation could also be created by top and bottom gates of the same voltage in a device configuration. With further increasing *N*, the electric field no longer penetrates the innermost layers, and, thus, the outermost two graphene layers on each surface have non-negligible doping, but the interior layers are undoped and experience no electric field. Thus, the $I(G^-)$ of the interior layers increases with increasing *N*.

Chemical doping of *N*LG ($N > 1$) can also be realized by intercalating molecules or atoms into the graphene layers, resulting in stage-*n* GIC with $n \leq N$. In fact, stage-*n* GIC can be considered as *n* graphene layers sandwiched by two intercalant layers,[121] where two adjacent *n*-graphene-layers are decoupled from each other. The charge transfer between intercalants and graphene layers in stage-*n* GIC makes the *n* graphene layers heavily doped.[61,286] This can also occur for *N*LG, and the *N*LG IC is formed.[61,286] *N*LG flakes can be intercalated by $FeCl_3$ by a two-zone vapor transport method to form stage-1 *N*LG ICs

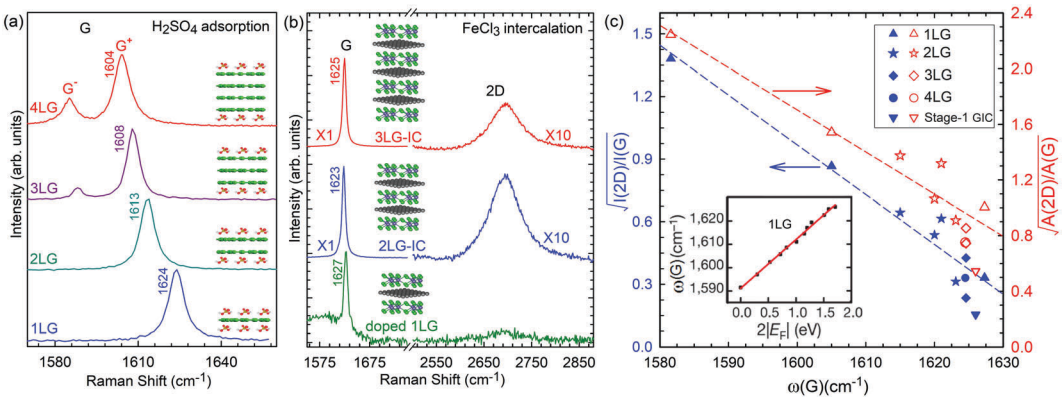

Fig. 22 (a) Raman spectra of 1–4LG when sulfuric acid molecules are adsorbed on both sides. Adapted with permission from ref. 115. (b) Raman spectra of doped 1LG and stage-1 2–3LG intercalation compounds with $FeCl_3$, excited by 532 nm. (c) Variation of $\sqrt{I(2D)/I(G)}$ and $\sqrt{A(2D)/A(G)}$ as a function of $\omega(G)$ for doped 1LG, stage-1 2–4LG intercalation compounds, and stage-1 graphite intercalation compounds. Inset: $\omega(G)$ as a function of $|E_F|$. Reproduced with permission from ref. 61. Copyright 2011, American Chemical Society. The inset in panel (c) was reproduced with permission from ref. 58. Copyright 2011, Nature Publishing Group.

(see Fig. 22(b)). Fig. 22(b) also shows that ω(G) of pristine 2LG and 3LG is significantly blueshifted to $\sim$1624 cm^{-1} after the intercalation, and their 2D bands exhibit a single Lorentzian profile, resulting in electronic decoupling of each layer in 2LG and 3LG ICs. The E_F of stage-1 *N*LG ICs can be as large as 0.9 eV, which can be confirmed by multi-wavelength Raman spectroscopy.[61]

To determine the doping level of 1LG by Raman scattering, in addition to multi-wavelength Raman spectroscopy,[61] the E_F of p-doped 1LG or stage-1 *N*LG ICs can also be determined from ω(G) and $\sqrt{A(2D)/A(G)}$. Wang and co-workers found that[58] the relationship between the Fermi level shift and ω(G) peak position is linear if the Fermi level shift is larger than $\sim$0.1 eV, as shown in the inset of Fig. 22(c). One can use the following relationship to determine the doping level,

$$|E_F| = \Delta\omega(G)/21, \quad (14)$$

where $\Delta\omega$(G) is the frequency difference of the G mode between doped and pristine 1LG, and E_F is in eV. Furthermore, considering the influence of electron–electron interactions in 1LG, E_F as a function of $\sqrt{A(2D)/A(G)}$ can be written as follows:[61]

$$|E_F| = 0.9\sqrt{\frac{A(G)}{A(2D)}} - 0.23, \quad (15)$$

where E_F is in electronvolts. It must be noted that eqn (15) works only at an excitation wavelength of 514 nm. For other excitation wavelengths, the parameters in eqn (15) should be modified. Based on eqn (14) and (15), $\sqrt{A(2D)/A(G)}$ is linear with ω(G). Indeed, the data collected from different doping levels of doped 1LG and *N*LG ICs show a linear relationship between $\sqrt{A(2D)/A(G)}$ (also $\sqrt{I(2D)/I(G)}$) and ω(G). In stage-1 $FeCl_3$-GIC, eqn (15) gives $|E_F| \sim 0.85$ eV, similar to that determined by the multi-wavelength Raman method.[61]

7.2 Magnetic fields

When graphite is exposed to a perpendicular magnetic field (B), the carriers precess around the zone edge in two-dimensional circular orbits, resulting in its electronic spectrum quenching into discrete Landau levels (LLs).[287] This is also the case for 1LG. 1LG under **B** exhibits discrete fourfold (spin and valley) degenerate LLs with energies $E_n = \mathrm{sgn}(n)\sqrt{2|n|\hbar\tilde{c}}/l_B$, where $n = \ldots, -2, -1, 0, 1, 2, \ldots$ is the index of LLs in the conduction ($n > 0$) and valence ($n < 0$) bands, $\tilde{c}$ and $l_B = \sqrt{\hbar/eB}$ are the electron velocity of the Dirac cone at zero B, and the magnetic length, respectively,[104] as shown in Fig. 23(a). The LL occupancy is characterized by the filling factor, $\nu = 2\pi {l_B}^2 \rho_s$, where ρ_s is the carrier density. Fully filled LLs with $n = 0, 1, \ldots$ have $\nu = 2, 6, \ldots$[104] Electron excitations between LLs can be described in terms of magneto-excitons. If the energy of an optical phonon matches that of the inter-Landau-level (LL) transitions, the effects of electron–phonon interactions will be enhanced, so-called magnetophonon resonances (MPRs).[88,94,95,98,288] According to the matrix structure of the interaction terms between different LLs, the following selection rules are optically active in 1LG:[289] (i) $n^- \rightarrow n^+$; (ii) $(n \mp 1)^- \rightarrow (n \mp 1)^+$; and (iii) $n^- \rightarrow (n+1)^+$, $(n+1)^- \rightarrow n^+$, which belong to the symmetry representations A_2, A_1, and E_2, respectively, originating from the prescribed hexagonal symmetry (C_{6v}) of the band structures in 1LG.[89,289] Thus, in 1LG, the doubly degenerate E_{2g} phonon at Γ (the so-called G mode) can interact strongly with the LL transitions (iii) with E_2 symmetry. This strong interaction results in the renormalization of the phonon frequencies and the line broadening of the G mode,[60,62–64,290,291] which can be tuned by electric and magnetic fields through Fermi energy shifts and Landau quantization. Furthermore, the selection rules of circular polarization for various LL transitions (originating from the angular momentum transfer), *e.g.*, σ^+ for $-n \rightarrow n+1$ and σ^- for $-n-1 \rightarrow n$ valence-to-conduction band transitions (σ^+ and σ^- represent right- and left-hand circular polarization, respectively), make the MPRs distinguishable for lattice vibrations under different circular polarizations.

Indeed, the MPR effect can be described as a resonant mixing of electronic and lattice excitations into a combination mode, leading to splitting and, thus, EPC-dependent anticrossings.[88] Because the σ^+ and σ^- magnetoexcitons are based on different LL transitions, changing the carrier density and, thus, the LL occupancy in 1LG would affect the splitting of the phonon fine structure differently.[88,94,95] For example, filling (depleting) the final states with electrons or depleting (filling) the initial states would block the corresponding LL transitions, thus suppressing (promoting) coupling between magnetoexcitons and phonons. This progress can be expressed by the so-called splitting, g, introduced in ref. 88, as depicted in Fig. 23(b). If $\nu = 0$, corresponding exactly to a half-filled $n = 0$ LL, the coupling strengths of σ^+ and σ^--polarized modes are equal, causing the G peak to split equally for σ^+ and σ^- phonon polarizations.[88] For $0 < \nu < 2$, in which $n = 0$ LL is more than half-filled, the $-1 \rightarrow 0$ (σ^-) transition becomes partly blocked, while the $0 \rightarrow +1$ (σ^+) transition is promoted, giving rise to different splittings in the fine structure of the σ^+- and σ^--polarized modes. When $2 < \nu < 6$, the $n = 0$ LL is fully occupied, leaving no space for MPRs with the σ^- phonon, whereas the $n = +1$ LL is only partly filled, resulting in a MPR-induced fine structure in the σ^+ phonon line shape (with maximum splitting at $\nu = 2$). Finally, if $\nu > 6$, both $-1 \rightarrow 0$ and $0 \rightarrow 1$ transitions are blocked, completely suppressing the MPR-induced fine structure of both modes. Therefore, the $\sigma^\mp$ can be resolved by MPR effects using various excitation/detection configurations.[88,89] Furthermore, the splitting of G peaks induced by the MPR effects can be grouped into three categories as a function of ν.[88,95] Based on the Dyson equation under the resonance approximation,[88,95] the frequencies of the G peak at $\nu < 2$ (0.4×10^{12} cm^{-2}) and $2 < \nu < 6$ (2.0×10^{12} cm^{-2}) after coupling with magneto-excitons can be calculated, as depicted in Fig. 23(c) (dashed lines). The strongest anticrossing corresponding to $0 \rightarrow 1$ (σ^+) and $-1 \rightarrow 0$ (σ^-) is shown under a magnetic field of 20–25 T.

Fig. 23(d and e) show the polarization and B dependence of the G peak at different carrier densities in terms of experiments. At a high carrier density ($\nu > 6$), there is no significant

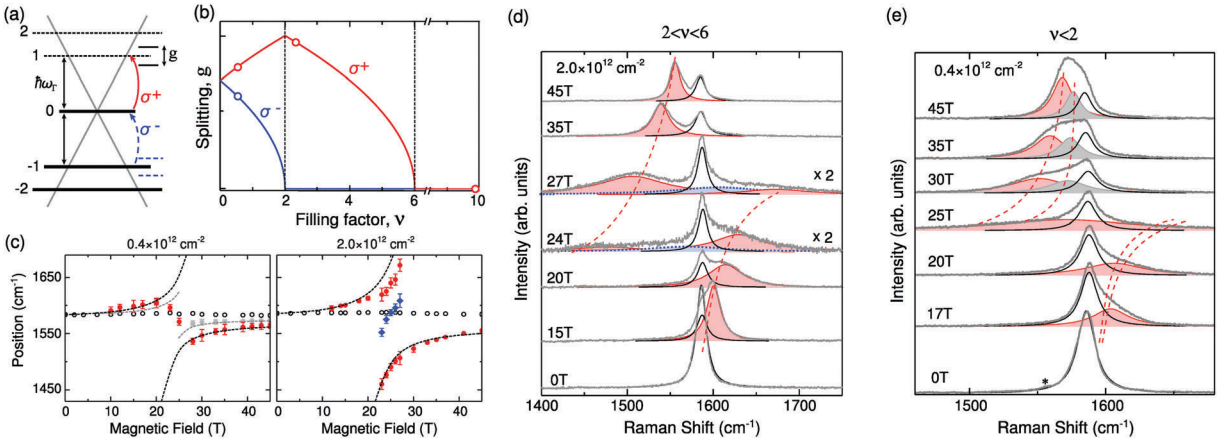

Fig. 23 (a) 1LG band structure at **B** = 0. Mode splitting ensues in the vicinity of the MPR between 0 → 1 electron–hole excitations and the E_{2g} phonon. (b) Calculated mode splitting g_σ as a function of the filling factor, ν. Open circles indicate the filling factors probed by experiment. (c) Peak position of the G peak Lorentzian components as a function of **B** for the (left) low and (right) intermediate carrier densities. Open black circles represent the central E_{2g} phonon line component. Filled red (σ^+) and gray (σ^-) circles are the electron–phonon coupled modes. Dashed lines plot the calculated frequencies of the G modes interacting with the magneto-exciton based on the Dyson equation.[88] Blue squares show additional components observed close to resonance. Circular-polarized magneto-Raman spectra at (d) $2 < \nu < 6$ and (e) $\nu < 2$. The pink spectrum shows the component corresponding to σ^+, and the gray spectrum shows the component corresponding to σ^-. Reproduced with permission from ref. 95. Copyright 2013, American Physical Society.

change in the G peak.[95] When the carrier density is $\sim 2 \times 10^{12}$ cm^{-2}, the G peak exhibits a strong, anticrossing like splitting, reaching ~ 150 cm^{-1} (~ 20 meV) for **B** = 25 T, as shown in Fig. 23(d). The electron–phonon coupled modes appear only in the σ^+ geometry, implying MPRs at $2 < \nu < 6$. As the carrier density further decreases so that $\nu < 2$, the G peak splitting changes (Fig. 23(e)). In contrast to the $2 < \nu < 6$ case, the coupled modes now appear in both σ^+ and σ^- polarizations. The spectra at **B** > 30 T reveal that the coupled mode consists of two peaks (pink and gray peaks), which can be assigned to the $\sigma^\pm$ polarized modes originating from the coupling of E_{2g} phonons with $0 \rightarrow 1$ and $-1 \rightarrow 0$ magnetoexcitons. All the experimental data are in agreement with those calculated, as shown in Fig. 23(c). It should be noted here that the additional component at an intermediate carrier density inside the anticrossing gap (Fig. 23(d)) results from the overall effect of inhomogeneous strain.

A similar MPR effect has been observed in 1LG on the surface of graphite,[91,92,96] non-Bernal stacked MLG on SiC,[90] ABA- and ABC-stacked 3LG,[97] and bulk graphite.[93] In addition, a simultaneous redshift and line broadening of the 2D mode in a magnetic field have also been revealed, which are attributed to the modified momenta of the optical phonons emitted during the double resonance Raman scattering process.[292] A knowledge of the Raman spectra of graphene flakes under a magnetic field can be helpful in uncovering the subtleties of the magneto-phonon resonance. The mode splitting can be further utilized to estimate the strength of electron–phonon coupling and to distinguish various circular-polarized lattice vibrations.

7.3 Strain and stress

The application of an external stress on a crystal results in a lattice strain, *i.e.*, a change in the interatomic distances and consequent redistribution of the electronic charge. In graphene, strain can even open the band gap.[85,293] Isotropic compression (hydrostatic pressure) generally results in an increase in the frequency of the vibrational modes (phonon hardening), while isotropic tension results in a decrease in the vibrational frequency (phonon softening).[294] The Grüneisen parameter gives the rate of change of a given phonon frequency with strain in a crystal. In metrology applications, accurate values of Grüneisen parameters are crucial for quantifying the amount of strain in the system, which can be estimated by probing the phonon frequency change from its value in the absence of strain.

Graphene bubbles and balloons can be used to study the Raman spectrum of graphene under biaxial strain.[147,295] Graphene bubbles are formed during the deposition of large graphene flakes on an oxidized silicon substrate. Bilayer graphene balloons are produced by pressurizing a specially made metallic container covered with large bilayer graphene membranes with nitrogen gas, as shown in Fig. 24(a). The Raman shifts of the G and 2D modes in the graphene bubbles are shown in Fig. 24(b and c), respectively. All the Raman modes redshift under the tensile strain. The Grüneisen parameters (γ) of the G (1.8), 2D (2.6), D (2.52), and 2D′ (1.66) peaks have been measured, and they are in excellent agreement with calculated parameters.[84,147] Because the initial doping or strain caused by the interaction between graphene and the substrate can strongly affect the measured Grüneisen parameters, graphene bubbles are a better system to observe the pure strain effect on the Raman modes.[147] For the Raman spectrum of bilayer graphene balloons, the strain does not alter the AB-stacking configuration when the strain is less than 1.2%, as shown in Fig. 24(d).

The application of anisotropic stress, *e.g.*, uniaxial strain, has more complex effects. The uniaxial strain can break the symmetry, resulting in the lifting of the degeneracy of phonon frequencies.[84,294] The G mode, which arises from the doubly degenerate E_{2g} mode in the intrinsic 1LG, will split into two peaks,

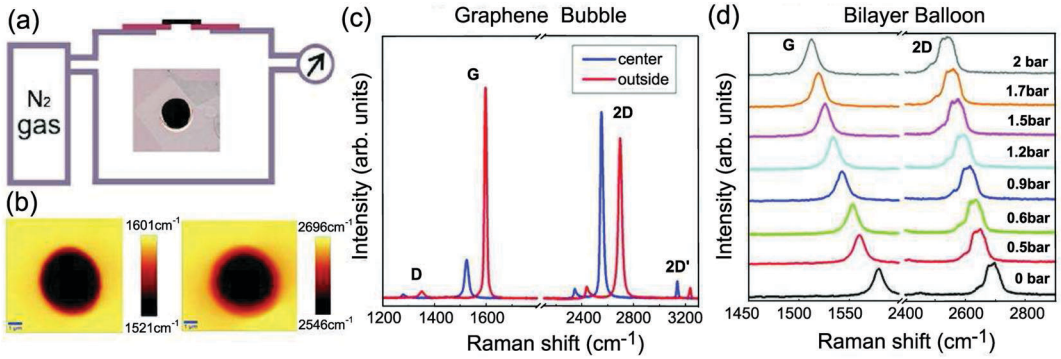

Fig. 24 (a) Schematic showing the experimental setup used to make the graphene balloons. The inset shows an optical micrograph of a large bilayer covering a 50 μm aperture in a copper scaffold. (b) Raman map of the G and 2D peak positions for a graphene bubble. The 2D and G peak positions decrease significantly when moving from the substrate to the center of the bubble. (c) Raman spectra measured at the center of a single-layer bubble and on the flat area on the substrate at 488 nm. (d) Raman spectra of a bilayer graphene balloon measured at different differential pressures at 514.5 nm. Reproduced with permission from ref. 147. Copyright 2012, American Chemical Society.

G^+ and G^- (E^+_{2g} and E^-_{2g}). The eigenvectors of the G^+ and G^- are orthogonal.[81,84,87,147,294,296] When the uniaxial tension strain is applied, sp^2 bonds along the direction parallel to the applied strain are lengthened and softened, yielding the G^- peak, while those perpendicular to it are only slightly affected, giving the G^+ peak. Thus, under uniaxial strain, only the peak of the G^- mode is significantly shifted relative to the G peak of unstrained 1LG (by as much as 30 cm^{-1} for 1.3% strain), while the peak G^+ mode is only moderately shifted (up to 15 cm^{-1}). Because this effect is purely mechanical,[84,294] the FWHM of G^- and G^+ remain constant. For the 2D band, the FWHM is also unchanged but the peak can redshift and split because of the softening of the TO phonon and the changing band structure.[81–83,85] Moreover, according to the Raman tensor, the E^+_{2g} and E^-_{2g} modes are polarized.[297] The polarized directions of those modes are orthogonal, which results in E_{2g} showing a depolarization behavior in the intrinsic 1LG. The intensities of the two peaks G^- and G^+ vary with the polarization of the scattered light along the direction of the strain, allowing the crystallographic orientation with respect to the strain to be probed.[87,294,298] A good understanding of the Raman spectrum in graphene under strain can help us to characterize the wrinkles in CVD-grown graphene,[299,300] understand the strain transfer in supported graphene,[301] and investigate the properties of the graphene engine.[302]

7.4 Temperature

Phonon anharmonicity in a solid is a fundamental topic in solid state physics. Temperature-dependent Raman spectroscopy is a powerful technique to probe the phonon anharmonicity. In the first-order approximation, the frequency of a Raman mode is linear with temperature, *i.e.*, $\Delta\omega = \chi\Delta T$, where χ is the first-order temperature coefficient. The frequency shift of the Raman mode with temperature can be represented as follows:[303]

$$\Delta\omega = \left(\frac{d\omega}{dT}\right)_V \Delta T + \left(\frac{d\omega}{dV}\right)_T \left(\frac{dV}{dT}\right)_P \Delta T = (\chi_T + \chi_V)\Delta T, \quad (16)$$

where χ_T and χ_V represent the shift arising from the direct coupling of the phonon modes (denoted as a pure temperature effect) and the thermal expansion induced by the volume change (denoted as pure volume effect), respectively.

The pure temperature coefficient for pristine graphite was found to be $\chi_T = -0.011$ cm^{-1} K^{-1} while χ_V can be ignored in the measured temperature range.[303] In most experiments, both contributions are reflected in the extracted values of the temperature coefficient and it must be interpreted as the sum of both contributions,[303,304] *i.e.*, $\chi = \chi_T + \chi_V$.

Temperature-dependent Raman spectra of 1LG and MLG have been measured by several groups.[99,101,103,304] The extracted values of the 1LG and AB-2LG temperature coefficient of the G mode are $-(1.6 \pm 0.2) \times 10^{-2}$ cm^{-1} K^{-1} and $-(1.5 \pm 0.06) \times 10^{-2}$ cm^{-1} K^{-1}, respectively.[99,101,103,304] The temperature coefficient of the 2D mode is $-(3.4 \pm 0.4) \times 10^{-2}$ cm^{-1} K^{-1} for 1LG, which means the 2D peak is more sensitive to the temperature than the G mode.[305] The uncertainty may result from factors such as the cleanliness of the sample, influence of the substrate, doping, and disorder. Once the χ values of 1LG and MLG have been determined, the temperature of the graphene flakes can be obtained *in situ*. This temperature measurement method can be utilized to determine the thermal conductivity[102,103,276,306] and thermal expansion coefficient[271] of 1LG and the thermal transport of graphene FETs[307] by *in situ* Raman spectroscopy.

8 Raman images of graphene flakes

Confocal Raman spectroscopy gives spatially resolved information about the vibrational spectrum, so-called Raman images. A state of the art Raman imaging system can achieve a spatial resolution of ~300 nm if we do not use some special techniques, such as near-field Raman technique, tip enhanced Raman scattering (TERS),[311] or microspheres (or lens). With the development of high-performance charge-coupled devices (CCDs) and also the optimization of optical items, the integration time required for obtaining a smooth Raman spectrum can be as short as milliseconds, which greatly minimizes the time to acquire

Raman imaging. Raman images can be generated based on different parameters of Raman peaks, *e.g.*, peak intensity, peak area (or integrated intensity), position, width, and also the ratios or differences between two peaks. As mentioned above, the Raman spectra of graphene are sensitive to its morphology and external perturbations. Thus, Raman images of graphene can yield information concerning the spatial distribution of the number of layers, stacking order, defects, doping, strain, and temperature, which is important for device applications.[5,77,109,307,309,312–315] In this section, we show several examples of Raman images of graphene with different morphologies and external perturbations, including the number of layers, stacking order, edge, strain, and temperature. Raman images can also be used to reveal the growth mechanism of graphene flakes.

8.1 Number of layers, crystal domain, and stacking order

As discussed above, the I(G) of a graphene flake depends on its number of layers, N.[252,308,312] Thus, Raman intensity images can offer an identification to N of graphene flakes with high spatial resolution. Indeed, using the Raman intensity image in Fig. 25(a), one can identify 1–4LG.

A significant proportion of CVD-grown 2LG is twisted 2LG. There are several single crystal domains in each *t*2LG flake. Polygonal domains in CVD-grown *t*2LG flakes evoke the orientation θ_t-dependent grain structure, as shown in Fig. 25(b), where the dark field (DF)-TEM image is a false color composite of the domains mapped individually by diffraction-filtered imaging.[185] Each *t*2LG exhibits a θ_t-dependent band structure and optical properties, resulting in θ_t-dependent I(G), as discussed in Section 4.3. The right panel of Fig. 25(b) clearly demonstrates that the variations in Raman intensity are strongly correlated with θ_t; furthermore, I(G) is nearly constant within a domain. In particular, there is a strong enhancement of the G band integrated area for a few specific domains, such as the 12.4° domain excited at 2.33 eV. Thus, the single crystal domains can be distinguished by Raman images of I(G) with an appropriate excitation energy.

The stacking order of MLG affects the band structure, and the band structure can be revealed by the profile of its 2D band. For example, ME-*N*LG exhibits different stacking orders, *i.e.*, AB and ABC, in the same flake.[5] The different DR resonant processes result in different FWFM(2D) for AB- and ABC-stacked MLG. Therefore, FWHM images of the 2D band can yield a stacking distribution in the ME-*N*LG, especially ME-3LG and -4LG, as shown in Fig. 25(c).

8.2 Edges and strain

The edge is a special defect[59] that can also activate the D peak. Based on the DR Raman process, the D peak cannot be activated at a perfect zigzag edge, although it is observable at the armchair edge. I(D) at the armchair edge shows polarization dependence.[59] Thus, by fixing the laser polarization at a particular angle, the Raman mapping of I(D) can be used to identify the chirality of the graphene edge.[75] As shown in the left panel of Fig. 25(e), the two edges with angles of 90° in the same flake can be determined as armchair and zigzag edges based on the absence and appearance of the D peak, respectively. The two edges with angles of 60° in the same flake are armchair edges, which can also be confirmed from the right panel of Fig. 25(e).

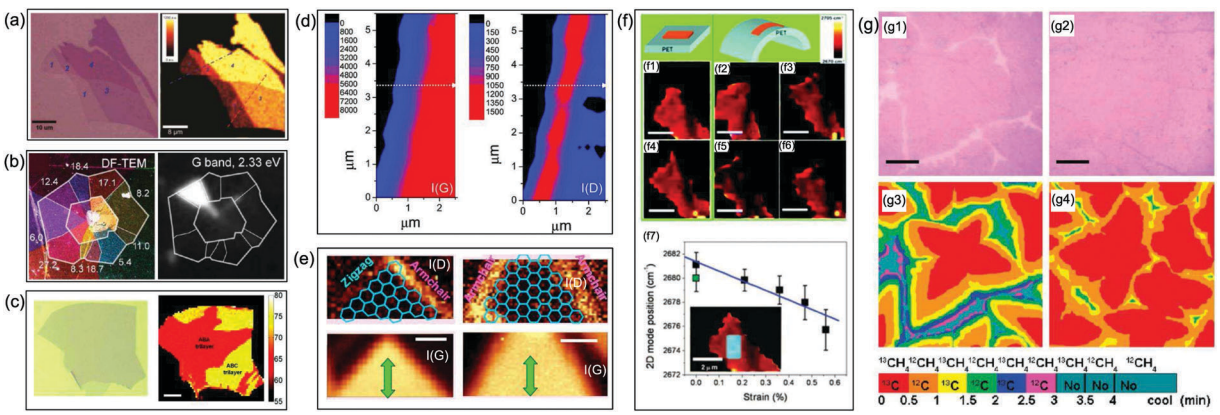

Fig. 25 (a) Optical image and Raman image of I(G) of graphene flakes with one, two, three, and four layers. Reproduced with permission from ref. 308. Copyright 2007, American Chemical Society. (b) DF-TEM of a *t*2LG flake (θ_t is labeled for each domain in the TEM image) and Raman image of I(G) of the same *t*2LG sample. Reproduced with permission from ref. 185. Copyright 2012, American Chemical Society. (c) Optical images and spatial maps of FWHM(2D) for 3LG samples under 514 nm excitation, where the red and yellow regions correspond to ABA and ABC 3LG domains, respectively. The scale bars are 10 μm in length. Reproduced with permission from ref. 5. Copyright 2010, American Chemical Society. (d) Raman maps of I(G) and I(D) in the proximity of the graphene edge. Reproduced with permission from ref. 77. Copyright 2009, American Chemical Society. (e) Raman imaging of I(D) and I(G) at edges with angles of 90° (zigzag and armchair) and of 60° (armchair). The images of I(G) show the positions and shapes of the 1LG sheets. Green arrows: the laser polarization. The superimposed frameworks are eye guides indicating the edge chirality. Reproduced with permission from ref. 75. Copyright 2008, AIP Publishing. (f) Raman images of (f1) unstrained graphene, (f2–f5) strained graphene, and (f6) relaxed graphene by extracting ω(2D) and (f7) mean of ω(2D) of the entire graphene as a function of strain. The inset shows the area of interest subjected to statistical analysis. The bending/strain is in the horizontal direction. Reproduced with permission from ref. 309. Copyright 2008, American Chemical Society. (g) Optical micrographs of the isotope-labeled graphene grown under isothermal conditions with different P_{Me}, (g1) 160 and (g2) 285 mTorr, and the corresponding Raman images of ω(G), (g3) 160 mTorr, and (g4) 285 mTorr, which schematically show the isotope distributions of ^{12}C and ^{13}C. The colors are decoded in the color bar with methane dosing sequences and times. Scale bars are 5 μm. Reproduced with permission from ref. 310. Copyright 2010, American Chemical Society.

However, one cannot exclude the existence of some zigzag fragments in the armchair edges only by using Raman images.

Strain has a large influence on the frequency shift of the G and 2D bands.[84] If graphene is mechanically exfoliated on a polyethylene terephthalate (PET) film, tensile strain is introduced into the graphene layer on the top surface of the PET film by bending, as shown in Fig. 25(f). The amount of strain is determined by dividing the increase in length of the strained top surface by the unstrained length. Fig. 25(f) shows an image of ω(2D) of the graphene layer on PET under strain.[309] The strain distribution is not perfectly uniform because of the contact between graphene and PET. Consequently, the van der Waals force between the graphene and substrate differs from region to region, which is revealed in the Raman image of ω(2D). Fig. 25(f7) shows the mean of ω(2D) from the entire graphene sample as a function of strain, which can be applied to analyze the strain status of graphene in related devices.

8.3 Growth mechanism

CVD growth on Ni and Cu provides large area graphene that can be transferred to other substrates after the removal of the metal by wet chemical etching. However, the temperature, methane-to-hydrogen ratio, growth pressure, and substrates are also critical parameters affecting the structural perfection of the CVD-grown graphene.[310,316–318] A technique based on isotope labeling has been widely used to reveal the growth mechanism of low-dimensional materials, such as single-walled carbon nanotubes and graphene.[318] The same materials grown with different isotopes exhibit different physical and chemical properties because of the different masses of the isotopes. In particular, the frequencies and linewidths of Raman modes in materials labeled by isotopes will be significantly different between different isotopes. For example, ω(G) of ^{13}C graphene is located at $\sim$1520 cm^{-1}, while that of ^{12}C graphene is located at 1582 cm^{-1}.[318] Thus, Raman mapping of ω(G) in the graphene labeled with ^{13}C and ^{12}C during the growth sequence and with time allows the mechanism of graphene growth by CVD to be determined.

Large area graphene can be grown by the CVD of methane on Cu foils. The growth parameters such as temperature (T), methane flow rate (J_{Me}), and methane partial pressure (P_{Me}) could affect the domain size and crystal quality of the grown graphene film. The effect of P_{Me} on graphene growth kinetics has been studied under isothermal conditions with a fixed T of 1035 °C and J_{Me} of 7 standard cubic centimeters per minute (sccm). To grow graphene using the C isotope labeling technique, the Cu surface was exposed to $^{13}CH_4$ and $^{12}CH_4$ (normal methane) sequentially. Because graphene growth on Cu occurs by surface adsorption, the isotope distribution in the local graphene regions will reflect the dosing sequence and can be mapped according to their different ω(G). Fig. 25(g1 and g2) show optical micrographs of graphene grown under P_{Me} of 160 and 285 mTorr, and the corresponding Raman images of ω(G) are shown in Fig. 25(g3 and g4), respectively, where the isotope distributions of the two cases using the A(G) of ^{13}C graphene at 1490–1550 cm^{-1} and that of ^{12}C graphene at 1550–1610 cm^{-1} are indicated in the color bar with methane dosing sequences and time. Under the condition of P_{Me} = 160 mTorr (Fig. 25(g3)), graphene growth terminated after the sixth dose (3 min) and achieved a maximum coverage of $\sim$90%. Afterward, there was no change, even though the Cu surface was further exposed to CH_4. However, graphene growth terminated after the fourth dose (1.5 min) and achieved a full coverage in the case of P_{Me} = 285 mTorr, as shown in Fig. 25(g4). Additionally, the growth rate of graphene sharply reduced with increasing coverage at both pressures because of C species formed by the Cu-catalyzed decomposition of CH_4, as shown Fig. 25(g3 and g4). When the Cu surface is undersaturated, there is no nucleation for graphene even though C_xH_y converts to the vapor phase. However, graphene starts to nucleate, grow, and becomes an island under saturation conditions, stopping because the lack of C_xH_y means that C cannot be absorbed on the island edges. That is, partial coverage on the Cu surface is achieved by the formation of graphene islands. Furthermore, when the Cu surface is supersaturated, graphene islands continue to grow to form graphene domains, fully covering the Cu surface because of sufficient C_xH_y.

This Raman imaging technique based on isotope labeling can also be utilized to monitor the other parameters of graphene growth, such as T and J_{Me}. Moreover, the growth mechanism of other 2DMs can also be optimized by this method.

9 Raman spectroscopy in graphene-based materials

9.1 Graphene quantum dots and carbon dots

Graphene quantum dots (GQDs) and carbon dots (C-dots) are typical graphene materials with a lateral size down to the nanometer scale.[322,323] GQDs and C-dots have attracted a great deal of attention in recent years because of their promise in bioimaging,[324] optoelectronic devices,[325] pollutant detection,[326] and catalysis.[327]

GQD is also referred to as nanographene. GQDs are originally defined as the products obtained by cutting graphene into small pieces with dimensions of a few nanometers (2–20 nm).[328] GQDs are crystalline and mainly composed of sp^2-hybridized carbon.[329] With time, small disks with dimensions of a few nanometers cut from MLGs have also become known as GQDs. Quantum confinement and edge effects in GQDs with sizes of less than 100 nm become pronounced as the sheets become smaller, particularly once their dimensions fall below 10 nm.[329] This results in nonzero band gaps, leading to strong photoluminescence once the GQD size is sufficiently small. The band gaps of GQDs can be tuned by changing their size, shape, and geometry, as well as the nature of their edges.[68,328,330–334] The correlation between size and band gap has been demonstrated by scanning tunneling spectroscopy experiments.[333]

Atomic force microscopy (AFM) images of as-grown GQDs on SiO_2 substrates with different growth durations are shown in Fig. 26(a–c).[68,335] In the early growth stages, GQDs are nucleated everywhere on the SiO_2 surface (Fig. 26(a)). The larger graphene islands are $\sim$1.2–1.5 nm thick, which is equivalent to four or five layers, as confirmed by the AFM measurements

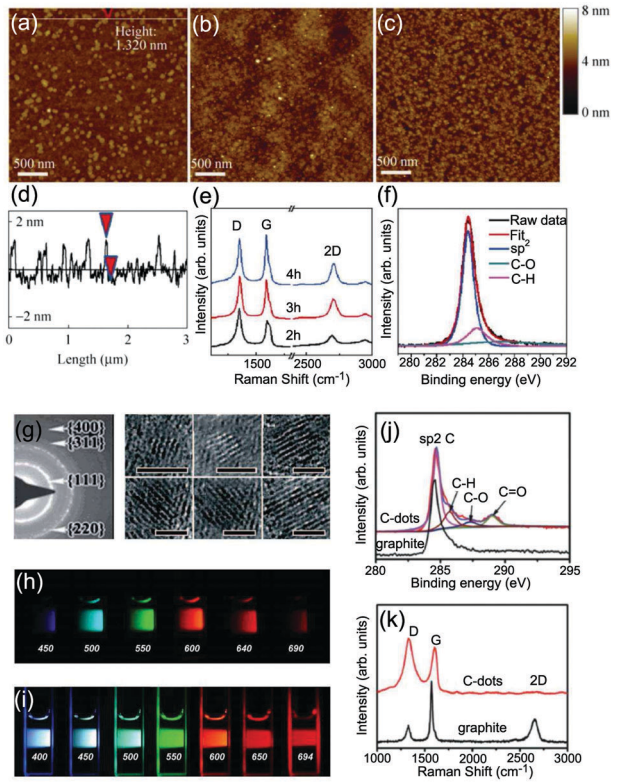

Fig. 26 AFM images of graphene grown on SiO_2 with growth durations of 2 (a), 3 (b), and 4 h (c). Topography height profile (d) along the line shown in image (a). (e) Raman spectra of the graphene shown in (a–c), measured at 633 nm excitation with a ~1 μm beam spot. (f) X-ray photoelectron spectroscopy (XPS) characteristics of the as-grown graphene, with binding energies ranging from 280 to 292 eV. Reproduced with permission from ref. 68. Copyright 2011, Tsinghua University Press and Springer-Verlag, Berlin, Heidelberg. (g) Selected area electron diffraction (SAED) pattern and high-resolution (HR)-TEM images of C-dots with different diameters. Reproduced with permission from ref. 319. Copyright 2012, Royal Society of Chemistry. Aqueous solution of the polyethylene glycol (PEG1500N)-attached carbon dots (h) excited at 400 nm and photographed through band-pass filters of different wavelengths, as indicated, and (i) excited at the indicated wavelengths and photographed directly. Reproduced with permission from ref. 320. Copyright 2006, American Chemical Society. (j) XPS spectra of graphite and C-dots. (k) Raman spectra (λ = 633 nm) of graphite and C-dots. Reproduced with permission from ref. 321. Copyright 2012, Royal Society of Chemistry.

shown in Fig. 26(d). Continued growth yields more nucleation sites on the surface of SiO_2, resulting in the whole surface being covered with a continuous and uniform GQD film. Further growth results in thicker GQDs (Fig. 26(c)) with 6–7 layers. Fig. 26(e) shows the Raman spectra of the samples shown in Fig. 26(a–c). The D, G, and 2D peaks show characteristic spectral features of disordered graphene structures.[49,56] A high I(D) originates from either small crystallite sizes or an abundance of edges, as discussed in Section 5.[56,77] The I(D)/I(G) ratio decreases and I(2D) increases as the growth time increases, which means that a higher quality nanographene film is obtained over time, consistent with the AFM images.[15] The XPS spectrum of the as-grown GQD film on SiO_2 with a dominant sp^2 peak shown in Fig. 26(f) confirms its graphene structure.[68]

C-Dots are quasi-spherical carbon nanoparticles with diameters of 2–10 nm that have a high oxygen content and consist of combinations of graphitic and turbostratic carbon in various volumetric ratios (see Fig. 26(g)).[320,328,336] The graphitic structure of C-dots is also apparent in the XPS spectra,[321] which contain a strong peak corresponding to sp^2 carbon atoms, as shown in Fig. 26(j). Therefore, C-dots can be considered as a kind of graphene-based material. In particular, compared with conventional inorganic quantum dots, C-dots have many advantages, including low toxicity, chemical inertness, and biocompatibility.[319,328,337] Typical C-dots have excellent water solubility and are suitable for subsequent functionalization with various organic, polymeric, inorganic, or biological species.[338] C-dots with well-defined dimensions and tunable surface functionalities can be used as building blocks for advanced functional architectures.[319,328] The most characteristic and significant property of C-dots is their relatively strong photoluminescence, which depends on their size, the excitation wavelength, and the surface functionalization, as shown in Fig. 26(h and i).[320,339] The Raman spectra of C-dots contain characteristic D and G bands at about 1350 and 1600 cm^{-1}, respectively, as shown in Fig. 26(k). The high I(D)/I(G) ratio indicates its small size, the presence of turbostratic carbon, and disordered surface structures.

9.2 Nanoribbons

Graphene nanoribbons (GNR) are a special graphene material with two edges. Both the edge effects and quantum confinement effect must be considered to understand their Raman spectra. Therefore, the Raman spectrum of a GNR is similar to that of graphene edges and is also dependent on its width.[19–21,79,227,340,341] The edges are in a perfect position to add functional groups, and the type of functional group affects the properties of the GNRs and the corresponding Raman spectra.[19,21]

Fig. 27(a) shows four GNRs, which are functionalized with long alkyl chains ($-C_{12}H_{25}$) to increase solubility.[342] The structures in Fig. 27(a(i–iii)) represent a series of 'cove-shaped' GNRs with the same edge pattern and increasing width, where a benzo ring periodically decorates the zigzag (ZZ) edge. These structures are labeled nCNRs, where n indicates the width of the ZZ GNR core (here, n = 4, 6, 8).[343] In addition to those samples, Fig. 27(a(iv)) also shows a GNR based on the chiral-edged (4,1)-GNR with periodically fused benzo rings; this is called m-ANR in ref. 343. The m-ANR has the same width as the 8CNR, but its 'chirality' leads to slightly different edge patterns.

In the ultralow frequency region, there is a new Raman peak corresponding to radial-like breathing mode (RLBM),[344] which is the relative in-plane vibration between the atoms close to the edges. The frequency of the RLBMs is between 120 and 250 cm^{-1}, as shown in Fig. 27(b). The RLBM is especially sensitive not just to the width but also to the edge modulation and functionalization, making it very different from the ideal cases studied to date, where the RLBM does not show a significant dependence on edge type.

The G peaks of all the GNRs in Fig. 27(a) are upshifted (~1605 cm^{-1}) and broader (FWHM ~ 25 cm^{-1}) than that (FWHM ~ 15 cm^{-1}) of pristine graphene, as shown in Fig. 27(c).

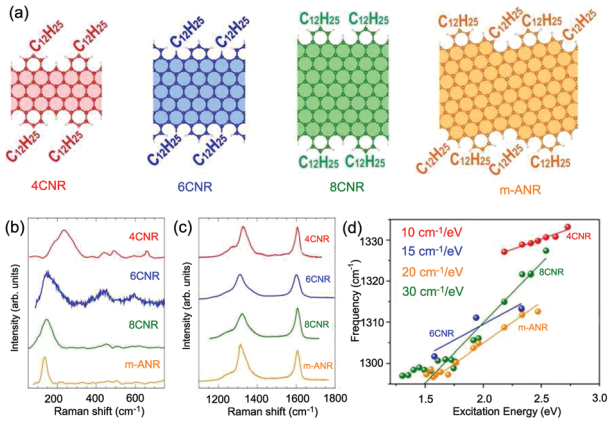

Fig. 27 (a) Structural models of the GNRs. Ball-and-stick representation of the atomic structure of the cove-shaped GNRs investigated, *i.e.*, 4CNR, 6CNR, 8CNR, and *m*-ANR. The schematics show the characteristic variable width of these GNRs and the location of the alkyl side chains in each case. The shaded areas indicate the corresponding zigzag/chiral GNRs. (b) Low- and (c) high-frequency regions of the Raman spectrum for the cove-shaped GNRs in (a). The 4CNR and 6CNR were excited at ~2.4 eV, while 8CNR and *m*-ANR were excited at ~1.9 eV. (d) Peak dispersion of GNRs as a function of excitation energy for the D peaks. Reproduced with permission from ref. 21. Copyright 2016, American Chemical Society.

Similar results were observed in small graphite domains[50] and polycyclic aromatic hydrocarbons (PAH)[345] because of the relaxation of the momentum conservation induced by the finite size.

Fig. 27(c) also shows a prominent D peak that is characterized by a dominant component at about 1310–1330 cm^{-1} with an intensity comparable to that of the G peak and one or more shoulders at its lower energy side. In graphene, the D peak activated by the intervalley DR process[69] is strongly dispersive with an excitation energy arising from a Kohn anomaly at *K*,[129] where the typical phonon dispersion of graphene is ~50 cm^{-1} eV^{-1}.[44,77] In the case of GNRs, smaller D-peak dispersions of 10–30 cm^{-1} eV^{-1} have been measured for the different GNRs, as shown in Fig. 27(d). The observed dispersion is expected to be related to some disorder-induced scattering, for example, edge functionalization, defects formed during the GNR production, or length distribution. Thus, the small dispersion of the D peak can be used to fingerprint the presence of GNRs and differentiate them from other sp^2 carbon nanostructures.

9.3 Graphene layers grown on SiC

Graphene can be epitaxially grown on Si terminated SiC (Si-SiC) and C terminated SiC (C-SiC) substrates,[346–348] which is suitable for large area fabrication and is more compatible with current Si processing techniques for future applications. Epitaxial graphene (EG) may interact with the SiC substrate, which could modify its optical and electronic properties. A bandgap of ~0.26 eV was observed by angle-resolved photoemission spectroscopy, which can be attributed to the interaction of EG with the SiC substrate. Fig. 28(a) shows the top view and side view of a graphene on the SiC(0001) surface. A 13 × 13 graphene lattice lies above the $6\sqrt{3}$ reconstructed SiC surface. The small and the large black circles represent $\sqrt{3}$ and $6\sqrt{3}$ lattices, respectively.

Fig. 28(b) shows the intrinsic Raman spectrum of the EG sample on SiC. The G and 2D peaks show different blueshifts in peak position with respect to ME-1LG.[251,349] The blueshift varies by up to 18 cm^{-1} for the G peak and 35 cm^{-1} for the 2D peak,[251] and the G mode on SiC is broadened. The blueshift of the G and 2D peaks cannot be attributed to charge transfer[60] from defects and the substrate but, instead, is due to the presence of compressive strain in the graphene layer.[349,350] The small difference between the lattice constant of the reconstructed 13 × 13 graphene layer supercell (ε_G = 31.923 Å) and the reconstructed SiC $6\sqrt{3} \times 6\sqrt{3}$ supercell (ε_{SiC} = 31.935 Å) cannot account for the significant amount of strain measured. However, compressive strain at room temperature in the graphene layer can be ascribed to the large difference in the coefficients of thermal expansion between graphene (ρ_G)[351] and SiC (ρ_{SiC})[352] during the cooling process from the synthesis temperature.[349,350] If the epitaxial film is in mechanical equilibrium with the SiC surface, as a stress-free monolayer commensurate with the $6\sqrt{3}$-reconstructed SiC surface at T_s, a large compressive strain would develop in the film during the cooling process because SiC contracts on cooling whereas graphene expands.[350]

Fig. 28(c) shows the thickness-dependent Raman spectra of the EG samples on a C-SiC substrate.[251] The 2D mode of

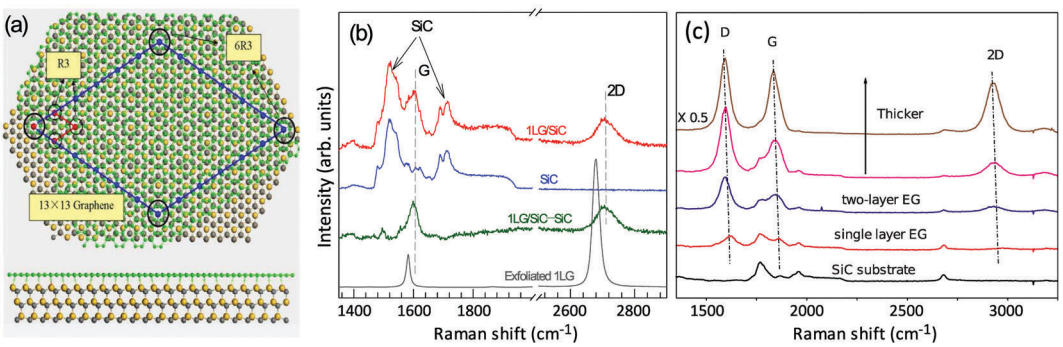

Fig. 28 (a) Top and side views of a graphene on the SiC(0001) surface. The green, yellow, and gray spheres represent C in graphene and Si and C in SiC, respectively. (b) Raman spectra of 1LG on SiC (1LG/SiC), SiC, graphene (by subtracting the SiC spectrum from that of 1LG/SiC), and exfoliated 1LG (1LG/SiC-1LG) in the SiC, G and 2D mode spectral region. (c) Raman spectra of epitaxial graphene layers (EGs) on the C-SiC substrate with different thicknesses. Panels (a and c) were reproduced with permission from ref. 251. Copyright 2008, American Physical Society.

EG samples on C-SiC (also Si-SiC) substrates exhibits a single Lorentzian profile no matter how many layers exist in the EG samples. It has been experimentally shown that MLG grown on the carbon terminated face of 4H-SiC does not grow as simple AB stacked layers.[353] Instead, MLG grows with a high density of rotational faults where adjacent sheets are rotated about 2° relative to each other. First principles calculations demonstrate that the small twist angle between adjacent graphene layers produces an epitaxially-grown MLG on SiC with an electronic structure that is indistinguishable from an isolated single graphene sheet in the vicinity of the Dirac point.[353] This explains its single-layer electronic properties, even though the film is composed of tens of graphene layers. Therefore, the 2D mode of epitaxial MLGs on C-SiC and Si-SiC substrates exhibits similar lineshapes to that of graphene. As the thicknesses of epitaxial MLG increase, the Raman peaks (D, G, and 2D) of epitaxial MLG shift to lower frequencies, *i.e.*, toward that of bulk graphite. This can be easily understood because, when the thickness of epitaxial MLG increases, the effect of the substrate on epitaxial MLG becomes weaker and the lattice of epitaxial MLG relaxes.

9.4 CVD-grown multilayer graphene

CVD can grow graphene films of high quality.[7,317] Given the many possible applications of high-quality graphene, routes toward industrial-scale synthesis are of great importance. For most industrial-level devices (and other) applications, large single-crystal graphene films are ideal for top-down processing. In the past ten years, the island size of single-crystal graphene has increased by more than four orders of magnitude, from micrometers to inches. Raman spectroscopy has been widely used to characterize the quality, disorder, domain boundaries, and doping of CVD-grown graphene films. However, we do not address the Raman spectra of CVD-grown graphene films because they are almost identical to those of mechanically-exfoliated 1LG.

When the growth conditions are optimized, MLG flakes can also be grown by CVD. CVD-grown *N*LG (CVD-*N*LG) with transparency, high electrical conductivity, and flexibility is considered to be a candidate for transparent and conducting electrodes, which could be used in touchscreen panels, organic light-emitting diodes, and solar cells.[356–359] By changing the growth conditions, *N*LG with different stacking orders, including AB and twisted stacking, can be obtained. Here, we will review Raman features of CVD-2LG, -3LG, and thicker flakes.[172,173,185,186,202,205,354,355,360,361]

2LG islands can be observed in the CVD-1LG film with appropriate growth conditions.[185,186] These islands sitting on 1LG have in general a multilobe star morphology. The lobes constitute the second layer and, in the center, three or more stacked layers can be identified by optical contrast when using an optical microscope, as shown in Fig. 29(a).[185] In particular, it has been shown that a significant proportion of CVD-2LG is twisted 2LG (*t*2LG), where the two layers are rotated by a relative angle of θ_t (Fig. 29(a), inset). DF-TEM studies have demonstrated that polygonal domains in CVD-2LG evoke the orientation θ_t-dependent grain structure (Fig. 29(b)), where the DF-TEM image is a false color composite of the domains

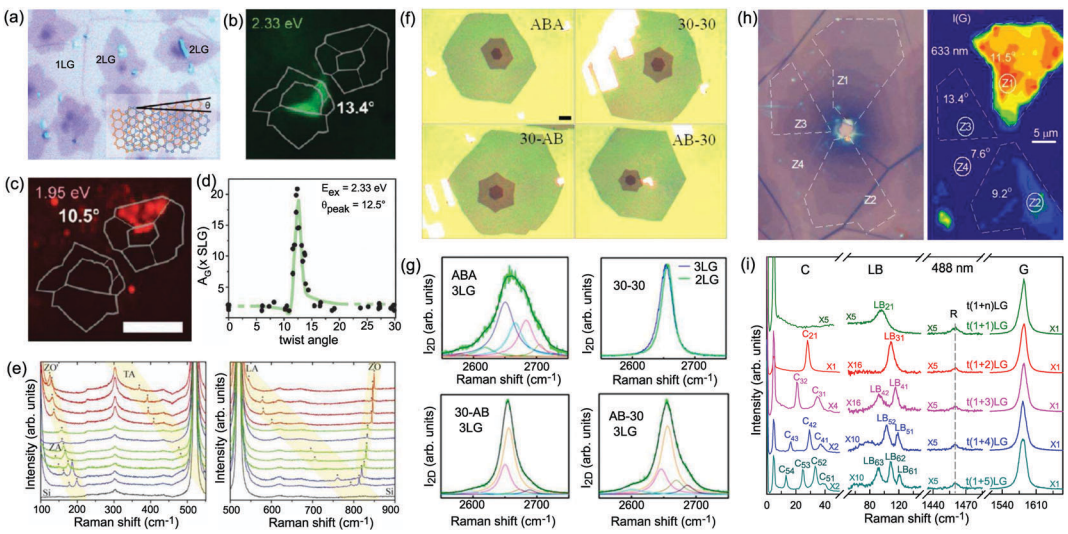

Fig. 29 (a) Optical image of CVD-*N*LG flakes. (b) Dark-field TEM of a *t*2LG, where θ_t is labeled for each domain in the TEM image. (c) G band Raman image of the same *t*2LG sample in (b). (d) A plot of G band integrated intensity *vs.* θ_t across many *t*2LG samples. Panels (a–d) are reproduced with permission from ref. 185. Copyright 2012, American Chemical Society. (e) Raman spectra of *t*2LG with different θ_t values. * Indicates the new Raman peaks observed in *t*2LG. Reproduced with permission from ref. 354. Copyright 2013, Tsinghua University Press and Springer-Verlag, Berlin, Heidelberg. (f) Optical micrographs of as-grown 3LG grains after transfer onto SiO_2 (90 nm)/Si substrates. Four different types of stacking arrangements are shown. Scale bar: 20 μm. (g) The 2D peaks in the trilayer regions correspond to four types of stacking arrangements in (f), respectively. Panels (f and g) are reproduced with permission from ref. 355. Copyright 2014, American Chemical Society. (h) Optical image of a CVD-MLG flake and the corresponding *I*(G) Raman image under 633 nm excitation. The zones with different *I*(G) are indicated by white dashed lines. (i) Raman spectra of different *t*NLG in a zone in (g) in the C, LB, R, and G spectral regions excited at 488 nm. The spectra are scaled and offset for clarity. Panels (h and i) were adapted with permission from ref. 202. Copyright 2016, Elsevier.

mapped individually by diffraction-filtered imaging.[185,186] I(G) images clearly demonstrate that the variations in Raman intensity are strongly correlated with θ_t; furthermore, I(G) is nearly constant within a domain (Fig. 29(c)). In particular, there is a strong enhancement of the G band integrated area (A_G) for a few specific domains, such as the 12.4° domain in Fig. 29(d).[185] This enhancement results from the singularity in the $JDOS_{OAT}$ of t2LG,[57] whose energy is exclusively a function of θ_t and whose optical transition strength is governed by interlayer interactions, as discussed in Section 4.3.

Besides the G mode, the so-called R and R′ modes have been observed at the low and high energy sides of the G mode.[172,173,354,360] The R and R′ band frequency is related to a Raman process that involves the scattering of a photo-excited electron by a phonon with wave vector q, and momentum conservation is achieved by the electron being elastically scattered by a superlattice wave vector $-q$ determined by θ_t.[354,360] The R and R′ modes come from the in-plane TO and LO phonon branches, and their frequencies are directly determined by θ_t. In principle, the phonons in other phonon branches can also be involved in such a Raman process and become Raman active. Indeed, several Raman modes can be observed in the range of 100–900 cm^{-1}, which can be assigned to the phonons of the ZO′, TA, LA, and ZO branches.[360] Because the q of the observed phonons in the 1LG BZ is determined by θ_t, phonons with wave vectors q in the interior of the BZ of 1LG can be spanned by changing the θ_t of t2LG.

Regular stacked NLG can also be grown by CVD. Mechanical exfoliation of graphite offers a simple way to obtain high-quality 3LG with ABA or ABC stacking. Crystallographically, 3LG can be viewed as two 2LGs with two separate stacking orientations, *i.e.*, top and bottom 2LG. Atmospheric pressure CVD-grown 3LG can form some special stacking configurations. If the angle θ_t between adjacent layers is used to denote the stacking orientation, ABA, 30–30, 30-AB, and AB-30 have been found to be major stacking orientations in the CVD-grown 3LG under specific growth conditions, and the optical micrographs of each stacking orientation are shown in Fig. 29(f). If we define the possible twist angle between bottom two layers as θ_{t1} and that between top two layers as θ_{t2}, the 30–30 stacking orientation can be denoted as t(1+1+1)LG with $\theta_{t1} = \theta_{t2} = 30°$, 30-AB as t(1+2)LG with $\theta_{t1} = 30°$, and AB-30 as t(2+1)LG with $\theta_{t2} = 30°$.

The profile of the 2D peak in ABA CVD-3LG (top left corner of Fig. 29(g)) is almost identical to that of natural AB-3LG prepared by exfoliation, which can be fitted by six Lorentzian peaks. The t(1+1+1)LG (30–30) and t(1+1)LG (30) show a linear band structure similar to 1LG, leading to the single Lorentzian peak of the 2D mode,[186] as shown in the top right corner of Fig. 29(g). The 30-AB and AB-30 3LG are the t(1+2)LGs with θ_{t1} or θ_{t2} of 30°. The band structure of t(n+m)LG can be considered as the overlapping of the band structure of the nLG and mLG constituents. Thus, the 2D mode profile of t(1+2)LG can be viewed as the superposition of the 2D mode profile of 1LG and AB-2LG. The 2D mode profile of AB-2LG can be fitted by four Lorentzian peaks, and that of 1LG shows a single Lorentzian peak. Therefore, the 2D mode profiles of 30-AB and AB-30 3LG can be fitted by five Lorentzian peaks, as shown in the lower panel of Fig. 29(g).

Once one twisted interface exists in NLG, the NLG is $t$$N$LG. In principle, there may exist up to $N - 1$ twisted interfaces in $t$$N$LG. CVD-grown NLG ($N > 1$) tends to be $t$$N$LG, which opens the possibility of studying various $t$$N$LG with different stacking sequences and twist angles. The stacking sequence of $t$$N$LG becomes more and more complicated with increasing N. When an additional layer is incorporated into a $t$$N$LG, AB-stacked or twisted interface can be formed relative to its adjacent layer. Continuing this trend, if $N > 2$, the number of stacking sequences of $t$$N$LG can reach $2^{N-1}-1$. For example, t3LG can be t(2+1)LG, t(1+2)LG, or t(1+1+1)LG. Adding one twisted interface can result in significant changes to its band structures and result in new singularities in the $JDOS_{OAT}$ of the twisted system. The number of twisted interfaces in $t$$N$LG can be probed by the corresponding R modes; for example, three R modes have been observed in CVD-t(1+1+1+1)LG.[205] Meanwhile, in comparison to CVD-1LG and CVD-t2LG, CVD-$t$$N$LG ($N > 2$) exhibits abundant spectral features in the ULF range, which are related to the interlayer vibration modes once the excitation energy matches the energies of the singularities in the $JDOS_{OAT}$ of the twisted system, and the enhanced C and LB modes can be resonantly observed.[57,71,202,205] The peculiar interlayer coupling in $t$$N$LG makes ω(C) sensitive to the number of layers of the constituents and ω(LB) to the total number of layers N.[57,71,202,205] This offers a convenient and reliable way to identify the stacking order of CVD-MLG by probing its C, LB, and R modes.[205]

Fig. 29(h) shows an optical image of a CVD-NLG flake (left panel), in which 1–6LG can be clearly identified, and an I(G) Raman image under 633 nm excitation (right panel).[202] The zones with different I(G) are indicated by white dashed lines and marked as Z1, Z2, Z3, and Z4, respectively. The images have the same scale. Fig. 29(i) shows typical Raman spectra of $t$$N$LG from $N = 2$ to $N = 6$ at the same zone in the ULF region.[202] Only one R mode with the same frequency is observed in this zone, indicating that all the NLGs ($N > 1$) in the same zone have only one twisted interface. This may indicate that all the NLGs share one twisted interface between the top two graphene layers according to the growth mechanism of CVD-MLG. The LB mode contributions in the $t$$N$LG originate from all graphene layers;[71] thus, we can determine N according to the observed ω(LB) and mark them as $t$$N$LG in the corresponding spectra in Fig. 29(i). Because the twisted interface would obstruct the interlayer shear coupling,[57,71] the C modes in $t$$N$LGs are localized in the AB-stacked constituents. With increasing total number of layers (N), it is found that the C modes in the $t$$N$LG ($N > 2$) always follow those of AB-(N−1)LG and all the (N−2) C modes are observed. This indicates that $t$$N$LG contains an AB-($N$−1)LG constituent. Therefore, the stacking sequence of the $t$$N$LG flakes is t(1+n)LG ($N = n + 1$). Moreover, t(1+n)LG in different zones exhibits similar spectral features (*e.g.*, the number and frequency of the C and LB modes) independent of θ_t. This offers a reliable way to identify the stacking orders (number of layers and stacking sequence) and interlayer coupling strength of CVD-MLGs, and one can determine whether a MLG sample

exhibits a fully non-stacked arrangement or if some of these layers are stacked in the AB-stacking with respect to the non-stacked layers.[205]

9.5 Graphene-based van der Waals heterostructures

Graphene-based vdWHs formed by vertically stacking other types of 2DMs (*e.g.*, TMDs) with graphene flakes have attracted significant interest.[28] The wide range of assemblies with 2DMs pave a way to modulate the fascinating physical properties with promising potential in nanoelectronics and optoelectronic devices. In these heterostructures, interfacial interactions between two atomic layers can dramatically influence the properties of the systems and induce remarkable phenomena that are absent in individual layers.[28,362–366] Normally, graphene and TMD flakes are two types of essential building blocks for vdWHs. Because graphene materials exhibit high mobilities, whereas TMD flakes have finite band gaps, TMD/graphene vdWHs have been used for various high-performance devices, such as field-effect tunneling transistors,[31] logic transistors, photovoltaics, and memory devices,[32–35,367] taking advantage of the properties of these two materials. In general, graphene flakes have been widely used as electrodes in vdWH-based devices to achieve higher performance because they have fewer defects compared with devices directly deposited on metal contacts.[31,35] An atomically sharp and non-damaged interface and a modified interfacial coupling are essential to the performance of TMD/graphene vdWHs. Therefore, it is very important to investigate the interfacial coupling in TMD/graphene vdWHs for their future application in high-performance devices.

Taking MoS_2 as an example, the graphene-MoS_2 vdWHs can be usually prepared by transferring one *m*-layer MoS_2 (*m*LM) flake onto an *n*LG or the *n*LG onto the *m*LM, denoted as *m*LM/*n*LG and *n*LG/*m*LM, respectively. Fig. 30(a) shows the optical images of 2L MoS_2(2LM)/2LG, and the corresponding atomic structure is represented in Fig. 30(b). In general, an annealing process is necessary after transfer to form good interfacial coupling because the two as-transferred 2DM flakes may not couple with each other. For MoS_2/graphene vdWHs, it is revealed that 30 min of annealing in an Ar atmosphere at 300° is the best condition to remove moisture and impurities. A slight redshift of E^1_{2g} and a blueshift of A_{1g} have been observed after annealing, originating from the multiple effects of doping, strain, and changes to the interface coupling.[36] Thus, it is difficult to evaluate the interface quality of *m*LM/*n*LG vdWHs by these high-frequency Raman modes. However, the C and LB modes, which are sensitive to the interlayer coupling, are a good choice to estimate the interface quality, as depicted by the ULF Raman signals of 2LM/*n*LG (n = 1, 2,..., 6, 8) in Fig. 30(c). Several LB branches can be detected in 2LM/*n*LGs, whose frequencies redshift with increasing n of *n*LG, as indicated by the dashed lines. This implies that the LB interfacial coupling between 2LM and *n*LG constituents is significant and both constituents contribute to the observed LB modes. Therefore, the vdWHs must be considered as an overall system with N ($N = n + 2$) layers to model the LB vibration in 2LM/*n*LG vdWHs, similar to the case of twisted multilayer graphenes.[71]

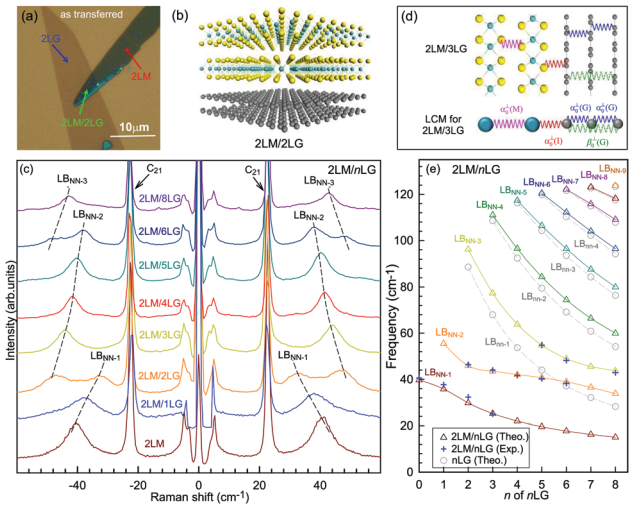

Fig. 30 (a) Optical image of 2LM/2LG vdWHs formed by transferring a 2LM flake on a 2LG flake. (b) Schematic illustration of 2LM/2LG vdWHs. (c) Stokes/anti-Stokes Raman spectra in the region of C and LB modes of pristine 2LM and 2LM/*n*LG vdWHs annealed for 30 min. The black dashed lines are eye guides. (d) Schematic diagram of an LCM for the LB modes in 2LM/3LG, in which the next nearest LB coupling in the 3LG constituents is considered. (e) Pos(LB) of *n*LG and 2LM/*n*LG as a function of n of *n*LG based on the LCM model. The crosses show the experimental Pos(LB) in 2LM/*n*LG. Reproduced with permission from ref. 36. Copyright 2017, American Chemical Society.

The LB modes can be analyzed by the LCM, in which each MoS_2 and graphene layer is treated as a ball with corresponding mass per unit area, as shown in Fig. 30(d) using 2LM/3LG as an example. There are $n + 1$ LB modes in 2LM/*n*LG. In the LCM of 2LM/*n*LG vdWHs, the previously determined LB force constants in MoS_2 and MLG are used,[71,151] that is, $\alpha_0^{\perp}(\mathrm{M}) = 84 \times 10^{18}$ N m^{-3}, $\alpha_0^{\perp}(\mathrm{G}) = 106.5 \times 10^{18}$ N m^{-3}, and $\beta_0^{\perp}(\mathrm{G}) = 9.5 \times 10^{18}$ N m^{-3} for the nearest LB force constants in MoS_2 and MLG flakes and the second nearest LB force constant of MLG flakes, respectively. If we denote the interfacial LB force constant between 2LM and *n*LG constituents as $\alpha_0^{\perp}(\mathrm{I})$, all the LB modes in different 2LM/*n*LG vdWHs (crosses in Fig. 30(e)) can be well reproduced with only one parameter, $\alpha_0^{\perp}(\mathrm{I}) = 60 \times 10^{18}$ N m^{-3}, as depicted by triangles and solid lines in Fig. 30(e). For comparison, the n-dependent Pos(LB) of the $(n-1)$ LB modes in *n*LG are also plotted in Fig. 30(e) as gray circles linked by gray dashed lines. The n-dependent Pos(LB) evolution of the LB modes in 2LM/*n*LG vdWHs are quite different from that in *n*LG, which clearly demonstrates how the interfacial LB coupling can modify the interlayer lattice dynamics of vdWHs from their constituents. Further investigation of *n*LG/*m*LM vdWHs has revealed that Pos(LB) in *n*LG/*m*LM are almost identical to those of *m*LM/*n*LG, which implies that the interface coupling in graphene–MoS_2 vdWHs is not sensitive to the stacking order or twist angles. Polarized Raman spectra show that one C mode was also observed in 2LM/*n*LG vdWHs. However, the observed Pos(C) of the 2LM/*n*LG vdWHs are almost identical to Pos(C_{21}) of pristine 2LM, which indicates the weak interfacial shear coupling between graphene and MoS_2 layers in the vdWHs, similar to the case in twisted multilayer graphene.[71]

In short, in comparison to the C modes, the LB modes can provide significant information about the interface quality and also the interlayer lattice dynamics of vdWHs, whereas the shear modes tend to localize in the constituents because of the much weaker shear coupling in the graphene-based vdWHs. Such ULF Raman studies on semimetal–semiconductor vdWH prototypes[36] can be extended to measure the interfacial interactions in various vdWHs[368] and would be beneficial to fundamentally understand their properties for further engineering of vdWH-based electronic and photonic devices.

9.6 Graphene oxide and reduced graphene oxide

Graphite oxide (GO) is a compound of carbon, oxygen, and hydrogen in variable ratios, obtained by treating graphite with strong oxidizers and subsequent exfoliation in water. GOs have a broad range of properties depending on the degree of oxidation and synthesis and have been recognized as promising precursors for the bulk production of graphene-based materials and devices.[12,371–373] However, there exist abundant oxygen-containing groups (*e.g.*, epoxy, hydroxyl, and carboxyl) on the GO sheet, which makes it insulating and significantly restricts its applications in electronics.[374] Reducing GO to produce reduced graphene oxide (rGO) has been used in the mass production of graphene. To date, significant research efforts have been dedicated to the reduction of GO, as evidenced by the vast body of related publications.[374–377] In the beginning, methods for GO reduction could be simply categorized into two types, one being chemical reduction and the other thermal treatments.[378–380] Later, laser annealing and electrochemical reduction were introduced to produce rGO.[381–383] The reduction of GO to rGO is a vital process because it has a significant impact on the quality of the rGO produced, and, thus, determines how similar rGO will be, in terms of structure, to pristine graphene. Raman spectroscopy has shown its ability to characterize GOs and rGOs.[67,370,384]

Under suitable conditions,[239,385,386] GO can undergo complete exfoliation in water, yielding colloidal suspensions of almost entirely individual graphene oxide sheets. Such sheets can be chemically functionalized, dispersed in polymer matrices, and deoxygenated to yield novel composites.[239] Moreover, GO sheets can be assembled into a paper-like material under a directional flow. Vacuum filtration of colloidal dispersions of graphene oxide sheets yielded, after drying, free-standing GO papers with thicknesses ranging from 1 to 30 μm, as shown in Fig. 31(a).[369] Scanning electron microscopy (SEM) images (see Fig. 31(b)) revealed well-packed layers through almost the entire cross-section of the paper samples. The peak in the X-ray diffraction (XRD) pattern of a typical GO paper specimen (see Fig. 31(c)) corresponds to a layer-to-layer distance (*d*-spacing) of about 0.83 nm, which is much larger than that of graphite because of the molecules between two adjacent GO sheets. Fig. 31(d) shows the micro-Raman spectra of a typical GO paper. The G peak and 2D peak are characteristic of sp^2 hybridized carbon–carbon bonds in graphene.[55,56] The strong and broad D band and high $I(D)/I(G)$ ratio in GO confirm its lattice distortions and a large amount of sp^3-like defects caused by the oxidation process. This is also confirmed by the blueshift of the G peak, which is overlapped by the redshifted D′ peak to form a single band at $\sim$1595 cm^{-1} because of the phonon quantum confinement effect induced by the small domain size in GO. The 2D band is more sensitive to the defects of graphene-based materials, as discussed in Section 5. The absence of the 2D band in GO also indicates that GO is dominated by the fully-disordered sp^2 bonding network.

There are a number of ways to create rGO from GO, although all methods are based on chemical, thermal, or electrochemical means. Some of these techniques are able to produce very high quality rGO, similar to pristine graphene, but can be complex or time consuming to carry out. Moon *et al.* reported a novel reducing agent system (hydroiodic acid with acetic acid

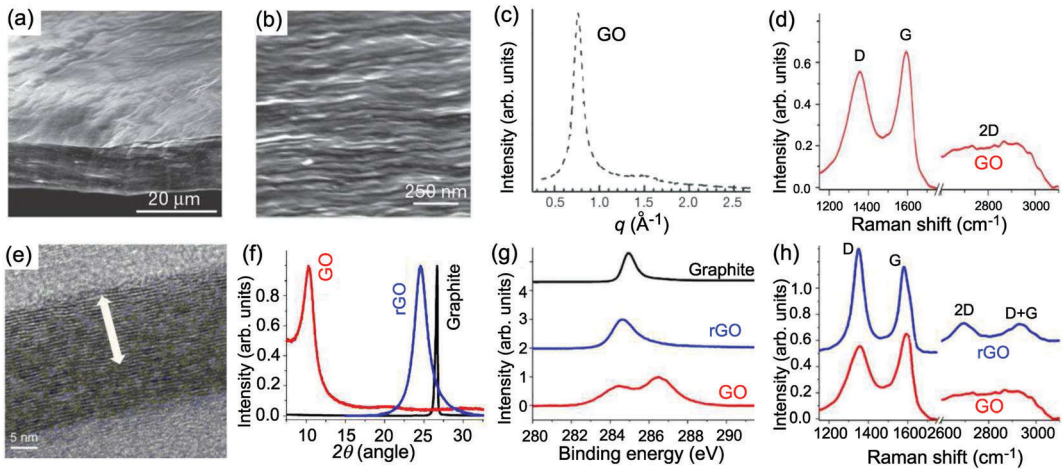

Fig. 31 (a) Low- and (b) high-resolution SEM side-view images of a 10 μm-thick GO paper. (c) X-ray diffraction pattern of the GO paper sample. Reproduced with permission from ref. 369. Copyright 2007, Nature Publishing Group. (d) Raman spectrum of a typical GO paper. (e) Cross-section TEM images of a stack of rGO platelets. (f) Powder XRD patterns of graphite, GO, and rGO. (g) XPS characterization of rGO platelets. (h) Raman spectra of rGO (blue) and the GO reference sample (red). Reproduced with permission from ref. 370. Copyright 2010, Nature Publishing Group.

(HI-AcOH)) that allows for the efficient, one-pot reduction of a solution-phased rGO powder.[370] The clusters in the powders are not fully restored into the hexagonal graphene framework, and the rGO platelets have inclusions containing aperiodically decorated functional groups. Furthermore, the graphitic laminar structure of stacks of rGO platelets could be resolved in the 'ordered' region. Fig. 31(e) shows a cross-section of one such stack, and the average interlayer distance of the stack is 3.64 Å. Fig. 31(f) shows powder XRD patterns of graphite, GO, and rRG. The 2θ angles of the XRD peaks (d-spacing) of rGO shifted from 10.27° (d-spacing $\sim$8.60 Å) of GO to 24.57° (d-spacing $\sim$3.62 Å) after reduction, which is similar to the SEM measurements. The XPS peaks of rGO at 285 eV in Fig. 31(g) assigned to C are one main C–C and four small C–O components.[387] The peak intensities and atomic ratios (O_{1s}/C_{1s}) of rGO in the C_{1s} peaks are decreased significantly in comparison with those of GO. Fig. 31(h) shows the Raman spectra of rGO and a GO reference. The G-band of rGO occurs at 1581 cm^{-1}, which corresponds to the recovery of the hexagonal network of carbon atoms with defects. The $I(D)/I(G)$ ratio of rGO increases notably, indicating that the reduction process may alter the structure of GO, resulting in a high number of structural defects. However, if we note the G peak at 1581 cm^{-1} and the appearance of the D′ peak, the defect status of rGO should be at stage 1 while that of GO should be at stage 2. Therefore, the higher $I(D)/I(G)$ ratio of rGO actually indicates fewer defects with respect to GO after the reduction process. The 2D peak ($\sim$2680 cm^{-1}) becomes significant in rGO and the D + G band is present at $\sim$2910 cm^{-1}, demonstrating the restoration of graphite structures. Analogously, by combining the XPS and Raman spectra, rGO produced by other methods can also be analyzed.[67,382]

9.7 Graphene–polymer composites

Because of the excellent mechanical, thermal, and electrical properties, graphene–polymer composites are expected to have a variety of applications in the automotive, aerospace, construction, and electronics industries.[226,388–390] A classic example of such a system is the birefringence measurements made on poly(methyl methacrylate) (PMMA) and polystyrene (PS) structures. There are already commercially available photoelasticity-based sensors, such as the Photostress gray-field polariscope from Stress Photonics.

Raman spectroscopy is the ideal tool to probe the status of graphene in this system.[226] The exfoliated and CVD-grown graphene composite coatings are prepared by the dry-transfer method. Fig. 32(a) shows a schematic of the sample preparation. The *in situ* Raman measurements were carried out on the graphene and the graphene/polymer composite coating. Well-defined Raman spectra with a characteristic 2D band (around 2640 cm^{-1}) and G band (around 1580 cm^{-1}) are obtained from both the exfoliated and CVD-grown graphene. The top panel of Fig. 32(b) shows the example flakes found in the composite system with increasing number of layers, where the $I(2D)/I(G)$ is greater than three for monolayer graphene. The absence of the D band for the exfoliated graphene reveals its high-quality.[44] The bottom panel of Fig. 32(b) shows the

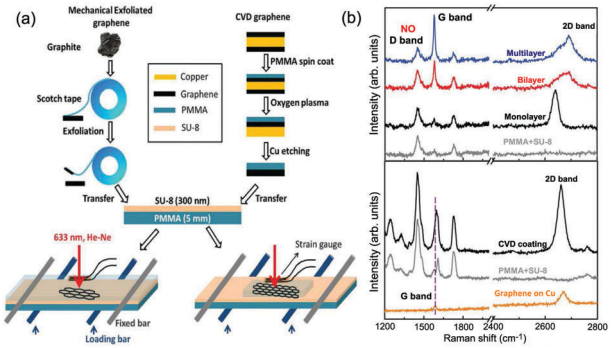

Fig. 32 (a) A schematic representation of the preparation of model composite coatings. (b) Top: Raman spectra of different layers of graphene in exfoliated composite coatings. Absence of the D band at $\sim$1350 cm^{-1} indicates the high crystallinity of the sample. Bottom: Raman spectra of the as produced CVD-grown graphene on Cu foil and in the composite coating. The spectra from poly(methyl methacrylate) (PMMA) top coat and SU-8 is shown as a reference in both cases. Spectra are offset for clarity. Reproduced with permission from ref. 226. Copyright 2014, Wiley Online Library.

Raman spectra of as-grown CVD graphene on Cu foil and in the coatings. $I(2D)/I(G)$ is greater than 2 and the FWHM of 2D mode $\sim$25 cm^{-1}. The G peak of different graphene layers in exfoliated composite coatings does not change with increasing number of layers and $\omega(G)$ is close to that of intrinsic 1LG, while $\omega(G)$ in CVD-graphene composite coatings blueshifts about $\sim$20 cm^{-1} from the CVD-graphene on the copper foil. This difference is due to the strain induced in the transfer process. The dry-transfer mechanically exfoliated sample has no residual stresses, whereas the CVD sample is in compression following the solvent evaporation during its transfer.[226]

10 Applications of Raman spectroscopy in graphene-based devices

When graphene materials are incorporated into some functional devices, their intrinsic properties are modified by the environment and even the device itself. During device fabrication, the graphene materials undergo several processes. For example, to realize the specific functions of the device, graphene materials might be decorated with functional groups or be in a certain state so that their peculiar properties can be used. In all cases, on-line, real-time, and nondestructive characterization techniques are crucial for the monitoring of the properties (and their modification) of graphene materials during the fabrication process and to probe the functions of graphene materials in the device. Some conventional methods show limitations concerning characterization, especially as device dimensions continue to shrink. Raman spectroscopy is a powerful scientific tool that allows researchers to identify important physical and chemical parameters of graphene materials in devices, such as number of layers, chemical identity, stacking geometry, doped charge, defects, contaminants, edge chirality, strain, stability,

chemically attached functional groups, and energy gaps. For 1LG and MLG, which are only angstrom-scale in the *z*-direction, the electronic band structure of graphene is easily modified by changing any of the above mentioned physical and chemical parameters. In the following subsections, we show the advantages and efficiencies of Raman spectroscopy in effectively characterizing some typical graphene-based devices, which is expected to be an important examination tool in the industrialization of graphene applications in the future.

10.1 Graphene-based field-effect transistors

The graphene FET is a device with source and drain electrodes, and the Si/SiO_2 substrate can be adopted as a back gate.[24,60,63] A graphene FET is not only the basic device of analog and digital circuits[391] but also the basic structure of other devices, *e.g.*, photodetectors[392,393] and sensors.[394,395] One of the most important variables in a graphene FET is its doping level, which can be identified by Raman spectroscopy, as discussed above.[60,61,63] Another important issue concerning graphene FETs is the heat generation and dissipation when a large current drive is necessary to address several other FETs or when high switching speeds for radio frequency applications are desired.[307,396] The dissipated electric power can increase the operating temperature of the device so that thermal management of the device becomes critical. Therefore, it is important to understand the heat generation and dissipation in the graphene FET.

Freitag *et al.* fabricated a graphene FET[307] whose SEM image is shown in Fig. 33(a) as an inset. The graphene FET is 2.65 μm long and 1.45 μm wide. The SiO_2 gate oxide thickness is 300 nm. The FET can support electrical power densities up to at least 210 kW cm^{-2}. Fig. 33(a) shows the 2D-band of the graphene FET while a current flows through it. ω(2D) decreases sharply with increasing electric power and the peak broadens. As Fig. 33(b) shows, the decrease in energy is proportional to the dissipated electric power, which suggests that Joule heating is responsible for the phonon softening. It is known that ω(2D) decreases linearly with temperature.[304] Using the proportionality factor of -29.4 K cm^{-1},[304] one can calibrate a temperature scale for the electronic measurements and, thus, it was shown that the center of the graphene FET heats up at a rate of 3.3 K kW^{-1} cm^{-2}. At the highest power density, 210 kW cm^{-2}, the graphene 2D-derived temperature reaches 1050 K. The intensity mapping of ω(2D) can give the temperature distribution in the graphene.[307] As shown in Fig. 33(c), ω(2D) in the graphene FET shows a unified distribution in the absence of an applied voltage. When a voltage is applied, because of the different energy dissipation pathways, the center of the FET has a higher temperature than the edges. The temperature distribution in the graphene FET at different electrical powers is shown in Fig. 33(d). The yellow bars are the electrodes. The temperature distribution can be explained by a model that considers the thermal resistance between the graphene and electron and also the thermal resistance between the graphene and SiO_2 substrate, as shown in Fig. 33(e). The simulation shows that the lateral heat flow in the thin graphene sheet is five times larger than the lateral flow in SiO_2 (despite being 1000 times thinner than the SiO_2 film).[307] This helps spread the hot spot in the graphene sheet, which would otherwise be even hotter in the middle, and it also spreads some of the heat power to the contacts. Nevertheless, 77% of the power is dissipated through the SiO_2 directly below the FET, while the remaining 23% is dissipated through the contacts and the neighboring sites. Thus, the main heat dissipation channel is the silicon under the graphene FET, as shown in Fig. 33(f).

Notably, the doping level changes slightly with a drain voltage but without a gate voltage.[307] At low doping, ω(2D) depends simply on the temperature.[60] ω(G) is sensitive to both doping level and temperature change.[60,304] Thus, ω(G) cannot be used to identify the thermal distribution in a graphene FET under a drain voltage.

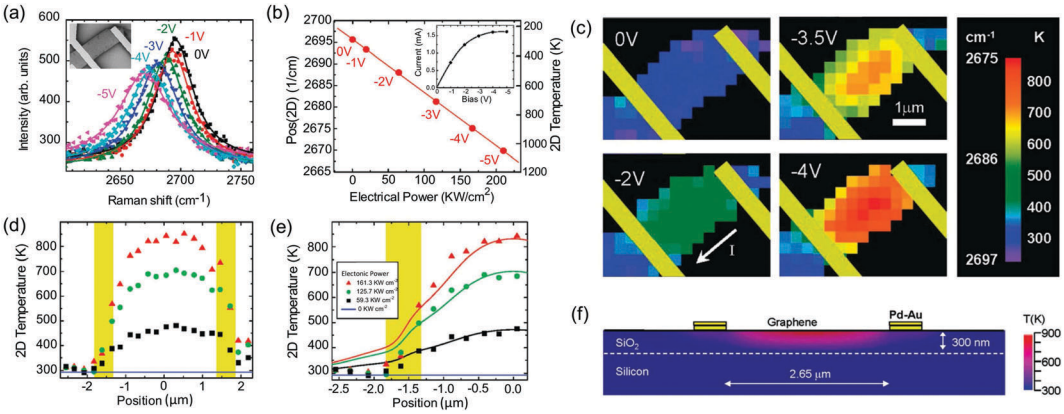

Fig. 33 (a) The 2D band spectra measured in the middle of the FET device at various drain voltages. The gate voltage is 0 V, ε_L = 2.41 eV. Inset: SEM image of the device. (b) ω(2D) and temperature as a function of applied electrical power. Inset: Corresponding *I*–*V* curve. (c) Spatially resolved images of ω(2D) at four different drain voltages. The graphene flake extends beyond the left and right contacts (indicated in yellow). (d) Experimental temperature along the graphene sheet (parallel to the current flow) at 59.3 (black), 125.7 (green), and 161.3 kW cm^{-2} (red) dissipated electronic power. The blue line corresponds to the zero-power case, defined as room temperature. Electrodes are depicted in yellow. (e) The corresponding modeled temperature profile along the graphene device for the same bias conditions. (f) Cross section of the temperature distribution in the gate stack for 161.3 kW cm^{-2} of dissipated electronic power. Reproduced with permission from ref. 307. Copyright 2009, American Chemical Society.

The above result shows the ability of Raman spectroscopy to probe the *in situ* temperature of graphene in electronic devices. This technique can be extended to other graphene-based FETs, such as the graphene/BN FET.[397]

10.2 Graphene-based energy storage devices

Technologies for efficient energy storage are urgently required because of environmental pollution, limited fossil resources, and the huge demand for energy. Therefore, interest in energy storage devices, such as ion batteries and electrochemical capacitors (ECs), has increased enormously.[399,400] The main reactions of ion batteries are reversible ion intercalation/de-intercalation cycles between two layered compounds, corresponding to the charge–discharge process, with electrochemical reactions.[401] For ECs, the interface between the electrodes and electrolyte can be treated as a capacitor.[400] According to the electrochemical activity or inactivity of electrode materials, the ECs are divided into electric double-layer capacitors (EDLCs) and pseudocapacitors, respectively. Thus, the electrode material is important for energy storage. The 2DMs, such as TMDs,[402] MXenes,[403] and graphene-based materials,[27,404] have many fantastic properties, *e.g.*, high surface area and possible redox reactions, and are widely used as electrodes in ion batteries and ECs. *In situ* spectroelectrochemical measurements can be used to characterize electrode materials during ion (lithium,[405] sodium,[406] and potassium[398]) battery or EC processes.[382,405,407] Here, we take potassium ion (K-ion) batteries with *N*LG electrodes as an example to show how Raman spectroscopy can help us to understand the mechanisms of energy storage and the distortion of the electrode material in the charge–discharge process of energy storage devices.[398]

To ensure equilibrium conditions between subsequent Raman scans, an extremely slow scan rate (0.05 mV s^{-1}) is used in the linear sweep voltammetry (LSV) measurements. Selective Raman spectra are shown in Fig. 34(a) for different states of charge. Fig. 34(b) displays all Raman spectra taken from 0.37 to 0.01 V in a waterfall plot. The top of Fig. 34(c) shows the LSV measured during the *in situ* Raman experiment. The G peak positions and intensities are shown in the bottom and middle of Fig. 34(c), respectively. Together these plots help visualize and quantify the distinct peak shifts and intensity changes of the Raman spectra. Notably, the D peak ($\sim$1330 cm^{-1}) was not observed throughout the *in situ* measurements, indicating that no significant degradation of the sp^2 hybridized carbon in the *N*LG takes place.[398,406] An initial scan taken at 2.0 V reveals a similar spectrum to that of *N*LG, containing 2D and G peaks with the G peak at 1582 cm^{-1}. At 0.37 V, the G peak blue shifts to 1589 cm^{-1} because of the formation of a low-defect-concentration stage GIC. From 0.37 to 0.25 V, minimal changes are observed in both the electrochemical and Raman data, which are attributed to the sparse ion composition of the low-defect-concentration stage compound. Near 0.24 V, the first reduction peak occurs in the LSV as ordered staging begins, indicated by a higher frequency shoulder in the G peak and a decrease in the 2D intensity. Initially, the charge is equally distributed between all layers, and only a single uncharged G peak (G_{uc}) is present.

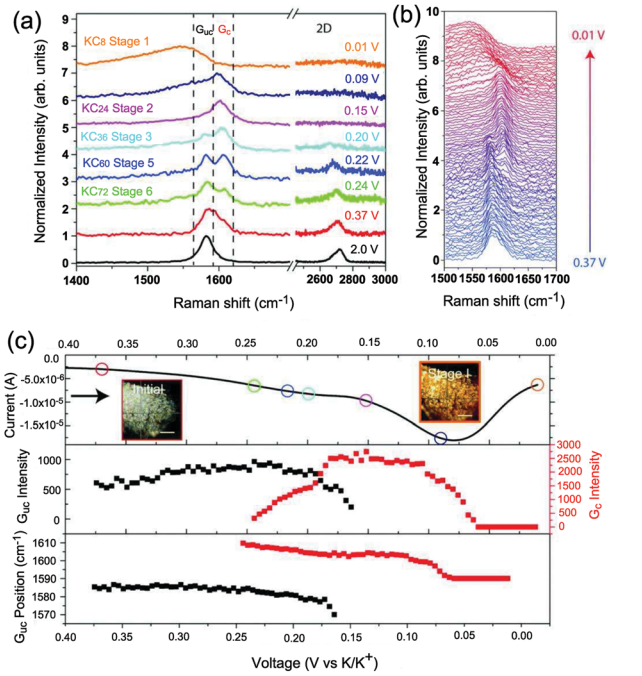

Fig. 34 (a) Selective Raman spectra taken at different states of charge, as indicated in the linear sweep voltammograms. (b) Waterfall plot of all Raman spectra taken between 0.37 and 0.01 V. (c) Top, LSV measured during the *in situ* Raman experiment. The colored circles indicate the state of charge for the Raman spectra in (a). Middle: Peak intensities for the G_{uc} and G_c peaks. Bottom: Peak positions for the G_{uc} and G_c peaks. Inset: Optical microscope image of the *N*LG coated foam initially and fully potassiated. Scale bar: 20 μm. Reproduced with permission from ref. 398. Copyright 2016, Royal Society of Chemistry.

When cations start to intercalate into graphite, the charge density increases on layers adjacent to the intercalants, forming an upshifted G_c (G charged) peak.[146,406,407] The graphene layers not adjacent to the ions continue to show the G_{uc} peak leading to a doublet in the Raman spectra at stages above stage 2.[408,409] At 0.24 V, the G_c/G_{uc} intensity ratio is indicative of stage 6 KC_{72}.[410] From 0.24 to 0.15 V, the G_c peak increases in intensity, the G_{uc} and 2D peaks decrease, and all peaks red shift. The opposite behavior of the G_c and G_{uc} intensities is due to continued staging where more graphene layers become charged and fewer uncharged layers remain. Both the G_{uc} peak and 2D peak have vanished by 0.15 V. This is because stage 2 no longer involves any uncharged graphene layers, correlating with the disappearance of the G_{uc} peak because of the emergence of a stage 2 compound. At this stage, the doping level ($|E_F|$, E_F is the Fermi level) is sufficiently high to invalidate the transitions of the DR process for the 2D peak.[58,60,61] From 0.15 to 0.01 V, the Raman spectra evolve from a symmetrical G peak to an asymmetric Fano resonance shape because of interference between the metallic like behavior of stage 1 GICs.[410] Optical microscope images of the *N*LG at an open circuit voltage of 0.01 V also support the formation of stage 1 KC_8, as shown by the change in color from gray to bright orange (inset of Fig. 34(c)).

The above results demonstrate that Raman spectroscopy is useful in electrode material preparation and redox reactions, as

well as to increase the cycle life of energy storage devices. This method can be extended to identify ion batteries and ECs containing other 2D materials as electrodes.[411]

10.3 Graphene-based solar cells and organic light emitting diodes

Having unique properties, *i.e.*, high optical transparence, high electrical conduction, and excellent mechanical flexibility, graphene and its derivatives have been investigated extensively in the field of solar cells and organic light emitting diodes (OLEDs). Many impressive results have been reported, where graphene-based materials (GO film and CVD-grown graphene) have been used as the electrodes, *i.e.*, transparent anodes,[357,413,414] non-transparent anodes,[415] transparent cathodes,[416] and catalytic counter electrodes,[417] as well as where graphene has been used as the active layer, *i.e.*, light harvesting materials,[418] Schottky junctions,[419] electron transport layers,[420] hole transport layers, both hole and electron transport layers,[421] and interfacial layers in the tandem configuration.[422]

Usually, CVD-grown graphene has a higher electrical conductivity than the GO film because of the higher crystal quality. Here, we present an example of the layer-by-layer (LBL) transferred CVD-grown graphene as the solar cell anode,[412] as shown in Fig. 35(a). A single layer of graphene does not have sufficiently high sheet conductivity. Stacking multilayer graphene together, followed by doping, is required to achieve higher extrinsic conductivity. A direct LBL interface coupling route for fabricating multilayer graphene films is shown in Fig. 35(b). In this LBL stacked graphene, the overall electrical conductivity is determined by the crystal quality and also the interlayer coupling. Raman spectroscopy is an ideal tool to identify the interlayer coupling and also the number of layers in this LBL transferred system.

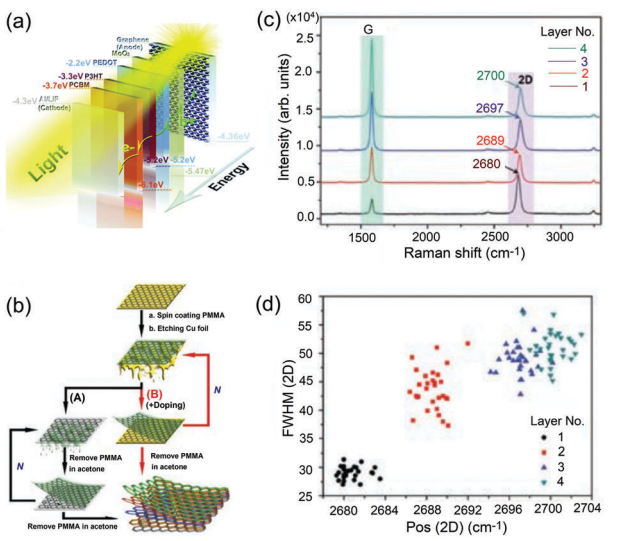

Fig. 35 (a) Schematic diagram of a photovoltaic (solar cell) device structure. (b) Schematic drawing of *N*LG films made by normal wet transfer (A) and direct coupling LBL assembly (B) (N = 0, 1, 2, 3...). (c) Raman spectra of graphene films with 1 to 4 layers. (d) A statistical result of FWHM(2D) and peak Pos(2D) from 1 to 4 layers. Reproduced with permission from ref. 412. Copyright 2011, Wiley Online Library.

As shown in Fig. 35(c), I(G) increases with the number of layers because of the increased signal from the graphene flake. In the AB- and ABC-stacked *N*LG, the interlayer coupling affects the electronic band and results in a complicated 2D band profile. Here, the LBL transferred graphene is the *tN*LG with randomly stacked orientations at each interface, denoted as complete *tN*LG. This complete *tN*LG has a linear electronic band dispersion similar to 1LG.[182] Thus, the 2D band of the complete *tN*LG also shows a single Lorentzian peak. However, the Fermi velocity of the *tN*LG is reduced because of the interlayer coupling. The lower Fermi velocity would lead to the blueshift of the 2D peak, as shown in Fig. 35(c and d). Moreover, the FWHM of the 2D peak in the complete *tN*LG would be broadened with respect to the number of layers. Therefore, according to the behavior of the 2D peak, the interlayer coupling and the number of layers of the LBL transferred graphene can be identified.

Graphene can also be adopted as the electrode of an OLED.[423] In these OLEDs, the transparent conducting top electrode can be formed of a large-area multilayer graphene/bonding layer/polyethylene terephthalate structure. In this structure, the strain is induced in the *N*LG. As a means of probing the uniaxial strain on the *N*LG, polarized Raman spectroscopy is usually performed.[423] The splitting of the G mode (denoted as the G^+ and G^- bands) can be observed under uniaxial strain. The upshift and downshift of the G mode indicate compression and tension, respectively. The local stress can be estimated from the expression, $\Delta\omega = \omega_{G_0} - \omega_{G^\pm} = -\omega_{G_0}\gamma\varepsilon$, where ω_{G_0} is the G-band peak of unstrained graphene, $\gamma = 2$ is the Grüneisen parameter of G mode,[87,424] and ε is the stress.

10.4 Graphene-based nanoelectromechanical systems

The outstanding mechanical,[273] electrical,[1,426] and optical[427] properties of graphene make it an ideal material for flexible, conductive, and semitransparent films. Multilayer graphene with several tens of graphene layers is sufficiently stiff[428] to produce freestanding cantilevers with very high aspect ratios that can be used to make suspended mirrors with masses from tens to hundreds of femtograms. Moreover, the optical cavities formed by suspending the cantilevers over a silica surface can be electrostatically actuated, making them well suited for the development of nanoelectromechanical systems (NEMS).[429] NEMS can be operated as ultrasensitive mass sensors[430,431] and ultrahigh-frequency resonators[432] and can also be used to explore fundamental physical phenomena such as nonlinear damping[273] and quantum effects in macroscopic objects.[433] Various dissipation mechanisms are known to limit the mechanical quality factors of NEMS and to induce aging because of material degradation; thus, there is a need for methods that can probe the motion of these systems and the stresses within them at the nanoscale.[425] Raman spectroscopy has been used to probe the local stress within such a multilayer graphene cantilever.[425]

Fig. 36(a) depicts a NEMS prepared from micrometer-sized multilayer graphene planar flakes, which are clamped on one side by a gold film with overhanging silicon oxide. The typical samples have a thickness of 100 graphene layers (30 nm) to

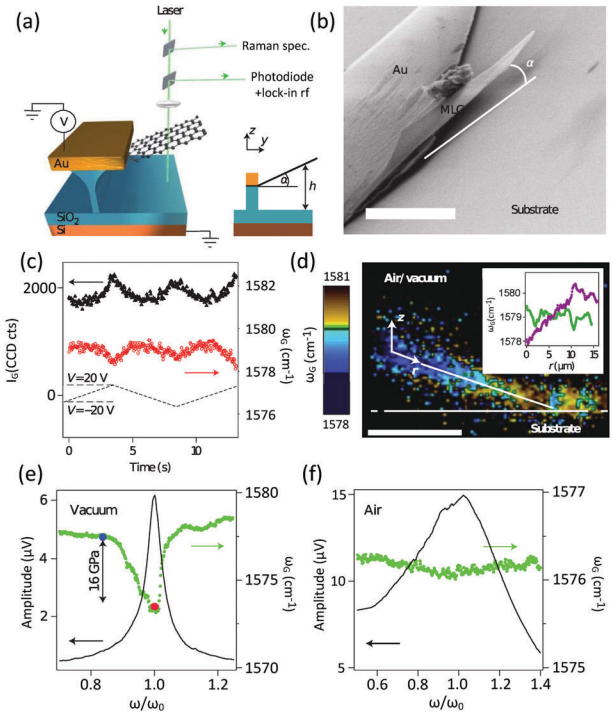

Fig. 36 (a) Schematic view of a nanoelectromechanical device. The cantilever can be actuated with an external voltage while its optical properties are analyzed with a high-sensitivity Raman spectrometer and a fast photodiode. (b) SEM images showing a typical multilayer graphene cantilever clamped to a gold film on an oxidized silicon substrate. (c) The intensity I_G (black symbols, left axis) and shift ω_G (red symbols, right axis) of the Raman G peak of a multilayer graphene cantilever *vs.* time during electrostatic actuation (dashed line). Peak softening can be seen. (d) False color plot showing the value of ω_G measured during a confocal (x, z) scan of the cantilever cross-section. The inset shows how ω_G varies along the cantilever before (purple) and after (green) the collapse of the cantilever onto the silica substrate. Black marks indicate the hinge position. Scale bar: 5 μm. (e and f) Amplitude of cantilever oscillations (black line: left axis) and Raman shift (green symbols: right axis) *vs.* drive frequency in a vacuum (e) and in air (f). Reproduced with permission from ref. 425. Copyright 2012, Nature Publishing Group.

prevent collapse, as shown in Fig. 36(b). ω(G) (or ω_G) of the graphene flake follows a quadratic dependence with small voltage variations. The G peak shift is indeed synchronized with the interferometric response intensity of G mode, as shown in Fig. 36(c), and exhibits softening of 1.9 cm^{-1} at the maximum cantilever deflection. This peak softening is interpreted as a stress/strain effect and, by analogy with measurements of strained graphene,[87,434,435] one can extract a corresponding strain value of 0.06% at the maximum deviation resulting from a quasi-static stress of 600 MPa.

The Raman signature of graphene flakes in NEMS depends on the position along the flake, which reflects the stress distribution in the cantilever. A micro-Raman confocal depth scan (x, z) (Fig. 36(d)) reveals a linear increase of ω(G) along the cantilever axis, from the free end of the cantilever to the hinge. This is not observed when the multilayer graphene is collapsed (Fig. 36(d), inset). This linear shift could be interpreted as a continuously increasing electrostatic field effect[60,64] owing to charge within the substrate, which also influences ω(G).[296] In Fig. 36(e and f), the fundamental mechanical resonance of this multilayer graphene cantilever is detected using the Raman signal under different experimental conditions. A large softening behavior (green curve, ~6 cm^{-1}) is observed when mechanical excitation coincides with the mechanical resonance width, which is in agreement with Fizeau interferometry measurements (black curve). In contrast to the vacuum case (Fig. 36(e), the quality factor Q_{vac} ~ 26.1), the same sample in air (Fig. 36(f)) presents a reduced quality factor (Q_{air} ~ 2.3), as well as a reduced Raman G-peak softening, which illustrates that the dynamical stress in air is less intense. The value of Q_{air} agrees with a typical viscous damping model[436] for this particular geometry and represents the predominant damping mechanism limiting the quality factor in air. However, this mechanism is no longer dominant under vacuum, where dissipation may be governed by clamping losses.

10.5 Graphene-based vdW two-dimensional heterostructure devices

Recently, vdW heterostructures formed by vertically stacked various 2DMs, such as graphene and TMDs, have offered more promising properties and functionalities for many electronic and optoelectronic applications than the constituent materials.[367,438–443] Fig. 37(a–c) show a cross-sectional view, optical microscope image, and topographical sketch of a representative graphene-coated MoS_2 (graphene/MoS_2 heterostructure),[437] respectively. Charge transfer between graphene and TMDs in the graphene/TMD heterostructures occurs, forming a Schottky junction.[437]

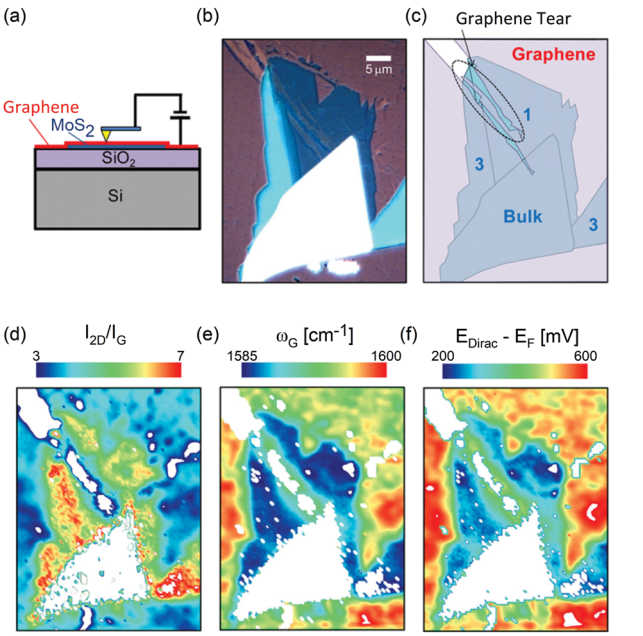

Fig. 37 (a) Schematic diagram of a graphene/MoS_2 system. Optical microscope image (b) and topographical diagram (c) of a CVD grown graphene single crystal on MoS_2. Spatial Raman maps for I(2D)/I(G) (d), ω_G (e), and the calculated $E_{Dirac} - E_F$ (f) for the graphene/MoS_2 heterostructure. Reproduced with permission from ref. 437. Copyright 2014, American Chemical Society.

A technique is necessary to *in situ* probe the charge transfer within the heterostructures. The doping carrier density (n) and the Fermi level relative to the Dirac point ($E_{Dirac} - E_F$) of graphene can be calculated based on ω(G) and ω(2D).[60,61] In particular, ω(G) upshifts monotonically upon increasing the doping level for p and moderate n doping in graphene, while ω(2D) upshifts in the case of p-doping ($E_F < E_{Dirac}$) and downshifts in the case of n-doping ($E_F > E_{Dirac}$).[60] Therefore, following the discussion in Section 7.1, the doping level and the carrier density (n_e or n_h) of graphene can be easily quantified by the spectral parameters of Raman spectroscopy. The spectral parameters of graphene are more sensitive to its doping level than those of TMDs; thus, the charge transfer between graphene and MoS_2 in the heterostructures can be determined by the spectral features of the graphene constituent.

Fig. 37(d–f) show the spatial Raman maps of I(2D)/I(G), ω_G, and the calculated $E_{Dirac} - E_F$ of the graphene constituent in the heterostructures, respectively. According to eqn (15), I(2D)/I(G) under 514 nm excitation can be used to identify the doping level of graphene. The average positions of the G and 2D peaks for the graphene on SiO_2 (ω_G = 1593 cm^{-1} and ω_{2D} = 2648 cm^{-1}), as well as their intensity ratio (I(2D)/I(G) = 4), indicate that graphene is heavily p-doped with a carrier density n = –2 × 10^{13} cm^{-2} and $E_F - E_{Dirac}$ = −550 mV. On the other hand, the corresponding parameters for graphene in contact with MoS_2 ($\omega_G \sim$ 1586 cm^{-1}, ω_{2D} = 2644 cm^{-1}, and I(2D)/I(G) = 6) suggest that graphene is p-doped with $n = -1 \times 10^{13}$ cm^{-2} and $E_F - E_{Dirac}$ = −250 mV. This suggests that additional electrons are transferred from MoS_2 to graphene so that graphene is 'counter doped' by the underlying MoS_2 flake or, in other words, MoS_2 is hole doped by graphene.

11 Conclusions

Graphene has extraordinary electronic, optoelectronic, and mechanical properties, and a variety of device applications. We have reviewed the origin of all Raman modes in intrinsic graphene, including the first-order G mode and DR-activated first-order and second-order Raman modes. The C, LB, and 2D modes in *N*LGs have also been discussed in detail, which are significantly sensitive to the number of layers N and stacking order (AB, ABC, and twist stacking). The resonance Raman spectroscopy of *N*LG has also been presented. The external perturbations to graphene flakes could affect their lattice vibrations and also band structures, which can be revealed by Raman spectroscopy. The effects of point defects, line defects, and edges on the D, G, and 2D modes have been discussed in detail, and it has been clearly demonstrated how to probe the nature of defects in graphene by Raman spectroscopy. The Raman spectral features, such as the lineshape and peak positions of the C, LB, and 2D modes, the intensity of the G mode of *N*LG, and that of the Si mode of the substrate, have been utilized to identify the value of N of graphene flakes. Raman spectroscopy has also been applied to characterize graphene-based materials, such as nanographene, carbon dots, graphene oxide, epitaxial graphene on SiC, *N*LG grown by CVD, and graphene-based van der Waals heterostructures. Raman imaging has also been shown to provide spatially distributed information concerning the number of layers, stacking order, edges, strain, and growth mechanism of graphene flakes. Finally, Raman spectroscopy has been shown to be an on-line, real-time, and nondestructive characterization technique to monitor the property modification or designed function on demand of graphene materials in related devices, such as FETs, energy storage devices, solar cells, OLEDs, NEMS, and graphene-based vdW heterostructures. We hope that this review will be an essential guide to the Raman spectroscopy of graphene-based materials for scientists in the field of material synthesis, basic research, and device and industrial applications.

Conflicts of interest

There are no conflicts to declare.

Acknowledgements

We acknowledge support from the National Key Research and Development Program of China (Grant No. 2016YFA0301204), the National Natural Science Foundation of China (Grant No. 11474277 and 11434010), the Key Research Program of the Chinese Academy of Sciences (Grant No. XDPB06-02, XDPB08-2), and Beijing Municipal Science and Technology Commission.

References

1 K. S. Novoselov, A. K. Geim, S. V. Morozov, D. Jiang, Y. Zhang, S. V. Dubonos, I. V. Grigorieva and A. A. Firsov, *Science*, 2004, **306**, 666–669.
2 T. Ohta, A. Bostwick, J. L. McChesney, T. Seyller, K. Horn and E. Rotenberg, *Phys. Rev. Lett.*, 2007, **98**, 206802.
3 K. F. Mak, J. Shan and T. F. Heinz, *Phys. Rev. Lett.*, 2010, **104**, 176404.
4 J. H. Warner, M. Mukai and A. I. Kirkland, *ACS Nano*, 2012, **6**, 5680–5686.
5 C. H. Lui, Z. Li, Z. Chen, P. V. Klimov, L. E. Brus and T. F. Heinz, *Nano Lett.*, 2010, **11**, 164–169.
6 C. Cong, T. Yu, K. Sato, J. Shang, R. Saito, G. F. Dresselhaus and M. S. Dresselhaus, *ACS Nano*, 2011, **5**, 8760–8768.
7 X. Li, W. Cai, J. An, S. Kim, J. Nah, D. Yang, R. Piner, A. Velamakanni, I. Jung and E. Tutuc, *et al.*, *Science*, 2009, **324**, 1312–1314.
8 A. Reina, X. Jia, J. Ho, D. Nezich, H. Son, V. Bulovic, M. S. Dresselhaus and J. Kong, *Nano Lett.*, 2008, **9**, 30–35.
9 C. Virojanadara, M. Syväjarvi, R. Yakimova, L. Johansson, A. Zakharov and T. Balasubramanian, *Phys. Rev. B: Condens. Matter Mater. Phys.*, 2008, **78**, 245403.
10 M. Sprinkle, M. Ruan, Y. Hu, J. Hankinson, M. Rubio-Roy, B. Zhang, X. Wu, C. Berger and W. A. De Heer, *Nat. Nanotechnol.*, 2010, **5**, 727–731.

11 H. A. Becerril, J. Mao, Z. Liu, R. M. Stoltenberg, Z. Bao and Y. Chen, *ACS Nano*, 2008, **2**, 463–470.
12 G. Eda, G. Fanchini and M. Chhowalla, *Nat. Nanotechnol.*, 2008, **3**, 270–274.
13 D. R. Dreyer, S. Park, C. W. Bielawski and R. S. Ruoff, *Chem. Soc. Rev.*, 2010, **39**, 228–240.
14 A. Hashimoto, K. Suenaga, A. Gloter, K. Urita and S. Iijima, *Nature*, 2004, **430**, 870–873.
15 M. M. Lucchese, F. Stavale, E. M. Ferreira, C. Vilani, M. Moutinho, R. B. Capaz, C. Achete and A. Jorio, *Carbon*, 2010, **48**, 1592–1597.
16 L. G. Cançado, A. Jorio, E. M. Ferreira, F. Stavale, C. Achete, R. Capaz, M. Moutinho, A. Lombardo, T. Kulmala and A. Ferrari, *Nano Lett.*, 2011, **11**, 3190–3196.
17 G. Lu, L. E. Ocola and J. Chen, *Nanotechnology*, 2009, **20**, 445502.
18 Z.-S. Wu, G. Zhou, L.-C. Yin, W. Ren, F. Li and H.-M. Cheng, *Nano Energy*, 2012, **1**, 107–131.
19 X. Jia, J. Campos-Delgado, M. Terrones, V. Meunier and M. S. Dresselhaus, *Nanoscale*, 2011, **3**, 86–95.
20 R. Yang, Z. Shi, L. Zhang, D. Shi and G. Zhang, *Nano Lett.*, 2011, **11**, 4083–4088.
21 I. A. Verzhbitskiy, M. D. Corato, A. Ruini, E. Molinari, A. Narita, Y. Hu, M. G. Schwab, M. Bruna, D. Yoon and S. Milana, *et al.*, *Nano Lett.*, 2016, **16**, 3442–3447.
22 A. K. Geim and K. S. Novoselov, *Nat. Mater.*, 2007, **6**, 183–191.
23 F. Bonaccorso, Z. Sun, T. Hasan and A. Ferrari, *Nat. Photonics*, 2010, **4**, 611–622.
24 Y.-M. Lin, C. Dimitrakopoulos, K. A. Jenkins, D. B. Farmer, H.-Y. Chiu, A. Grill and P. Avouris, *Science*, 2010, **327**, 662.
25 F. Torrisi, T. Hasan, W. Wu, Z. Sun, A. Lombardo, T. S. Kulmala, G.-W. Hsieh, S. Jung, F. Bonaccorso and P. J. Paul, *et al.*, *ACS Nano*, 2012, **6**, 2992–3006.
26 Z. Sun, T. Hasan, F. Torrisi, D. Popa, G. Privitera, F. Wang, F. Bonaccorso, D. M. Basko and A. C. Ferrari, *ACS Nano*, 2010, **4**, 803–810.
27 L. Miao, J. Wu, J. Jiang and P. Liang, *J. Phys. Chem. C*, 2012, **117**, 23–27.
28 A. K. Geim and I. V. Grigorieva, *Nature*, 2013, **499**, 419–425.
29 K. S. Novoselov, A. Mishchenko, A. Carvalho and A. H. C. Neto, *Science*, 2016, **353**, 6298.
30 D. Bischoff, M. Eich, A. Varlet, P. Simonet, H. C. Overweg, K. Ensslin and T. Ihn, *Mater. Today*, 2016, **19**, 375–381.
31 L. Britnell, R. V. Gorbachev, B. D. Jalil, R. Belle, F. Schedin, A. Mishchenko, T. Georgiou, M. I. Katsnelson, L. Eaves, S. V. Morozov, N. M. Peres, J. Leist, A. K. Geim, K. S. Novoselov and L. A. Ponomarenko, *Science*, 2012, **335**, 947–950.
32 L. Britnell, R. M. Ribeiro, A. Eckmann, R. Jalil, B. D. Belle, A. Mishchenko, Y.-J. Kim, R. V. Gorbachev, T. Georgiou, S. V. Morozov, A. N. Grigorenko, A. K. Geim, C. Casiraghi, A. H. C. Neto and K. S. Novoselov, *Science*, 2013, **340**, 1311–1314.
33 W. J. Yu, Z. Li, H. Zhou, Y. Chen, Y. Wang, Y. Huang and X. Duan, *Nat. Mater.*, 2013, **12**, 246–252.
34 T. Georgiou, R. Jalil, B. D. Belle, L. Britnell, R. V. Gorbachev, S. V. Morozov, Y.-J. Kim, A. Gholinia, S. J. Haigh, O. Makarovsky, L. Eaves, L. A. Ponomarenko, A. K. Geim, K. S. Novoselov and A. Mishchenko, *Nat. Nanotechnol.*, 2013, **8**, 100–103.
35 F. Withers, O. Del Pozo-Zamudio, A. Mishchenko, A. P. Rooney, A. Gholinia, K. Watanabe, T. Taniguchi, S. J. Haigh, A. K. Geim, A. I. Tartakovskii and K. S. Novoselov, *Nat. Mater.*, 2015, **14**, 301–306.
36 H. Li, J.-B. Wu, F. Ran, M.-L. Lin, X.-L. Liu, Y. Zhao, X. Lu, Q. Xiong, J. Zhang, W. Huang, H. Zhang and P.-H. Tan, *ACS Nano*, 2017, **11**, 11714–11723.
37 A. Azizi, S. M. Eichfeld, G. Geschwind, K. Zhang, B. Jiang, D. Mukherjee, L. Hossain, A. F. Piasecki, B. Kabius and J. A. Robinson, *et al.*, *ACS Nano*, 2015, **9**, 4882–4890.
38 Y. Lin, J. Li, S. C. D. La Barrera, S. M. Eichfeld, Y. Nie, R. Addou, P. Mende, R. M. Wallace, K. Cho and R. M. Feenstra, *et al.*, *Nanoscale*, 2016, **8**, 8947–8954.
39 M. M. Furchi, A. Pospischil, F. Libisch, J. Burgdorfer and T. Mueller, *Nano Lett.*, 2014, **14**, 4785–4791.
40 F. Withers, O. D. Pozozamudio, A. Mishchenko, A. P. Rooney, A. Gholinia, K. Watanabe, T. Taniguchi, S. J. Haigh, A. K. Geim and A. I. Tartakovskii, *et al.*, *Nat. Mater.*, 2015, **14**, 301–306.
41 G. Lee, Y. Yu, X. Cui, N. Petrone, C. Lee, M. S. Choi, D. Lee, C. Lee, W. J. Yoo and K. Watanabe, *et al.*, *ACS Nano*, 2013, **7**, 7931–7936.
42 M. S. Choi, G. Lee, Y. Yu, D. Lee, S. H. Lee, P. Kim, J. Hone and W. J. Yoo, *Nat. Commun.*, 2013, **4**, 1624.
43 A. Milani, M. Tommasini, V. Russo, A. L. Bassi, A. Lucotti, F. Cataldo and C. S. Casari, *Beilstein J. Nanotechnol.*, 2015, **6**, 480–491.
44 A. Ferrari, J. Meyer, V. Scardaci, C. Casiraghi, M. Lazzeri, F. Mauri, S. Piscanec, D. Jiang, K. Novoselov and S. Roth, *et al.*, *Phys. Rev. Lett.*, 2006, **97**, 187401.
45 F. Tuinstra and J. L. Koenig, *J. Chem. Phys.*, 1970, **53**, 1126–1130.
46 J. W. Ager III, D. K. Veirs and G. M. Rosenblatt, *Phys. Rev. B: Condens. Matter Mater. Phys.*, 1991, **43**, 6491.
47 M. S. Dresselhaus, A. Jorio, M. Hofmann, G. Dresselhaus and R. Saito, *Nano Lett.*, 2010, **10**, 751–758.
48 F. Innocenti, A. Milani and C. Castiglioni, *J. Raman Spectrosc.*, 2010, **41**, 226–236.
49 L. Malard, M. Pimenta, G. Dresselhaus and M. Dresselhaus, *Phys. Rep.*, 2009, **473**, 51–87.
50 A. C. Ferrari and J. Robertson, *Phys. Rev. B: Condens. Matter Mater. Phys.*, 2000, **61**, 14095.
51 M. S. Dresselhaus, G. Dresselhaus, R. Saito and A. Jorio, *Phys. Rep.*, 2005, **409**, 47–99.
52 D. S. Bethune, G. Meijer, W. C. Tang, H. J. Rosen, W. G. Golden, H. Seki, C. A. Brown and M. S. de Vries, *Chem. Phys. Lett.*, 1991, **179**, 181–186.
53 M.-L. Lin, J.-B. Wu, X.-L. Liu and P.-H. Tan, *J. Raman Spectrosc.*, 2017, DOI: 10.1002/jrs.5224.
54 L. Liang, J. Zhang, B. G. Sumpter, Q. Tan, P.-H. Tan and V. Meunier, *ACS Nano*, 2017, **11**, 11777–11802.

55 A. C. Ferrari, *Solid State Commun.*, 2007, **143**, 47–57.
56 A. C. Ferrari and D. M. Basko, *Nat. Nanotechnol.*, 2013, **8**, 235–246.
57 J.-B. Wu, X. Zhang, M. Ijäs, W.-P. Han, X.-F. Qiao, X.-L. Li, D.-S. Jiang, A. C. Ferrari and P.-H. Tan, *Nat. Commun.*, 2014, **5**, 5309.
58 C.-F. Chen, C.-H. Park, B. W. Boudouris, J. Horng, B. Geng, C. Girit, A. Zettl, M. F. Crommie, R. A. Segalman and S. G. Louie, *et al.*, *Nature*, 2011, **471**, 617–620.
59 C. Casiraghi, S. Pisana, K. Novoselov, A. Geim and A. Ferrari, *Appl. Phys. Lett.*, 2007, **91**, 233108.
60 A. Das, S. Pisana, B. Chakraborty, S. Piscanec, S. Saha, U. Waghmare, K. Novoselov, H. Krishnamurthy, A. Geim and A. Ferrari, *et al.*, *Nat. Nanotechnol.*, 2008, **3**, 210–215.
61 W.-J. Zhao, P.-H. Tan, J. Liu and A. C. Ferrari, *J. Am. Chem. Soc.*, 2011, **133**, 5941–5946.
62 A. Das, B. Chakraborty, S. Piscanec, S. Pisana, A. Sood and A. Ferrari, *Phys. Rev. B: Condens. Matter Mater. Phys.*, 2009, **79**, 155417.
63 S. Pisana, M. Lazzeri, C. Casiraghi, K. S. Novoselov, A. K. Geim, A. C. Ferrari and F. Mauri, *Nat. Mater.*, 2007, **6**, 198–201.
64 J. Yan, Y. Zhang, P. Kim and A. Pinczuk, *Phys. Rev. Lett.*, 2007, **98**, 166802.
65 J. Yan, E. A. Henriksen, P. Kim and A. Pinczuk, *Phys. Rev. Lett.*, 2008, **101**, 136804.
66 E. M. Ferreira, M. V. Moutinho, F. Stavale, M. Lucchese, R. B. Capaz, C. Achete and A. Jorio, *Phys. Rev. B: Condens. Matter Mater. Phys.*, 2010, **82**, 125429.
67 D. Yang, A. Velamakanni, G. Bozoklu, S. Park, M. Stoller, R. D. Piner, S. Stankovich, I. Jung, D. A. Field and C. A. Ventrice, *et al.*, *Carbon*, 2009, **47**, 145–152.
68 L. Zhang, Z. Shi, Y. Wang, R. Yang, D. Shi and G. Zhang, *Nano Res.*, 2011, **4**, 315–321.
69 C. Thomsen and S. Reich, *Phys. Rev. Lett.*, 2000, **85**, 5214.
70 P.-H. Tan, W.-P. Han, W.-J. Zhao, Z.-H. Wu, K. Chang, H. Wang, Y.-F. Wang, N. Bonini, N. Marzari and N. Pugno, *et al.*, *Nat. Mater.*, 2012, **11**, 294–300.
71 J.-B. Wu, Z.-X. Hu, X. Zhang, W.-P. Han, Y. Lu, W. Shi, X.-F. Qiao, M. Ijiäs, S. Milana and W. Ji, *et al.*, *ACS Nano*, 2015, **9**, 7440–7449.
72 D. Basko, *New J. Phys.*, 2009, **11**, 095011.
73 D. Yoon, H. Moon, Y.-W. Son, J. S. Choi, B. H. Park, Y. H. Cha, Y. D. Kim and H. Cheong, *Phys. Rev. B: Condens. Matter Mater. Phys.*, 2009, **80**, 125422.
74 D. Basko, *Phys. Rev. B: Condens. Matter Mater. Phys.*, 2009, **79**, 205428.
75 Y. You, Z. Ni, T. Yu and Z. Shen, *Appl. Phys. Lett.*, 2008, **93**, 3112.
76 A. K. Gupta, T. J. Russin, H. R. Gutiérrez and P. C. Eklund, *ACS Nano*, 2008, **3**, 45–52.
77 C. Casiraghi, A. Hartschuh, H. Qian, S. Piscanec, C. Georgi, A. Fasoli, K. Novoselov, D. Basko and A. Ferrari, *Nano Lett.*, 2009, **9**, 1433–1441.
78 C. Cong, T. Yu and H. Wang, *ACS Nano*, 2010, **4**, 3175–3180.
79 S. Ryu, J. Maultzsch, M. Y. Han, P. Kim and L. E. Brus, *ACS Nano*, 2011, **5**, 4123–4130.
80 P. Venezuela, M. Lazzeri and F. Mauri, *Phys. Rev. B: Condens. Matter Mater. Phys.*, 2011, **84**, 035433.
81 M. Huang, H. Yan, T. F. Heinz and J. Hone, *Nano Lett.*, 2010, **10**, 4074–4079.
82 M. Mohr, J. Maultzsch and C. Thomsen, *Phys. Rev. B: Condens. Matter Mater. Phys.*, 2010, **82**, 201409.
83 D. Yoon, Y.-W. Son and H. Cheong, *Phys. Rev. Lett.*, 2011, **106**, 155502.
84 T. Mohiuddin, A. Lombardo, R. Nair, A. Bonetti, G. Savini, R. Jalil, N. Bonini, D. Basko, C. Galiotis and N. Marzari, *et al.*, *Phys. Rev. B: Condens. Matter Mater. Phys.*, 2009, **79**, 205433.
85 Z. H. Ni, T. Yu, Y. H. Lu, Y. Y. Wang, Y. P. Feng and Z. X. Shen, *ACS Nano*, 2008, **2**, 2301–2305.
86 J. E. Proctor, E. Gregoryanz, K. S. Novoselov, M. Lotya, J. N. Coleman and M. P. Halsall, *Phys. Rev. B: Condens. Matter Mater. Phys.*, 2009, **80**, 073408.
87 M. Huang, H. Yan, C. Chen, D. Song, T. F. Heinz and J. Hone, *Proc. Natl. Acad. Sci. U. S. A.*, 2009, **106**, 7304–7308.
88 M. Goerbig, J.-N. Fuchs, K. Kechedzhi and V. I. Falko, *Phys. Rev. Lett.*, 2007, **99**, 087402.
89 O. Kashuba and V. I. Falko, *Phys. Rev. B: Condens. Matter Mater. Phys.*, 2009, **80**, 241404.
90 C. Faugeras, M. Amado, P. Kossacki, M. Orlita, M. Sprinkle, C. Berger, W. De Heer and M. Potemski, *Phys. Rev. Lett.*, 2009, **103**, 186803.
91 J. Yan, S. Goler, T. D. Rhone, M. Han, R. He, P. Kim, V. Pellegrini and A. Pinczuk, *Phys. Rev. Lett.*, 2010, **105**, 227401.
92 C. Faugeras, M. Amado, P. Kossacki, M. Orlita, M. Kühne, A. Nicolet, Y. I. Latyshev and M. Potemski, *Phys. Rev. Lett.*, 2011, **107**, 036807.
93 Y. Kim, Y. Ma, A. Imambekov, N. Kalugin, A. Lombardo, A. Ferrari, J. Kono and D. Smirnov, *Phys. Rev. B: Condens. Matter Mater. Phys.*, 2012, **85**, 121403.
94 P. Kossacki, C. Faugeras, M. Kühne, M. Orlita, A. Mahmood, E. Dujardin, R. Nair, A. Geim and M. Potemski, *Phys. Rev. B: Condens. Matter Mater. Phys.*, 2012, **86**, 205431.
95 Y. Kim, J. Poumirol, A. Lombardo, N. Kalugin, T. Georgiou, Y. Kim, K. Novoselov, A. Ferrari, J. Kono and O. Kashuba, *et al.*, *Phys. Rev. Lett.*, 2013, **110**, 227402.
96 C. Qiu, X. Shen, B. Cao, C. Cong, R. Saito, J. Yu, M. S. Dresselhaus and T. Yu, *Phys. Rev. B: Condens. Matter Mater. Phys.*, 2013, **88**, 165407.
97 C. Cong, J. Jung, B. Cao, C. Qiu, X. Shen, A. Ferreira, S. Adam and T. Yu, *Phys. Rev. B: Condens. Matter Mater. Phys.*, 2015, **91**, 235403.
98 C. Faugeras, M. Orlita and M. Potemski, *J. Raman Spectrosc.*, 2017, DOI: 10.1002/jrs.5213.
99 A. A. Balandin, S. Ghosh, W. Bao, I. Calizo, D. Teweldebrhan, F. Miao and C. N. Lau, *Nano Lett.*, 2008, **8**, 902–907.
100 N. Bonini, M. Lazzeri, N. Marzari and F. Mauri, *Phys. Rev. Lett.*, 2007, **99**, 176802.
101 J.-U. Lee, D. Yoon, H. Kim, S. W. Lee and H. Cheong, *Phys. Rev. B: Condens. Matter Mater. Phys.*, 2011, **83**, 081419.

102 S. Chen, Q. Wu, C. Mishra, J. Kang, H. Zhang, K. Cho, W. Cai, A. A. Balandin and R. S. Ruoff, *Nat. Mater.*, 2012, **11**, 203–207.
103 W. Cai, A. L. Moore, Y. Zhu, X. Li, S. Chen, L. Shi and R. S. Ruoff, *Nano Lett.*, 2010, **10**, 1645–1651.
104 A. H. Castro Neto, F. Guinea, N. M. R. Peres, K. S. Novoselov and A. K. Geim, *Rev. Mod. Phys.*, 2009, **81**, 109–162.
105 Y. M. Chang, H. Kim, J. H. Lee and Y.-W. Song, *Appl. Phys. Lett.*, 2010, **97**, 211102.
106 A. Martinez, K. Fuse and S. Yamashita, *Appl. Phys. Lett.*, 2011, **99**, 121107.
107 M. Yi and Z. Shen, *J. Mater. Chem. A*, 2015, **3**, 11700–11715.
108 P. Blake, E. Hill, A. C. Neto, K. Novoselov, D. Jiang, R. Yang, T. Booth and A. Geim, *Appl. Phys. Lett.*, 2007, **91**, 063124.
109 C. Casiraghi, A. Hartschuh, E. Lidorikis, H. Qian, H. Harutyunyan, T. Gokus, K. Novoselov and A. Ferrari, *Nano Lett.*, 2007, **7**, 2711–2717.
110 M. J. Allen, V. C. Tung and R. B. Kaner, *Chem. Rev.*, 2009, **110**, 132–145.
111 J. M. Dawlaty, S. Shivaraman, J. Strait, P. George, M. Chandrashekhar, F. Rana, M. G. Spencer, D. Veksler and Y. Chen, *Appl. Phys. Lett.*, 2008, **93**, 131905.
112 S. Latil and L. Henrard, *Phys. Rev. Lett.*, 2006, **97**, 036803.
113 M. Aoki and H. Amawashi, *Solid State Commun.*, 2007, **142**, 123–127.
114 L. Malard, J. Nilsson, D. Elias, J. Brant, F. Plentz, E. Alves, A. C. Neto and M. Pimenta, *Phys. Rev. B: Condens. Matter Mater. Phys.*, 2007, **76**, 201401.
115 W.-J. Zhao, P.-H. Tan, J. Zhang and J. Liu, *Phys. Rev. B: Condens. Matter Mater. Phys.*, 2010, **82**, 245423.
116 M. Lazzeri, C. Attaccalite, L. Wirtz and F. Mauri, *Phys. Rev. B: Condens. Matter Mater. Phys.*, 2008, **78**, 081406.
117 P.-H. Tan, C.-Y. Hu, J. Dong, W.-C. Shen and B.-F. Zhang, *Phys. Rev. B: Condens. Matter Mater. Phys.*, 2001, **64**, 214301.
118 S. Reich and C. Thomsen, *Philos. Trans. R. Soc., A*, 2004, **362**, 2271–2288.
119 K. Mani and R. Ramani, *Phys. Status Solidi B*, 1974, **61**, 659–668.
120 R. J. Nemanich, G. Lucovsky and S. A. Solin, Proceedings of the International Conference on Lattice Dynamics, Flammarion, 1975.
121 M. Dresselhaus and G. Dresselhaus, *Adv. Phys.*, 1981, **30**, 139–326.
122 C. Cong, T. Yu, R. Saito, G. F. Dresselhaus and M. S. Dresselhaus, *ACS Nano*, 2011, **5**, 1600–1605.
123 R. Rao, R. Podila, R. Tsuchikawa, J. Katoch, D. Tishler, A. M. Rao and M. Ishigami, *ACS Nano*, 2011, **5**, 1594–1599.
124 M. Born and K. Huang, *Dynamical theory of crystal lattices*, Oxford University Press, 1998.
125 M. Mohr, J. Maultzsch, E. Dobardžić, S. Reich, I. Milošević, M. Damnjanović, A. Bosak, M. Krisch and C. Thomsen, *Phys. Rev. B: Condens. Matter Mater. Phys.*, 2007, **76**, 035439.
126 S. Siebentritt, R. Pues, K.-H. Rieder and A. M. Shikin, *Phys. Rev. B: Condens. Matter Mater. Phys.*, 1997, **55**, 7927.
127 R. Saito, A. Jorio, A. Souza Filho, G. Dresselhaus, M. Dresselhaus and M. Pimenta, *Phys. Rev. Lett.*, 2001, **88**, 027401.
128 P.-H. Tan, L. An, L. Liu, Z. Guo, R. Czerw, D. L. Carroll, P. M. Ajayan, N. Zhang and H. Guo, *Phys. Rev. B: Condens. Matter Mater. Phys.*, 2002, **66**, 245410.
129 S. Piscanec, M. Lazzeri, F. Mauri, A. Ferrari and J. Robertson, *Phys. Rev. Lett.*, 2004, **93**, 185503.
130 R. R. Nair, W. Ren, R. Jalil, I. Riaz, V. G. Kravets, L. Britnell, P. Blake, F. Schedin, A. S. Mayorov, S. Yuan, M. I. Katsnelson, H.-M. Cheng, W. Strupinski, L. G. Bulusheva, A. V. Okotrub, I. V. Grigorieva, A. N. Grigorenko, K. S. Novoselov and A. K. Geim, *Small*, 2010, **6**, 2877–2884.
131 I. Childres, L. A. Jauregui, J. Tian and Y. P. Chen, *New J. Phys.*, 2011, **13**, 025008.
132 Y. Peter and M. Cardona, *Fundamentals of semiconductors: physics and materials properties*, Springer Science & Business Media, 2010.
133 I. Pócsik, M. Hundhausen, M. Koós and L. Ley, *J. Non-Cryst. Solids*, 1998, **227**, 1083–1086.
134 P. May, M. Lazzeri, P. Venezuela, F. Herziger, G. Callsen, J. S. Reparaz, A. Hoffmann, F. Mauri and J. Maultzsch, *Phys. Rev. B: Condens. Matter Mater. Phys.*, 2013, **87**, 075402.
135 P.-H. Tan, Y. Deng and Q. Zhao, *Phys. Rev. B: Condens. Matter Mater. Phys.*, 1998, **58**, 5435.
136 Y. Kawashima and G. Katagiri, *Phys. Rev. B: Condens. Matter Mater. Phys.*, 1995, **52**, 10053.
137 J. Jiang, R. Saito, G. G. Samsonidze, S. G. Chou, A. Jorio, G. Dresselhaus and M. S. Dresselhaus, *Phys. Rev. B: Condens. Matter Mater. Phys.*, 2005, **72**, 235408.
138 D. Basko, S. Piscanec and A. Ferrari, *Phys. Rev. B: Condens. Matter Mater. Phys.*, 2009, **80**, 165413.
139 R. Vidano, D. Fischbach, L. Willis and T. Loehr, *Solid State Commun.*, 1981, **39**, 341–344.
140 D. Yoon, H. Moon, Y.-W. Son, G. Samsonidze, B. H. Park, J. B. Kim, Y. Lee and H. Cheong, *Nano Lett.*, 2008, **8**, 4270–4274.
141 S. Sahoo, R. Palai and R. Katiyar, *J. Appl. Phys.*, 2011, **110**, 044320.
142 L. Malard, M. Guimaraes, D. Mafra and A. Jorio, *Phys. Rev. B: Condens. Matter Mater. Phys.*, 2009, **79**, 125426.
143 C. Cong and T. Yu, *Phys. Rev. B: Condens. Matter Mater. Phys.*, 2014, **89**, 235430.
144 C. Cong and T. Yu, *Nat. Commun.*, 2014, **5**, 4709.
145 M. Bruna and S. Borini, *Phys. Rev. B: Condens. Matter Mater. Phys.*, 2010, **81**, 125421.
146 L. Malard, D. Elias, E. Alves and M. Pimenta, *Phys. Rev. Lett.*, 2008, **101**, 257401.
147 J. Zabel, R. R. Nair, A. Ott, T. Georgiou, A. K. Geim, K. S. Novoselov and C. Casiraghi, *Nano Lett.*, 2012, **12**, 617–621.
148 S. K. Saha, U. Waghmare, H. Krishnamurthy and A. Sood, *Phys. Rev. B: Condens. Matter Mater. Phys.*, 2008, **78**, 165421.
149 J.-W. Jiang, H. Tang, B.-S. Wang and Z.-B. Su, *Phys. Rev. B: Condens. Matter Mater. Phys.*, 2008, **77**, 235421.
150 X. Zhang, W.-P. Han, X.-F. Qiao, Q.-H. Tan, Y.-F. Wang, J. Zhang and P.-H. Tan, *Carbon*, 2016, **99**, 118–122.
151 X. Zhang, W.-P. Han, J.-B. Wu, S. Milana, Y. Lu, Q.-Q. Li, A. Ferrari and P.-H. Tan, *Phys. Rev. B: Condens. Matter Mater. Phys.*, 2013, **87**, 115413.

152 P.-H. Tan, J.-B. Wu, W.-P. Han, W.-J. Zhao, X. Zhang, H. Wang and Y.-F. Wang, *Phys. Rev. B: Condens. Matter Mater. Phys.*, 2014, **89**, 235404.
153 C. H. Lui, L. M. Malard, S. Kim, G. Lantz, F. E. Laverge, R. Saito and T. F. Heinz, *Nano Lett.*, 2012, **12**, 5539–5544.
154 C. H. Lui, Z. Ye, C. Keiser, X. Xiao and R. He, *Nano Lett.*, 2014, **14**, 4615–4621.
155 X. Zhang, X.-F. Qiao, W. Shi, J.-B. Wu, D.-S. Jiang and P.-H. Tan, *Chem. Soc. Rev.*, 2015, **44**, 2757–2785.
156 Y. Zhao, X. Luo, H. Li, J. Zhang, P. T. Araujo, C. K. Gan, J. Wu, H. Zhang, S. Y. Quek and M. S. Dresselhaus, *et al.*, *Nano Lett.*, 2013, **13**, 1007–1015.
157 X. Ling, L. Liang, S. Huang, A. A. Puretzky, D. B. Geohegan, B. G. Sumpter, J. Kong, V. Meunier and M. S. Dresselhaus, *Nano Lett.*, 2015, **15**, 4080–4088.
158 C. H. Lui, Z. Ye, C. Ji, K.-C. Chiu, C.-T. Chou, T. I. Andersen, C. Means-Shively, H. Anderson, J.-M. Wu and T. Kidd, *et al.*, *Phys. Rev. B: Condens. Matter Mater. Phys.*, 2015, **91**, 165403.
159 H. Zhao, J. Wu, H. Zhong, Q. Guo, X. Wang, F. Xia, L. Yang, P.-H. Tan and H. Wang, *Nano Res.*, 2015, **8**, 3651–3661.
160 Y. Zhao, X. Luo, J. Zhang, J. Wu, X. Bai, M. Wang, J. Jia, H. Peng, Z. Liu and S. Y. Quek, *et al.*, *Phys. Rev. B: Condens. Matter Mater. Phys.*, 2014, **90**, 245428.
161 X.-F. Qiao, J.-B. Wu, L. Zhou, J. Qiao, W. Shi, T. Chen, X. Zhang, J. Zhang, W. Ji and P.-H. Tan, *Nanoscale*, 2016, **8**, 8324–8332.
162 A. A. Puretzky, L. Liang, X. Li, K. Xiao, B. G. Sumpter, V. Meunier and D. B. Geohegan, *ACS Nano*, 2016, **10**, 2736–2744.
163 E. Lorchat, G. Froehlicher and S. Berciaud, *ACS Nano*, 2016, **10**, 2752–2760.
164 J.-W. Jiang, B.-S. Wang and H. S. Park, *J. Phys.: Condens. Matter*, 2016, **28**, 165401.
165 S. Huang, L. Liang, X. Ling, A. A. Puretzky, D. B. Geohegan, B. G. Sumpter, J. Kong, V. Meunier and M. S. Dresselhaus, *Nano Lett.*, 2016, **16**, 1435–1444.
166 S. Dong, A. Zhang, K. Liu, J. Ji, Y. Ye, X. Luo, X. Chen, X. Ma, Y. Jie and C. Chen, *et al.*, *Phys. Rev. Lett.*, 2016, **116**, 087401.
167 X.-F. Qiao, X.-L. Li, X. Zhang, W. Shi, J.-B. Wu, T. Chen and P.-H. Tan, *Appl. Phys. Lett.*, 2015, **106**, 223102.
168 X.-L. Li, W.-P. Han, J.-B. Wu, X.-F. Qiao, J. Zhang and P.-H. Tan, *Adv. Funct. Mater.*, 2017, **27**, 1604468.
169 C. H. Lui, Z. Ye, C. Keiser, E. B. Barros and R. He, *Appl. Phys. Lett.*, 2015, **106**, 041904.
170 H. Wilhelm, B. Croset and G. Medjahdi, *Carbon*, 2007, **45**, 2356–2364.
171 T. Nguyen, J. Lee, D. Yoon and H. Cheong, *Sci. Rep.*, 2014, **4**, 4630.
172 V. Carozo, C. Almeida, B. Fragneaud, P. Bedê, M. Moutinho, J. Ribeiro-Soares, N. Andrade, A. Souza Filho, M. Matos and B. Wang, *et al.*, *Phys. Rev. B: Condens. Matter Mater. Phys.*, 2013, **88**, 085401.
173 V. Carozo, C. M. Almeida, E. H. Ferreira, L. G. Cançado, C. A. Achete and A. Jorio, *Nano Lett.*, 2011, **11**, 4527–4534.
174 E. J. Mele, *Phys. Rev. B: Condens. Matter Mater. Phys.*, 2010, **81**, 161405.
175 R. Bistritzer and A. H. MacDonald, *Proc. Natl. Acad. Sci. U. S. A.*, 2011, **108**, 12233–12237.
176 D. S. Lee, C. Riedl, T. Beringer, A. C. Neto, K. von Klitzing, U. Starke and J. H. Smet, *Phys. Rev. Lett.*, 2011, **107**, 216602.
177 E. S. Morell, J. Correa, P. Vargas, M. Pacheco and Z. Barticevic, *Phys. Rev. B: Condens. Matter Mater. Phys.*, 2010, **82**, 121407.
178 P. Moon and M. Koshino, *Phys. Rev. B: Condens. Matter Mater. Phys.*, 2013, **87**, 205404.
179 R. Bistritzer and A. MacDonald, *Phys. Rev. B: Condens. Matter Mater. Phys.*, 2011, **84**, 035440.
180 A. Luican, G. Li, A. Reina, J. Kong, R. Nair, K. S. Novoselov, A. K. Geim and E. Andrei, *Phys. Rev. Lett.*, 2011, **106**, 126802.
181 G. Trambly de Laissardière, D. Mayou and L. Magaud, *Nano Lett.*, 2010, **10**, 804–808.
182 J. L. Dos Santos, N. Peres and A. C. Neto, *Phys. Rev. Lett.*, 2007, **99**, 256802.
183 G. Li, A. Luican, J. L. Dos Santos, A. C. Neto, A. Reina, J. Kong and E. Andrei, *Nat. Phys.*, 2010, **6**, 109–113.
184 J. D. Sanchez-Yamagishi, T. Taychatanapat, K. Watanabe, T. Taniguchi, A. Yacoby and P. Jarillo-Herrero, *Phys. Rev. Lett.*, 2012, **108**, 076601.
185 R. W. Havener, H. Zhuang, L. Brown, R. G. Hennig and J. Park, *Nano Lett.*, 2012, **12**, 3162–3167.
186 K. Kim, S. Coh, L. Z. Tan, W. Regan, J. M. Yuk, E. Chatterjee, M. Crommie, M. L. Cohen, S. G. Louie and A. Zettl, *Phys. Rev. Lett.*, 2012, **108**, 246103.
187 Z. Ni, Y. Wang, T. Yu, Y. You and Z. Shen, *Phys. Rev. B: Condens. Matter Mater. Phys.*, 2008, **77**, 235403.
188 E. S. Morell, M. Pacheco, L. Chico and L. Brey, *Phys. Rev. B: Condens. Matter Mater. Phys.*, 2013, **87**, 125414.
189 A. K. Gupta, Y. Tang, V. H. Crespi and P. C. Eklund, *Phys. Rev. B: Condens. Matter Mater. Phys.*, 2010, **82**, 241406.
190 J. T. Robinson, S. W. Schmucker, C. B. Diaconescu, J. P. Long, J. C. Culbertson, T. Ohta, A. L. Friedman and T. E. Beechem, *ACS Nano*, 2012, **7**, 637–644.
191 J. Campos-Delgado, G. Algara-Siller, C. Santos, U. Kaiser and J.-P. Raskin, *Small*, 2013, **9**, 3247–3251.
192 J. Coraux, T. N. Plasa, C. Busse and T. Michely, *New J. Phys.*, 2008, **10**, 043033.
193 U. Fano, *Phys. Rev.*, 1961, **124**, 1866.
194 F. Cerdeira, T. Fjeldly and M. Cardona, *Phys. Rev. B: Solid State*, 1973, **8**, 4734.
195 H. Lin, L. A. Wray, Y. Xia, S. Xu, S. Jia, R. J. Cava, A. Bansil and M. Z. Hasan, *Nat. Mater.*, 2010, **9**, 546–549.
196 R. Gupta, Q. Xiong, C. Adu, U. Kim and P. Eklund, *Nano Lett.*, 2003, **3**, 627–631.
197 J. Zhang, Z. Peng, A. Soni, Y. Zhao, Y. Xiong, B. Peng, J. Wang, M. S. Dresselhaus and Q. Xiong, *Nano Lett.*, 2011, **11**, 2407–2414.
198 M. Klein and M. Cardona, *Top. Appl. Phys.*, 1975, **8**, 148.
199 D. Yoon, D. Jeong, H.-J. Lee, R. Saito, Y.-W. Son, H. C. Lee and H. Cheong, *Carbon*, 2013, **61**, 373–378.

200 Z. Li, C. H. Lui, E. Cappelluti, L. Benfatto, K. F. Mak, G. L. Carr, J. Shan and T. F. Heinz, *Phys. Rev. Lett.*, 2012, **108**, 156801.
201 T.-T. Tang, Y. Zhang, C.-H. Park, B. Geng, C. Girit, Z. Hao, M. C. Martin, A. Zettl, M. F. Crommie and S. G. Louie, *et al.*, *Nat. Nanotechnol.*, 2010, **5**, 32–36.
202 J.-B. Wu, H. Wang, X.-L. Li, H. Peng and P.-H. Tan, *Carbon*, 2016, **110**, 225–231.
203 R. He, T.-F. Chung, C. Delaney, C. Keiser, L. A. Jauregui, P. M. Shand, C. Chancey, Y. Wang, J. Bao and Y. P. Chen, *Nano Lett.*, 2013, **13**, 3594–3601.
204 Y. Y. Wang, J. Jiang, C. W. Gao, H. Y. Nan, Z. H. Ni, D. Wang, B. Zhong and G. W. Wen, *J. Raman Spectrosc.*, 2016, **47**, 668–673.
205 M.-L. Lin, T. Chen, W. Lu, Q.-H. Tan, P. Zhao, H.-T. Wang, Y. Xu and P.-H. Tan, *J. Raman Spectrosc.*, 2017, DOI: 10.1002/jrs.5219.
206 A. Eckmann, A. Felten, A. Mishchenko, L. Britnell, R. Krupke, K. S. Novoselov and C. Casiraghi, *Nano Lett.*, 2012, **12**, 3925–3930.
207 Q.-Q. Li, X. Zhang, W.-P. Han, Y. Lu, W. Shi, J.-B. Wu and P.-H. Tan, *Carbon*, 2015, **85**, 221–224.
208 F. Banhart, J. Kotakoski and A. V. Krasheninnikov, *ACS Nano*, 2011, **5**, 26–41.
209 Z. H. Ni, L. A. Ponomarenko, R. R. Nair, R. Yang, S. Anissimova, I. V. Grigorieva, F. Schedin, P. Blake, Z. X. Shen, E. H. Hill, K. S. Novoselov and A. K. Geim, *Nano Lett.*, 2010, **10**, 3868–3872.
210 J. Chen, W. G. Cullen, C. Jang, M. S. Fuhrer and E. D. Williams, *Phys. Rev. Lett.*, 2009, **102**, 236805.
211 J. Lahiri, Y. Lin, P. Bozkurt, I. I. Oleynik and M. Batzill, *Nat. Nanotechnol.*, 2010, **5**, 326–329.
212 L. D. Carr and M. T. Lusk, *Nat. Nanotechnol.*, 2010, **5**, 316–317.
213 D. W. Boukhvalov and M. I. Katsnelson, *Nano Lett.*, 2008, **8**, 4373–4379.
214 C. Casiraghi, A. C. Ferrari and J. Robertson, *Phys. Rev. B: Condens. Matter Mater. Phys.*, 2005, **72**, 085401.
215 P. Venezuela, M. Lazzeri and F. Mauri, *Phys. Rev. B: Condens. Matter Mater. Phys.*, 2011, **84**, 035433.
216 A. Jorio, M. S. Dresselhaus, R. Saito and G. F. Dresselhaus, *Raman spectrocopy in graphene-related systems*, Wiley-VCH, Weinheim, Germany, 2011.
217 Y. Stubrov, A. Nikolenko, V. Gubanov and V. Strelchuk, *Nanoscale Res. Lett.*, 2016, **11**, 2.
218 X. Zhang, Q.-Q. Li, W.-P. Han, Y. Lu, W. Shi, J.-B. Wu, A. S. Mikhaylushkin and P.-H. Tan, *Nanoscale*, 2014, **6**, 7519–7525.
219 L. G. Cançado, M. G. da Silva, E. H. M. Ferreira, F. Hof, K. Kampioti, K. Huang, A. Pénicaud, C. A. Achete, R. B. Capaz and A. Jorio, *2D Mater.*, 2017, **4**, 025039.
220 S. Mignuzzi, A. J. Pollard, N. Bonini, B. Brennan, I. S. Gilmore, M. A. Pimenta, D. Richards and D. Roy, *Phys. Rev. B: Condens. Matter Mater. Phys.*, 2015, **91**, 195411.
221 W. Shi, X. Zhang, X.-L. Li, X.-F. Qiao, J.-B. Wu, J. Zhang and P.-H. Tan, *Chin. Phys. Lett.*, 2016, **33**, 057801.
222 W. Shi, M.-L. Lin, Q.-H. Tan, X.-F. Qiao, J. Zhang and P.-H. Tan, *2D Mater.*, 2016, **3**, 025016.
223 L. Cançado, K. Takai, T. Enoki, M. Endo, Y. Kim, H. Mizusaki, A. Jorio, L. Coelho, R. Magalhaes-Paniago and M. Pimenta, *Appl. Phys. Lett.*, 2006, **88**, 163106.
224 J. Ribeiro-Soares, M. Oliveros, C. Garin, M. David, L. Martins, C. Almeida, E. Martins-Ferreira, K. Takai, T. Enoki and R. Magalhaes-Paniago, *et al.*, *Carbon*, 2015, **95**, 646–652.
225 L. Huang, Y. Huang, J. Liang, X. Wan and Y. Chen, *Nano Res.*, 2011, **4**, 675–684.
226 A. P. A. Raju, A. Lewis, B. Derby, R. J. Young, I. A. Kinloch, R. Zan and K. S. Novoselov, *Adv. Funct. Mater.*, 2014, **24**, 2865–2874.
227 M. Y. Han, B. Özyilmaz, Y. Zhang and P. Kim, *Phys. Rev. Lett.*, 2007, **98**, 206805.
228 P. Silvestrov and K. Efetov, *Phys. Rev. Lett.*, 2007, **98**, 016802.
229 Ç. Ö. Girit, J. C. Meyer, R. Erni, M. D. Rossell, C. Kisielowski, L. Yang, C.-H. Park, M. Crommie, M. L. Cohen and S. G. Louie, *et al.*, *Science*, 2009, **323**, 1705–1708.
230 K. A. Ritter and J. W. Lyding, *Nat. Mater.*, 2009, **8**, 235–242.
231 Y.-W. Son, M. L. Cohen and S. G. Louie, *Nature*, 2006, **444**, 347–349.
232 L. Cançado, M. Pimenta, B. Neves, M. Dantas and A. Jorio, *Phys. Rev. Lett.*, 2004, **93**, 247401.
233 P. Y. Huang, C. S. Ruiz-Vargas, A. M. van der Zande, W. S. Whitney, M. P. Levendorf, J. W. Kevek, S. Garg, J. S. Alden, C. J. Hustedt, Y. Zhu, J. Park, P. L. McEuen and D. A. Muller, *Nature*, 2011, **469**, 389–392.
234 J. T. Robinson, M. K. Zalalutdinov, C. D. Cress, J. C. Culbertson, A. L. Friedman, A. Merrill and B. J. Landi, *ACS Nano*, 2017, **11**, 4745–4752.
235 Y. Xu, A. Ali, K. Shehzad, N. Meng, M. Xu, Y. Zhang, X. Wang, C. Jin, H. Wang, Y. Guo, Z. Yang, B. Yu, Y. Liu, Q. He, X. Duan, X. Wang, P.-H. Tan, W. Hu, H. Lu and T. Hasan, *Adv. Mater. Technol.*, 2017, **2**, 1600241.
236 P. Lespade, A. Marchand, M. Couzi and F. Cruege, *Carbon*, 1984, **22**, 375–385.
237 J.-H. Zhong, J. Zhang, X. Jin, J.-Y. Liu, Q. Li, M.-H. Li, W. Cai, D.-Y. Wu, D. Zhan and B. Ren, *J. Am. Chem. Soc.*, 2014, **136**, 16609–16617.
238 O. V. Yazyev and S. G. Louie, *Phys. Rev. B: Condens. Matter Mater. Phys.*, 2010, **81**, 195420.
239 S. Stankovich, D. A. Dikin, G. H. B. Dommett, K. M. Kohlhaas, E. J. Zimney, E. A. Stach, R. D. Piner, S. T. Nguyen and R. S. Ruoff, *Nature*, 2006, **442**, 282–286.
240 D. C. Elias, R. R. Nair, T. M. G. Mohiuddin, S. V. Morozov, P. Blake, M. P. Halsall, A. C. Ferrari, D. W. Boukhvalov, M. I. Katsnelson, A. K. Geim and K. S. Novoselov, *Science*, 2009, **323**, 610–613.
241 C. Shen, G. Huang, Y. Cheng, R. Cao, F. Ding, U. Schwingenschlögl and Y. Mei, *Nanoscale Res. Lett.*, 2012, **7**, 268.
242 A. Felten, A. Eckmann, J.-J. Pireaux, R. Krupke and C. Casiraghi, *Nanotechnology*, 2013, **24**, 355705.

243 X. Dong, Y. Shi, Y. Zhao, D. Chen, J. Ye, Y. Yao, F. Gao, Z. Ni, T. Yu, Z. Shen, Y. Huang, P. Chen and L.-J. Li, *Phys. Rev. Lett.*, 2009, **102**, 135501.
244 X. Hong, K. Zou, B. Wang, S.-H. Cheng and J. Zhu, *Phys. Rev. Lett.*, 2012, **108**, 226602.
245 N. Soin, S. C. Ray, S. Sarma, D. Mazumder, S. Sharma, Y.-F. Wang, W.-F. Pong, S. S. Roy and A. M. Strydom, *J. Phys. Chem. C*, 2017, **121**, 14073–14082.
246 L. Cheng, S. Jandhyala, G. Mordi, A. T. Lucero, J. Huang, A. Azcatl, R. Addou, R. M. Wallace, L. Colombo and J. Kim, *ACS Appl. Mater. Interfaces*, 2016, **8**, 5002–5008.
247 J. T. Robinson, J. S. Burgess, C. E. Junkermeier, S. C. Badescu, T. L. Reinecke, F. K. Perkins, M. K. Zalalutdniov, J. W. Baldwin, J. C. Culbertson, P. E. Sheehan and E. S. Snow, *Nano Lett.*, 2010, **10**, 3001–3005.
248 S.-H. Cheng, K. Zou, F. Okino, H. R. Gutierrez, A. Gupta, N. Shen, P. C. Eklund, J. O. Sofo and J. Zhu, *Phys. Rev. B: Condens. Matter Mater. Phys.*, 2010, **81**, 205435.
249 H. Yang, M. Chen, H. Zhou, C. Qiu, L. Hu, F. Yu, W. Chu, S. Sun and L. Sun, *J. Phys. Chem. C*, 2011, **115**, 16844–16848.
250 Y. Wang, Z. Ni, Z. Shena, H. Wang and Y. Wu, *Appl. Phys. Lett.*, 2008, **92**, 043121.
251 Z. Ni, W. Chen, X. Fan, J. Kuo, T. Yu, A. Wee and Z. Shen, *Phys. Rev. B: Condens. Matter Mater. Phys.*, 2008, **77**, 115416.
252 X.-L. Li, X.-F. Qiao, W.-P. Han, Y. Lu, Q.-H. Tan, X.-L. Liu and P.-H. Tan, *Nanoscale*, 2015, **7**, 8135–8141.
253 H. Starnberg, H. Brauer, L. Holleboom and H. Hughes, *Phys. Rev. Lett.*, 1993, **70**, 3111.
254 H. Ramakrishna Matte, A. Gomathi, A. K. Manna, D. J. Late, R. Datta, S. K. Pati and C. Rao, *Angew. Chem., Int. Ed.*, 2010, **122**, 4153–4156.
255 H. Fang, S. Chuang, T. C. Chang, K. Takei, T. Takahashi and A. Javey, *Nano Lett.*, 2012, **12**, 3788–3792.
256 D. Kong, H. Wang, J. J. Cha, M. Pasta, K. J. Koski, J. Yao and Y. Cui, *Nano Lett.*, 2013, **13**, 1341–1347.
257 Q.-J. Song, Q.-H. Tan, X. Zhang, J.-B. Wu, B.-W. Sheng, Y. Wan, X.-Q. Wang, L. Dai and P.-H. Tan, *Phys. Rev. B: Condens. Matter Mater. Phys.*, 2016, **93**, 115409.
258 B. Sipos, A. F. Kusmartseva, A. Akrap, H. Berger, L. Forró and E. Tutiš, *Nat. Mater.*, 2008, **7**, 960–965.
259 M. Ghorbani-Asl, A. Kuc, P. Miró and T. Heine, *Adv. Mater.*, 2016, **28**, 853–856.
260 K. Xu, Z. Wang, F. Wang, Y. Huang, F. Wang, L. Yin, C. Jiang and J. He, *Adv. Mater.*, 2015, **27**, 7881–7887.
261 Y. Zhou, Z. Wang, P. Yang, X. Zu, L. Yang, X. Sun and F. Gao, *ACS Nano*, 2012, **6**, 9727–9736.
262 M. M. Ugeda, A. J. Bradley, Y. Zhang, S. Onishi, Y. Chen, W. Ruan, C. Ojeda-Aristizabal, H. Ryu, M. T. Edmonds and H.-Z. Tsai, *et al.*, *Nat. Phys.*, 2016, **12**, 92–97.
263 H. Li, G. Lu, Y. Wang, Z. Yin, C. Cong, Q. He, L. Wang, F. Ding, T. Yu and H. Zhang, *Small*, 2013, **9**, 1974–1981.
264 C. Li, O. van t Erve, J. Robinson, Y. Liu, L. Li and B. Jonker, *Nat. Nanotechnol.*, 2014, **9**, 218–224.
265 Y. Min, J. W. Roh, H. Yang, M. Park, S. I. Kim, S. Hwang, S. M. Lee, K. H. Lee and U. Jeong, *Adv. Mater.*, 2013, **25**, 1425–1429.
266 A. C. Ferrari, F. Bonaccorso, V. Fal'Ko, K. S. Novoselov, S. Roche, P. Bøggild, S. Borini, F. H. Koppens, V. Palermo and N. Pugno, *et al.*, *Nanoscale*, 2015, **7**, 4598–4810.
267 Y. Zhang, T.-T. Tang, C. Girit, Z. Hao, M. C. Martin, A. Zettl, M. F. Crommie, Y. R. Shen and F. Wang, *Nature*, 2009, **459**, 820–823.
268 K. F. Mak, C. H. Lui, J. Shan and T. F. Heinz, *Phys. Rev. Lett.*, 2009, **102**, 256405.
269 Y. Zhang, Y.-W. Tan, H. L. Stormer and P. Kim, *Nature*, 2005, **438**, 201–204.
270 K. Novoselov, E. McCann, S. Morozov, V. I. Fal ko, M. Katsnelson, U. Zeitler, D. Jiang, F. Schedin and A. Geim, *Nat. Phys.*, 2006, **2**, 177–180.
271 D. Yoon, Y.-W. Son and H. Cheong, *Nano Lett.*, 2011, **11**, 3227–3231.
272 Y. Su, H. Wei, R. Gao, Z. Yang, J. Zhang, Z. Zhong and Y. Zhang, *Carbon*, 2012, **50**, 2804–2809.
273 C. Lee, X. Wei, J. W. Kysar and J. Hone, *Science*, 2008, **321**, 385–388.
274 J. W. Suk, R. D. Piner, J. An and R. S. Ruoff, *ACS Nano*, 2010, **4**, 6557–6564.
275 N. Bendiab, J. Renard, C. Schwarz, L. Djevahirdjian, V. Bouchiat, J. Coraux and L. Marty, *J. Raman Spectrosc.*, 2017, DOI: 10.1002/jrs.5267.
276 H. Malekpour and A. Balandin, *J. Raman Spectrosc.*, 2017, DOI: 10.1002/jrs.5230.
277 X. Wang, X. Li, L. Zhang, Y. Yoon, P. K. Weber, H. Wang, J. Guo and H. Dai, *Science*, 2009, **324**, 768–771.
278 B. Guo, L. Fang, B. Zhang and J. R. Gong, *Insci. J.*, 2011, **1**, 80–89.
279 H. Liu, Y. Liu and D. Zhu, *J. Mater. Chem.*, 2011, **21**, 3335–3345.
280 J. E. Lee, G. Ahn, J. Shim, Y. S. Lee and S. Ryu, *Nat. Commun.*, 2012, **3**, 1024.
281 N. Jung, B. Kim, A. C. Crowther, N. Kim, C. Nuckolls and L. Brus, *ACS Nano*, 2011, **5**, 5708–5716.
282 N. Jung, N. Kim, S. Jockusch, N. J. Turro, P. Kim and L. Brus, *Nano Lett.*, 2009, **9**, 4133–4137.
283 B. Das, R. Voggu, C. S. Rout and C. Rao, *Chem. Commun.*, 2008, 5155–5157.
284 R. Voggu, B. Das, C. S. Rout and C. N. R. Rao, *J. Phys.: Condens. Matter*, 2008, **20**, 472204.
285 A. C. Crowther, A. Ghassaei, N. Jung and L. E. Brus, *ACS Nano*, 2012, **6**, 1865–1875.
286 D. Zhan, L. Sun, Z. H. Ni, L. Liu, X. F. Fan, Y. Wang, T. Yu, Y. M. Lam, W. Huang and Z. X. Shen, *Adv. Funct. Mater.*, 2010, **20**, 3504–3509.
287 J. W. McClure, *Phys. Rev.*, 1956, **104**, 666–671.
288 A. A. Bykov, A. Kalagin and A. K. Bakarov, *JETP Lett.*, 2005, **81**, 523–526.
289 O. Kashuba and V. I. Fal'ko, *New J. Phys.*, 2012, **14**, 105016.
290 J. Yan, T. Villarson, E. A. Henriksen, P. Kim and A. Pinczuk, *Phys. Rev. B: Condens. Matter Mater. Phys.*, 2009, **80**, 241417.
291 M. Lazzeri, S. Piscanec, F. Mauri, A. Ferrari and J. Robertson, *Phys. Rev. B: Condens. Matter Mater. Phys.*, 2006, **73**, 155426.

292 C. Faugeras, P. Kossacki, D. M. Basko, M. Amado, M. Sprinkle, C. Berger, W. A. de Heer and M. Potemski, *Phys. Rev. B: Condens. Matter Mater. Phys.*, 2010, **81**, 155436.
293 F. Guinea, M. Katsnelson and A. Geim, *Nat. Phys.*, 2010, **6**, 30–33.
294 N. Ferralis, *J. Mater. Sci.*, 2010, **45**, 5135–5149.
295 J.-U. Lee, D. Yoon and H. Cheong, *Nano Lett.*, 2012, **12**, 4444–4448.
296 S. Berciaud, S. Ryu, L. E. Brus and T. F. Heinz, *Nano Lett.*, 2009, **9**, 346–352.
297 R. Loudon, *Adv. Phys.*, 1964, **13**, 423–482.
298 S.-M. Choi, S.-H. Jhi and Y.-W. Son, *Phys. Rev. B: Condens. Matter Mater. Phys.*, 2010, **81**, 081407.
299 M. S. Bronsgeest, N. Bendiab, S. Mathur, A. Kimouche, H. T. Johnson, J. Coraux and P. Pochet, *Nano Lett.*, 2015, **15**, 5098–5104.
300 S. R. Na, X. Wang, R. D. Piner, R. Huang, C. G. Willson and K. M. Liechti, *ACS Nano*, 2016, **10**, 9616–9625.
301 C. Bousige, F. Balima, D. Machon, G. S. Pinheiro, A. Torres-Dias, J. Nicolle, D. Kalita, N. Bendiab, L. Marty, V. Bouchiat, G. Montagnac, A. G. Souza Filho, P. Poncharal and A. San-Miguel, *Nano Lett.*, 2017, **17**, 21–27.
302 J. H. Lee, J. Y. Tan, C.-T. Toh, S. P. Koenig, V. Fedorov, A. H. Castro Neto and B. Özyilmaz, *Nano Lett.*, 2014, **14**, 2677–2680.
303 P.-H. Tan, Y. Deng, Q. Zhao and W. Cheng, *Appl. Phys. Lett.*, 1999, **74**, 1818.
304 I. Calizo, A. Balandin, W. Bao, F. Miao and C. Lau, *Nano Lett.*, 2007, **7**, 2645–2649.
305 I. Calizo, F. Miao, W. Bao, C. Lau and A. Balandin, *Appl. Phys. Lett.*, 2007, **91**, 071913.
306 C. Faugeras, B. Faugeras, M. Orlita, M. Potemski, R. R. Nair and A. Geim, *ACS Nano*, 2010, **4**, 1889–1892.
307 M. Freitag, M. Steiner, Y. Martin, V. Perebeinos, Z. Chen, J. C. Tsang and P. Avouris, *Nano Lett.*, 2009, **9**, 1883–1888.
308 Z. Ni, H. Wang, J. Kasim, H. Fan, T. Yu, Y. Wu, Y. Feng and Z. Shen, *Nano Lett.*, 2007, **7**, 2758–2763.
309 T. Yu, Z. Ni, C. Du, Y. You, Y. Wang and Z. Shen, *J. Phys. Chem. C*, 2008, **112**, 12602–12605.
310 X. Li, C. W. Magnuson, A. Venugopal, J. An, J. W. Suk, B. Han, M. D. Borysiak, W. Cai, A. Velamakanni and Y. Zhu, *et al.*, *Nano Lett.*, 2010, **10**, 4328–4334.
311 K.-D. Park, M. B. Raschke, J. M. Atkin, Y. H. Lee and M. S. Jeong, *Adv. Mater.*, 2017, **29**, 1603601.
312 D. Graf, F. Molitor, K. Ensslin, C. Stampfer, A. Jungen, C. Hierold and L. Wirtz, *Solid State Commun.*, 2007, **143**, 44–46.
313 S. Chen, Q. Li, Q. Zhang, Y. Qu, H. Ji, R. S. Ruoff and W. Cai, *Nanotechnology*, 2012, **23**, 365701.
314 C. Stampfer, F. Molitor, D. Graf, K. Ensslin, A. Jungen, C. Hierold and L. Wirtz, *Appl. Phys. Lett.*, 2007, **91**, 241907.
315 J. Campos, H. Miranda, C. Rabelo, E. Sandoz-Rosado, S. Pandley, J. Riikonen, A. Cano-Marquez and A. Jorio, *J. Raman Spectrosc.*, 2017, DOI: 10.1002/jrs.5225.
316 Q. Li, H. Chou, J. Zhong, J. Liu, A. Dolocan, J. Zhang, Y. Zhou, R. S. Ruoff, S. Chen and W. Cai, *et al.*, *Nano Lett.*, 2013, **13**, 486–490.
317 K. S. Kim, Y. Zhao, H. Jang, S. Y. Lee, J. M. Kim, K. S. Kim, J.-H. Ahn, P. Kim, J.-Y. Choi and B. H. Hong, *Nature*, 2009, **457**, 706–710.
318 X. Li, W. Cai, L. Colombo and R. S. Ruoff, *Nano Lett.*, 2009, **9**, 4268–4272.
319 H. Li, Z. Kang, Y. Liu and S. Lee, *J. Mater. Chem.*, 2012, **22**, 24230–24253.
320 Y. Sun, B. Zhou, Y. Lin, W. Wang, K. A. S. Fernando, P. Pathak, M. J. Meziani, B. A. Harruff, X. Wang and H. Wang, *et al.*, *J. Am. Chem. Soc.*, 2006, **128**, 7756–7757.
321 H. Ming, Z. Ma, Y. Liu, K. Pan, H. Yu, F. Wang and Z. Kang, *Dalton Trans.*, 2012, **41**, 9526–9531.
322 Y. Dong, N. Zhou, X. Lin, L. Jianpeng, Y. Chi and G. Chen, *Chem. Mater.*, 2010, **22**, 5895–5899.
323 L. Zheng, Y. Chi, Y. Dong, J. Lin and B. Wang, *J. Am. Chem. Soc.*, 2009, **131**, 4564–4565.
324 L. Cao, X. Wang, M. J. Meziani, F. Lu, H. Wang, P. G. Luo, Y. Lin, A. H. Barbara, L. M. Veca and D. Murray, *et al.*, *J. Am. Chem. Soc.*, 2007, **129**, 11318–11319.
325 Y. Li, Y. Hu, Y. Zhao, G. Shi, L. Deng, Y. Hou and L. Qu, *Adv. Mater.*, 2011, **23**, 776–780.
326 H. X. Zhao, L. Q. Liu, Z. De Liu, Y. Wang, X. J. Zhao and C. Z. Huang, *Chem. Commun.*, 2011, **47**, 2604–2606.
327 L. Cao, S. Sahu, P. Anilkumar, C. E. Bunker, J. Xu, K. A. S. Fernando, P. Wang, E. A. Guliants, K. N. Tackett and Y. Sun, *J. Am. Chem. Soc.*, 2011, **133**, 4754–4757.
328 V. Georgakilas, J. A. Perman, J. Tucek and R. Zboril, *Chem. Rev.*, 2015, **115**, 4744–4822.
329 L. A. Ponomarenko, F. Schedin, M. I. Katsnelson, R. Yang, E. Hill, K. S. Novoselov and A. K. Geim, *Science*, 2008, **320**, 356–358.
330 X. Yan, X. Cui, B. Li and L. Li, *Nano Lett.*, 2010, **10**, 1869–1873.
331 S. Neubeck, L. A. Ponomarenko, F. Freitag, A. J. M. Giesbers, U. Zeitler, S. V. Morozov, P. Blake, A. K. Geim and K. S. Novoselov, *Small*, 2010, **6**, 1469–1473.
332 L. Li and X. Yan, *J. Phys. Chem. Lett.*, 2010, **1**, 2572–2576.
333 K. Ritter and J. W. Lyding, *Nat. Mater.*, 2009, **8**, 235–242.
334 J. Peng, W. Gao, B. K. Gupta, Z. Liu, R. Romero-Aburto, L. Ge, L. Song, L. B. Alemany, X. Zhan, G. Gao, S. A. Vithayathil, B. A. Kaipparettu, A. A. Marti, T. Hayashi, J.-J. Zhu and P. M. Ajayan, *Nano Lett.*, 2012, **12**, 844–849.
335 H. Li, X. He, Z. Kang, H. Huang, Y. Liu, J. Liu, S. Lian, C. H. A. Tsang, X. Yang and S. Lee, *Angew. Chem., Int. Ed.*, 2010, **49**, 4430–4434.
336 S. Hu, K. Niu, J. Sun, J. Yang, N. Zhao and X. Du, *J. Mater. Chem.*, 2009, **19**, 484–488.
337 Z. Yang, M. Xu, Y. Liu, F. He, F. Gao, Y. Su, H. Wei and Y. Zhang, *Nanoscale*, 2014, **6**, 1890–1895.
338 Y. Fan, H. Cheng, C. Zhou, X. Xie, Y. Liu, L. Dai, J. Zhang and L. Qu, *Nanoscale*, 2012, **4**, 1776–1781.
339 Y. Wang and A. Hu, *J. Mater. Chem. C*, 2014, **2**, 6921–6939.
340 F. Cervantes-Sodi, G. Csanyi, S. Piscanec and A. Ferrari, *Phys. Rev. B: Condens. Matter Mater. Phys.*, 2008, **77**, 165427.
341 J. Campos-Delgado, J. M. Romo-Herrera, X. Jia, D. A. Cullen, H. Muramatsu, Y. A. Kim, T. Hayashi, Z. Ren, D. J. Smith and Y. Okuno, *et al.*, *Nano Lett.*, 2008, **8**, 2773–2778.

342 A. Narita, I. A. Verzhbitskiy, W. Frederickx, K. S. Mali, S. A. Jensen, M. R. Hansen, M. Bonn, S. De Feyter, C. Casiraghi and X. Feng, *et al.*, *ACS Nano*, 2014, **8**, 11622–11630.
343 S. Osella, A. Narita, M. G. Schwab, Y. Hernandez, X. Feng, K. Müllen and D. Beljonne, *ACS Nano*, 2012, **6**, 5539–5548.
344 R. Saito, M. Furukawa, G. Dresselhaus and M. Dresselhaus, *J. Phys.: Condens. Matter*, 2010, **22**, 334203.
345 C. Castiglioni, M. Tommasini and G. Zerbi, *Philos. Trans. R. Soc., A*, 2004, **362**, 2425–2459.
346 F. Varchon, R. Feng, J. Hass, X. Li, B. N. Nguyen, C. Naud, P. Mallet, J.-Y. Veuillen, C. Berger and E. H. Conrad, *et al.*, *Phys. Rev. Lett.*, 2007, **99**, 126805.
347 S. Zhou, G.-H. Gweon, A. Fedorov, P. First, W. De Heer, D.-H. Lee, F. Guinea, A. C. Neto and A. Lanzara, *Nat. Mater.*, 2007, **6**, 770–775.
348 J. Robinson, X. Weng, K. Trumbull, R. Cavalero, M. Wetherington, E. Frantz, M. LaBella, Z. Hughes, M. Fanton and D. Snyder, *ACS Nano*, 2009, **4**, 153–158.
349 J. Röhrl, M. Hundhausen, K. Emtsev, T. Seyller, R. Graupner and L. Ley, *Appl. Phys. Lett.*, 2008, **92**, 201918.
350 N. Ferralis, R. Maboudian and C. Carraro, *Phys. Rev. Lett.*, 2008, **101**, 156801.
351 N. Mounet and N. Marzari, *Phys. Rev. B: Condens. Matter Mater. Phys.*, 2005, **71**, 205214.
352 G. A. Slack and S. Bartram, *J. Appl. Phys.*, 1975, **46**, 89–98.
353 J. Hass, F. Varchon, J. E. Millán-Otoya, M. Sprinkle, N. Sharma, W. A. de Heer, C. Berger, P. N. First, L. Magaud and E. H. Conrad, *Phys. Rev. Lett.*, 2008, **100**, 125504.
354 J. Campos-Delgado, L. G. Cançado, C. A. Achete, A. Jorio and J.-P. Raskin, *Nano Res.*, 2013, **6**, 269–274.
355 H. Zhao, Y.-C. Lin, C.-H. Yeh, H. Tian, Y.-C. Chen, D. Xie, Y. Yang, K. Suenaga, T.-L. Ren and P.-W. Chiu, *ACS Nano*, 2014, **8**, 10766–10773.
356 L. Gomez De Arco, Y. Zhang, C. W. Schlenker, K. Ryu, M. E. Thompson and C. Zhou, *ACS Nano*, 2010, **4**, 2865–2873.
357 S. Bae, H. Kim, Y. Lee, X. Xu, J.-S. Park, Y. Zheng, J. Balakrishnan, T. Lei, H. R. Kim and Y. I. Song, *et al.*, *Nat. Nanotechnol.*, 2010, **5**, 574–578.
358 J. Xue, J. Sanchez-Yamagishi, D. Bulmash, P. Jacquod, A. Deshpande, K. Watanabe, T. Taniguchi, P. Jarillo-Herrero and B. J. LeRoy, *Nat. Mater.*, 2011, **10**, 282–285.
359 G. Wang, Y. Kim, M. Choe, T.-W. Kim and T. Lee, *Adv. Mater.*, 2011, **23**, 755–760.
360 A. Jorio and L. G. Cançado, *Solid State Commun.*, 2013, **175**, 3–12.
361 V. Popov, *J. Raman Spectrosc.*, 2017, DOI: 10.1002/jrs.5189.
362 M. P. Levendorf, C.-J. Kim, L. Brown, P. Y. Huang, R. W. Havener, D. A. Muller and J. Park, *Nature*, 2012, **488**, 627–632.
363 Z. Liu, L. Ma, G. Shi, W. Zhou, Y. Gong, S. Lei, X. Yang, J. Zhang, J. Yu, K. P. Hackenberg, A. Babakhani, J.-C. Idrobo, R. Vajtai, R. Vajtai and P. M. Ajayan, *Nat. Nanotechnol.*, 2013, **8**, 119–124.
364 H. Fang, C. Battaglia, C. Carraro, S. Nemsak, B. Ozdol, J. S. Kang, H. A. Bechtel, S. B. Desai, F. Kronast, A. A. Unal, G. Conti, C. Conlon, G. K. Palsson, M. C. Martin, A. M. Minor, C. S. Fadley, E. Yablonovitch, R. Maboudian and A. Javey, *Proc. Natl. Acad. Sci. U. S. A.*, 2014, **111**, 6198–6202.
365 Y. Gong, S. Lei, G. Ye, B. Li, Y. He, K. Keyshar, X. Zhang, Q. Wang, J. Lou, Z. Liu, R. Vajtai, W. Zhou and P. M. Ajayan, *Nano Lett.*, 2015, **15**, 6135–6141.
366 S. Latini, K. T. Winther, T. Olsen and K. S. Thygesen, *Nano Lett.*, 2017, **17**, 938–945.
367 S. Bertolazzi, D. Krasnozhon and A. Kis, *ACS Nano*, 2013, **7**, 3246–3252.
368 C. H. Lui, Z. Ye, C. Ji, K.-C. Chiu, C.-T. Chou, T. I. Andersen, C. Means-Shively, H. Anderson, J.-M. Wu, T. Kidd, Y.-H. Lee and R. He, *Phys. Rev. B: Condens. Matter Mater. Phys.*, 2015, **91**, 165403.
369 D. A. Dikin, S. Stankovich, E. J. Zimney, R. D. Piner, G. H. B. Dommett, G. Evmenenko, S. T. Nguyen and R. S. Ruoff, *Nature*, 2007, **448**, 457–460.
370 I. K. Moon, J. Lee, R. S. Ruoff and H. Lee, *Nat. Commun.*, 2010, **1**, 73.
371 X. Huang, S. Li, Y. Huang, S. Wu, X. Zhou, S. Li, C. L. Gan, F. Boey, C. A. Mirkin and H. Zhang, *Nat. Commun.*, 2011, **2**, 292.
372 X. Huang, S. Li, S. Wu, Y. Huang, F. Boey, C. L. Gan and H. Zhang, *Adv. Mater.*, 2012, **24**, 979–983.
373 D. R. Dreyer, S. Park, C. W. Bielawski and R. S. Ruoff, *Chem. Soc. Rev.*, 2010, **39**, 228–240.
374 Y. Zhang, L. Guo, H. Xia, Q. Chen, J. Feng and H. Sun, *Adv. Opt. Mater.*, 2014, **2**, 10–28.
375 S. Stankovich, D. A. Dikin, R. D. Piner, K. A. Kohlhaas, A. Kleinhammes, Y. Jia, Y. Wu, S. T. Nguyen and R. S. Ruoff, *Carbon*, 2007, **45**, 1558–1565.
376 Y. Zhu, S. Murali, M. D. Stoller, A. Velamakanni, R. D. Piner and R. S. Ruoff, *Carbon*, 2010, **48**, 2118–2122.
377 S. Pei and H. Cheng, *Carbon*, 2012, **50**, 3210–3228.
378 S. Eigler, S. Grimm, M. Enzelbergerheim, P. Muller and A. Hirsch, *Chem. Commun.*, 2013, **49**, 7391–7393.
379 R. Larciprete, S. Fabris, T. Sun, P. Lacovig, A. Baraldi and S. Lizzit, *J. Am. Chem. Soc.*, 2011, **133**, 17315–17321.
380 I. K. Moon, J. Lee and H. Lee, *Chem. Commun.*, 2011, **47**, 9681–9683.
381 R. Trusovas, K. Ratautas, G. Račiukaitis, J. Barkauskas, I. Stankevičienė, G. Niaura and R. Mažeikienė, *Carbon*, 2013, **52**, 574–582.
382 G. K. Ramesha and S. Sampath, *J. Phys. Chem. C*, 2009, **113**, 7985–7989.
383 S. J. An, Y. Zhu, S. H. Lee, M. D. Stoller, T. Emilsson, S. Park, A. Velamakanni, J. An and R. S. Ruoff, *J. Phys. Chem. Lett.*, 2010, **1**, 1259–1263.
384 T. V. Cuong, V. H. Pham, Q. T. Tran, S. H. Hahn, J. S. Chung, E. W. Shin and E. J. Kim, *Mater. Lett.*, 2010, **64**, 399–401.
385 S. Stankovich, R. D. Piner, X. Chen, N. Wu, S. T. Nguyen and R. S. Ruoff, *J. Mater. Chem.*, 2006, **16**, 155–158.
386 P. Cui, J. Lee, E. Hwang and H. Lee, *Chem. Commun.*, 2011, **47**, 12370–12372.
387 J. Shen, Y. Hu, M. Shi, X. Lu, C. Qin, C. Li and M. Ye, *Chem. Mater.*, 2009, **21**, 3514–3520.

388 T. Kuilla, S. Bhadra, D. Yao, N. H. Kim, S. Bose and J. H. Lee, *Prog. Polym. Sci.*, 2010, **35**, 1350–1375.
389 W.-L. Song, M.-S. Cao, M.-M. Lu, S. Bi, C.-Y. Wang, J. Liu, J. Yuan and L.-Z. Fan, *Carbon*, 2014, **66**, 67–76.
390 Y.-B. Luo, J.-S. Cheng, Q. Ma, Y.-Q. Feng and J.-H. Li, *Anal. Methods*, 2011, **3**, 92–98.
391 Y.-M. Lin, A. Valdes-Garcia, S.-J. Han, D. B. Farmer, I. Meric, Y. Sun, Y. Wu, C. Dimitrakopoulos, A. Grill and P. Avouris, *et al.*, *Science*, 2011, **332**, 1294–1297.
392 F. Xia, T. Mueller, Y.-M. Lin, A. Valdes-Garcia and P. Avouris, *Nat. Nanotechnol.*, 2009, **4**, 839–843.
393 T. Mueller, F. Xia and P. Avouris, *Nat. Photonics*, 2010, **4**, 297–301.
394 H. Choi, J. S. Choi, J.-S. Kim, J.-H. Choe, K. H. Chung, J.-W. Shin, J. T. Kim, D.-H. Youn, K.-C. Kim and J.-I. Lee, *et al.*, *Small*, 2014, **10**, 3685–3691.
395 W. Li, X. Geng, Y. Guo, J. Rong, Y. Gong, L. Wu, X. Zhang, P. Li, J. Xu and G. Cheng, *et al.*, *ACS Nano*, 2011, **5**, 6955–6961.
396 Y.-M. Lin, K. A. Jenkins, A. Valdes-Garcia, J. P. Small, D. B. Farmer and P. Avouris, *Nano Lett.*, 2009, **9**, 422–426.
397 H. Wang, T. Taychatanapat, A. Hsu, K. Watanabe, T. Taniguchi, P. Jarillo-Herrero and T. Palacios, *IEEE Electron Device Lett.*, 2011, **32**, 1209–1211.
398 K. Share, A. P. Cohn, R. E. Carter and C. L. Pint, *Nanoscale*, 2016, **8**, 16435–16439.
399 D. P. Dubal, O. Ayyad, V. Ruiz and P. Gomez-Romero, *Chem. Soc. Rev.*, 2015, **44**, 1777–1790.
400 Y. Wang, Y. Song and Y. Xia, *Chem. Soc. Rev.*, 2016, **45**, 5925–5950.
401 M.-S. Balogun, Y. Luo, W. Qiu, P. Liu and Y. Tong, *Carbon*, 2016, **98**, 162–178.
402 X. Cong, C. Cheng, Y. Liao, Y. Ye, C. Dong, H. Sun, X. Ji, W. Zhang, P. Fang and L. Miao, *et al.*, *J. Phys. Chem. C*, 2015, **119**, 20864–20870.
403 W. Zhang, C. Cheng, P. Fang, B. Tang, J. Zhang, G. Huang, X. Cong, B. Zhang, X. Ji and L. Miao, *Phys. Chem. Chem. Phys.*, 2016, **18**, 4376–4384.
404 H. Wan, J. Liu, Y. Ruan, L. Lv, L. Peng, X. Ji, L. Miao and J. Jiang, *ACS Appl. Mater. Interfaces*, 2015, **7**, 15840–15847.
405 L. J. Hardwick, P. W. Ruch, M. Hahn, W. Scheifele, R. Kötz and P. Novák, *J. Phys. Chem. Solids*, 2008, **69**, 1232–1237.
406 A. P. Cohn, K. Share, R. Carter, L. Oakes and C. L. Pint, *Nano Lett.*, 2015, **16**, 543–548.
407 R. Baddour-Hadjean and J.-P. Pereira-Ramos, *Chem. Rev.*, 2009, **110**, 1278–1319.
408 M. Inaba, H. Yoshida, Z. Ogumi, T. Abe, Y. Mizutani and M. Asano, *J. Electrochem. Soc.*, 1995, **142**, 20–26.
409 Q. Shi, K. Dokko and D. A. Scherson, *J. Phys. Chem. B*, 2004, **108**, 4789–4793.
410 J. C. Chacon-Torres, L. Wirtz and T. Pichler, *ACS Nano*, 2013, **7**, 9249–9259.
411 F. Xiong, H. Wang, X. Liu, J. Sun, M. Brongersma, E. Pop and Y. Cui, *Nano Lett.*, 2015, **15**, 6777–6784.
412 Y. Wang, S. W. Tong, X. F. Xu, B. Özyilmaz and K. P. Loh, *Adv. Mater.*, 2011, **23**, 1514–1518.
413 Z. Yin, S. Sun, T. Salim, S. Wu, X. Huang, Q. He, Y. M. Lam and H. Zhang, *ACS Nano*, 2010, **4**, 5263–5268.
414 S. Li, Y. Luo, W. Lv, W. Yu, S. Wu, P. Hou, Q. Yang, Q. Meng, C. Liu and H.-M. Cheng, *Adv. Energy Mater.*, 2011, **1**, 486–490.
415 J. Liang, H. Bi, D. Wan and F. Huang, *Adv. Funct. Mater.*, 2012, **22**, 1267–1271.
416 D. Zhang, F. Xie, P. Lin and W. C. Choy, *ACS Nano*, 2013, **7**, 1740–1747.
417 Z. Wen, S. Cui, H. Pu, S. Mao, K. Yu, X. Feng and J. Chen, *Adv. Mater.*, 2011, **23**, 5445–5450.
418 V. Gupta, N. Chaudhary, R. Srivastava, G. D. Sharma, R. Bhardwaj and S. Chand, *J. Am. Chem. Soc.*, 2011, **133**, 9960–9963.
419 Y. Lin, X. Li, D. Xie, T. Feng, Y. Chen, R. Song, H. Tian, T. Ren, M. Zhong and K. Wang, *et al.*, *Energy Environ. Sci.*, 2013, **6**, 108–115.
420 W. Zhou, J. Zhu, C. Cheng, J. Liu, H. Yang, C. Cong, C. Guan, X. Jia, H. J. Fan and Q. Yan, *et al.*, *Energy Environ. Sci.*, 2011, **4**, 4954–4961.
421 J. Liu, Y. Xue, Y. Gao, D. Yu, M. Durstock and L. Dai, *Adv. Mater.*, 2012, **24**, 2228–2233.
422 Z. Yin, J. Zhu, Q. He, X. Cao, C. Tan, H. Chen, Q. Yan and H. Zhang, *Adv. Energy Mater.*, 2014, **4**, 1–19.
423 J. T. Lim, H. Lee, H. Cho, B.-H. Kwon, N. S. Cho, B. K. Lee, J. Park, J. Kim, J.-H. Han and J.-H. Yang, *et al.*, *Sci. Rep.*, 2015, **5**, 17748.
424 S. S.-Y. Juang, C.-Y. Liu, C.-W. Huang, J. H.-H. Liao, T. Wang, Y. Yu and H.-C. Chui, *Appl. Surf. Sci.*, 2015, **331**, 472–476.
425 A. Reserbat-Plantey, L. Marty, O. Arcizet, N. Bendiab and V. Bouchiat, *Nat. Nanotechnol.*, 2012, **7**, 151–155.
426 A. C. Neto, F. Guinea, N. M. Peres, K. S. Novoselov and A. K. Geim, *Rev. Mod. Phys.*, 2009, **81**, 109.
427 R. R. Nair, P. Blake, A. N. Grigorenko, K. S. Novoselov, T. J. Booth, T. Stauber, N. M. Peres and A. K. Geim, *Science*, 2008, **320**, 1308.
428 T. J. Booth, P. Blake, R. R. Nair, D. Jiang, E. W. Hill, U. Bangert, A. Bleloch, M. Gass, K. S. Novoselov and M. I. Katsnelson, *et al.*, *Nano Lett.*, 2008, **8**, 2442–2446.
429 J. S. Bunch, A. M. Van Der Zande, S. S. Verbridge, I. W. Frank, D. M. Tanenbaum, J. M. Parpia, H. G. Craighead and P. L. McEuen, *Science*, 2007, **315**, 490–493.
430 B. Lassagne, D. Garcia-Sanchez, A. Aguasca and A. Bachtold, *Nano Lett.*, 2008, **8**, 3735–3738.
431 K. Jensen, K. Kim and A. Zettl, *Nat. Nanotechnol.*, 2008, **3**, 533–537.
432 H. Peng, C. Chang, S. Aloni, T. Yuzvinsky and A. Zettl, *Phys. Rev. Lett.*, 2006, **97**, 087203.
433 A. D. O. Connell, M. Hofheinz, M. Ansmann, R. C. Bialczak, M. Lenander, E. Lucero, M. Neeley, D. Sank, H. Wang and M. Weides, *et al.*, *Nature*, 2010, **464**, 697–703.
434 O. Frank, G. Tsoukleri, J. Parthenios, K. Papagelis, I. Riaz, R. Jalil, K. S. Novoselov and C. Galiotis, *ACS Nano*, 2010, **4**, 3131–3138.
435 O. Frank, G. Tsoukleri, I. Riaz, K. Papagelis, J. Parthenios, A. C. Ferrari, A. K. Geim, K. S. Novoselov and C. Galiotis, *Nat. Commun.*, 2011, **2**, 255.

436 H. Hosaka, K. Itao and S. Kuroda, *Sens. Actuators, A*, 1995, **49**, 87–95.
437 C.-J. Shih, Q. H. Wang, Y. Son, Z. Jin, D. Blankschtein and M. S. Strano, *ACS Nano*, 2014, **8**, 5790–5798.
438 K. Roy, M. Padmanabhan, S. Goswami, T. P. Sai, G. Ramalingam, S. Raghavan and A. Ghosh, *Nat. Nanotechnol.*, 2013, **8**, 826–830.
439 G. W. Shim, K. Yoo, S.-B. Seo, J. Shin, D. Y. Jung, I.-S. Kang, C. W. Ahn, B. J. Cho and S.-Y. Choi, *ACS Nano*, 2014, **8**, 6655–6662.
440 P. T. K. Loan, W. Zhang, C.-T. Lin, K.-H. Wei, L.-J. Li and C.-H. Chen, *Adv. Mater.*, 2014, **26**, 4838–4844.
441 L. Ju, J. Velasco Jr, E. Huang, S. Kahn, C. Nosiglia, H.-Z. Tsai, W. Yang, T. Taniguchi, K. Watanabe and Y. Zhang, *et al.*, *Nat. Nanotechnol.*, 2014, **9**, 348–352.
442 Y. Liu, N. O. Weiss, X. Duan, H. C. Cheng, Y. Huang and X. Duan, *Nat. Rev. Mater.*, 2016, **1**, 16042.
443 H. Cheng, G. Wang, D. Li, Q. He, A. Yin, Y. Liu, H. Wu, M. Ding, Y. Huang and X. Duan, *Nano Lett.*, 2015, **16**, 367–373.